Developement of microscopy system for time-resolved fluorescence detection of gadolinium/terbium hybrid macromolecular complexes for bimodal imaging of atherothrombosis

Trong Nghia Nguyen

▶ To cite this version:

Trong Nghia Nguyen. Developement of microscopy system for time-resolved fluorescence detection of gadolinium/terbium hybrid macromolecular complexes for bimodal imaging of atherothrombosis. Physics [physics]. Université Paris-Nord - Paris XIII, 2014. English. NNT : 2014PA132005 . tel-01263903

HAL Id: tel-01263903
https://theses.hal.science/tel-01263903

Submitted on 29 Jan 2016

HAL is a multi-disciplinary open access archive for the deposit and dissemination of scientific research documents, whether they are published or not. The documents may come from teaching and research institutions in France or abroad, or from public or private research centers.

L'archive ouverte pluridisciplinaire **HAL**, est destinée au dépôt et à la diffusion de documents scientifiques de niveau recherche, publiés ou non, émanant des établissements d'enseignement et de recherche français ou étrangers, des laboratoires publics ou privés.

UNIVERSITÉ PARIS 13 - INSTITUT GALILÉE

LABORATOIRE DE PHYSIQUE DES LASERS-CNRS UMR7538

LABORATOIRE DE RECHERCHES VASCULAIRES TRANSLATIONNELLES–INSERM U1148

N° attribué par la bibliothèque

|_|_|_|_|_|_|_|_|_|_|

THÈSE

pour obtenir le grade de

DOCTEUR DE L'UNIVERSITÉ PARIS 13

Discipline : Physique

présentée et soutenue publiquement

par

NGUYỄN TRỌNG NGHĨA

Soutenue le 23 juin 2014

Développement d'un système de microscopie pour la détection en temps résolu de la fluorescence de complexes macromoléculaires mixtes Gadolinium/Terbium destinés à l'imagerie bimodale de l'athérothrombose

Directeur de thèse : Jean-Michel Tualle

JURY

Mme	Nathalie	WESTBROOK	Présidente
Mme	Florence	GAZEAU	Rapporteur
Mme	Hong Nhung	TRAN	Rapporteur
M.	Phalla	OU	Examinateur
M.	Frédéric	CHAUBET	Co directeur de thèse
M.	Eric	TINET	Co directeur de thèse
M.	Jean-Michel	TUALLE	Directeur de thèse

This work was supported by the CNRS
(Centre National de la Recherche Scientifique)
through the contract number 254445
from march 2011 to february 2014

ACKNOWLEDGEMENTS

I would like to thank my supervisors Dr. Jean Michel Tualle, Prof. Frédéric Chaubet, Dr. Éric Tinet who have encouraged me throughout the course of this thesis and gave me valuable advices. I have gained important experience while working with them.

I would like to thank Dr. Anne Beilvert, Dr. Murielle Maire in the group Cardiovascular Bioengineering of Laboratory for Vascular Translational Science (LVTS) who have synthesized the agents needed for my experiments. In the same laboratory Graciela Pavon-Djavid and Liliane Louedec were very kind with me too when they helped me preparing the samples from the rats arteries.

I would like to thank my colleagues who are researchers in the departments of the Bichat Claude Bernard hospital: “Service Anatomie et Cytologie Pathologiques” and “Service de Radiologie et Imagerie Médicale”. They helped me a lot when I tried the *in vitro* and *in vivo* experiments

I would like to thank my colleagues in the Laboratoire de Physique des Lasers (LPL) where I worked most of the time, in particular the secretaries, mechanics and optics technicians for their assistance.

Finally, I would like to thank the support and encouragement of my friends and my family, in particular my father, my mother and my wife.

Outline

INTRODUCTION-- 1

1-ATHEROSCLEROSIS, IMAGING AND CONTRAST AGENTS----------------- 3

1.1 Evolution of atherosclerosis--- 3

1.2 Platelets and atherothrombosis -- 4

1.3 Magnetic resonance imaging--- 5
1.3.1 Larmor frequency - Excitation--- 6
1.3.2 Relaxation--- 7
1.3.3 Imaging-- 7

1.4 MRI contrast agent --- 9
1.4.1 T_2 contrast agent-- 9
1.4.2 T_1 contrast agent --10
1.4.3 Bimodal MRI/optical contrast agents---10

1.5 Optical properties of terbium (Tb3+) and europium (Eu3+) ions ----------------11
1.5.1 Absorption spectra---11
1.5.2 Emission spectra --13
1.5.3 Fluorescent lifetime--15

2-MICROSCOPE SYSTEM SETUP FOR TIME-GATED FLUORESCENCE---19

2.1 The microscope ---19

2.2 The laser--20

2.3 The filters --22

2.4 The chopper ---24

2.5 The EMCCD camera ---24
Frame Transfer Mode ---25
Non-Frame Transfer Mode---25

2.6 The shutter--26

2.7 The spectrometer---26

2.8 Electrical synchronization---26

2.9 How to get a fluorescent image? --27

2.10 "Mosaic" imaging--- 29

2.11 System background noise -- 30

2.12 Conclusion--- 31

3-THE EMCCD CAMERA ---33

3.1 CCD camera-- 33
3.1.1 The transfer of charges-- 33
3.1.2 The CCD cameras architectures -- 34

3.2 Quantification of the signal provided by our camera ------------------------------ 36
3.2.1 Theory --- 36
3.2.2 The function $F_0(k)$ and exponential constant g---------------------------------- 39
3.2.3 Numerical method to estimate average number of photoelectrons λ at input -- 40
3.2.4 An example -- 42

3.3 Use of the Camera for Long Decay Fluorescent Measurement ------------------ 49
3.3.1 Effect of vertical shift speed on the streaking of image --------------------------- 51
3.3.2 Application of vertical shift for lifetime measurement---------------------------- 57

3.4. Conclusion -- 61

4-P717-TB EXPERIMENTAL RESULTS---63

4.1 Synthesis of the fluorescent molecule -- 63
4.1.1 Synthesis of P717-Tb--- 63
4.1.2 Synthesis of P717-Tb-F -- 64

4.2 Optical properties of P717-Tb in solution--- 66
4.2.1 Spectrum --- 66
4.2.2 Fluorescent lifetime--- 67
4.2.3 Absorption cross-section--- 68

4.3 Fluorescent images of P717-Tb/PBS in healthy artery ---------------------------- 71
4.3.1 Preparation of the samples--- 71
4.3.2 Fluorescent images --- 72

4.4 Conclusion --- 76

5-EXPERIMENTAL RESULTS ON ATHEROSCLEROTIC RAT ARTERIES --77

5.1 Animal model -- 77

5.2 Preparation of contrast agent mixtures -- 77

5.3 Rat abdominal aorta MR imaging--- 78

5.4 Preparation of the rat’s arteries --- 78

5.5 Results --- 79

CONCLUSION---83

APPENDIX A ---85

APPENDIX B ---89

REFERENCES --95

Introduction

According to the American Heart Association, **atherosclerosis** “is a type of arteriosclerosis. The name comes from the Greek words *athero* (meaning gruel or paste) and *sclerosis* (hardness). It is the term for the process of fatty substances, cholesterol, cellular waste products, calcium and fibrin (a clotting material in the blood) building up in the inner lining of an artery. The buildup that results is called plaque” [1].

The development of atherosclerosis is usually a long process and its causes are not clear. Many scientists think atherosclerosis starts from the damages of the innermost layer of the artery. The reasons of those damages could be

+ High amounts of certain fats and cholesterol in the blood

+ High blood pressure

The biggest risk of atherosclerosis is a heart attack or a stroke that cause irreversible damages to the brain or the heart, possibly a sudden death. Because the development of atherosclerosis is over decades, an early detection of disease is very important for the treatment.

Since the pathology is deeply located in utmost important organs, a direct invasive observation would be extremely difficult and would be extremely dangerous. Moreover, the affected regions may be diverse and of varying sizes. Therefore, a good diagnostic method should both be non-invasive and independent on the pathology’s locations.

Blood cells are implied from the very beginning of the pathological process. In particular platelets play a pivotal role in cardiovascular diseases and there is a great interest in diagnostic approaches enabling activated platelet molecular imaging i.e. thrombotic pathological situation because platelets constitutes the main cell part of the thrombus.

Magnetic resonance imaging (MRI) is a method which can image the whole body. It could be a good technique to diagnose atherosclerosis, but its spatial resolution isn’t yet very good and the natural contrast between atheroma and its surrounding tissues may be poor. One can notice that if someday MRI achieves a one-cell or a sub-cellular resolution, the volume of data to acquire and to process would be really big! Moreover, ultimate MRI resolution will probably be limited for routine diagnosis by biological safety norms (maximum fields intensity, time derivative of fields, duration of exposure). For all these reasons, in MRI technique, a contrast agent is often used – and will be in the future - to enhance the contrast of the images or to label specific tissues or lesions we may want to localize in the body. It is therefore evident that an agent providing a high contrast while being very specific to the arteries lesions, at early stages if possible, with a low toxicity and side effects (intrinsically innocuous and/or efficient at low concentrations) is extremely desirable.

Since 2003, the Laboratory for Vascular Translational Science (formerly Laboratory for Polymer Bioenginneering) has developed with the company Guerbet Laboratories the use of a macromolecular MRI contrast agents (P717) including a gadolinium-based complex with a ligand (DOTA). The magnetic contrast can be appropriate, but the limitation due to the low spatial resolution of the MRI technique [2], [3], [4], [5] still persists and does not allow research on the cellular level, even on extracted samples.

The idea is to slightly modify the contrast agent to allow the study of its interactions with the tissues using another imaging modality which sensitivity and resolution would be complementary to that of MRI. If we substitute terbium ions to the gadolinium ones, the chemical properties of the agent isn't noticeably modified. However, the terbium ions are fluorescent, and the spatial resolution of an optical system can be well below one micrometer. Excitation wavelength is in the ultra-violet range. Fluorescence efficiency is very low, well below tissue autofluorescence, but since it has a very long emission time, a time-gated detection is feasible. UV excitation and low efficiency fluorescence is not possible *in vivo* as a routine diagnostic method. However, we can obtain on histological slices valuable information about the contrast agent's interaction with the arteries wall and the atherosclerotic pathologies.

We will start from the macromolecular precursor of P717, Gd and Tb complexes to obtain Tb and Gd complexes. Then these complexes would be endowed with biospecificity by coupling them with a ligand exhibiting a strong affinity for activated platelets. By mixing both biospecific contrast agents it should be possible to localize by MRI the pathological areas in vivo (rat model) and after sacrifice of the animals to visualize the thrombus at cellular scale with delayed fluorescence imaging of histological slices.

Fluorescence microscopy is widely developped for the examination of slices of tissues with the use of organic fluorophores for example linked to antibodies for the identification of tissues areas, cells or macromolecular biological structures. Beyond this use, organic fluorophores have numerous drawbacks when considering quantification and specificity of the signal. Thus there is a strong need of a system allowing to localize and efficiently quantify even very low amounts of contrast agent in situations where they are able to specifically bind to pertinent ligands of atherothrombosis, in our case: activated platelets. Fluorescence molecular imaging is the first challenge of this project. The second one is to get both MR and optical images from the same contrast agent, knowing that water molecules needed for the MR contrast are powerful quenchers of lanthanide fluorescence.

Chapter 1

Atherosclerosis, imaging and contrast agents

1.1 Evolution of atherosclerosis

It has long been thought that atherosclerosis was similar to a clogged pipe, where the pipe is a passive victim of a buildup of fatty materials and limescale, except that maybe it can show a little surface corrosion which acts as an anchor point. The development of atherosclerosis is presented in the figure 1.1 [6], [7], [8].

However, in fact, it is an extremely complex and still not fully understood pathology where the artery walls play an active role. All children older than age 10 have primary anatomic lesions. Sometimes, it even starts as young as one year old. No one is immune; the early stage seems to be independent on the geographic origin, the sex, the environment. The pathology initially evolves very slowly and during the first two or three decades, it is completely silent. Nevertheless, we know for sure that after this slow asymptomatic evolution, the atheroma evolves faster later and this speed depends heavily on some environmental factors like stress, food, exercise.

The pathology starts with repeated injury to the wall of arteries. A higher than normal blood pressure and shear stress in the blood flow are probably important factors here. In fact, for the animal models, like rabbits, used to study atherosclerosis, the pathology is initiated by scratching the inner wall of a coronary artery, and then by feeding the animals with a very fatty diet. The injury leads to an answer by the immune system and macrophages penetrate the artery wall. For some reason, they stay blocked here. When the macrophages die, their materials, for example their cholesterol-rich membranes stay in place in the middle of artery wall. This enhances the inflammation and more macrophages are attracted here. This process is the core of the first silent phase. When enough lipids are accumulated in the artery’s wall, fibrosis and calcification appear. The artery is partially blocked. Its wall becomes rigid and can rupture.

Of course, the sooner we can detect the pathology, the easier and least difficult is its mitigation. Imaging plays a key role here, and the two main methods of clinical imaging are X-ray tomography and Magnetic Resonance Imaging.

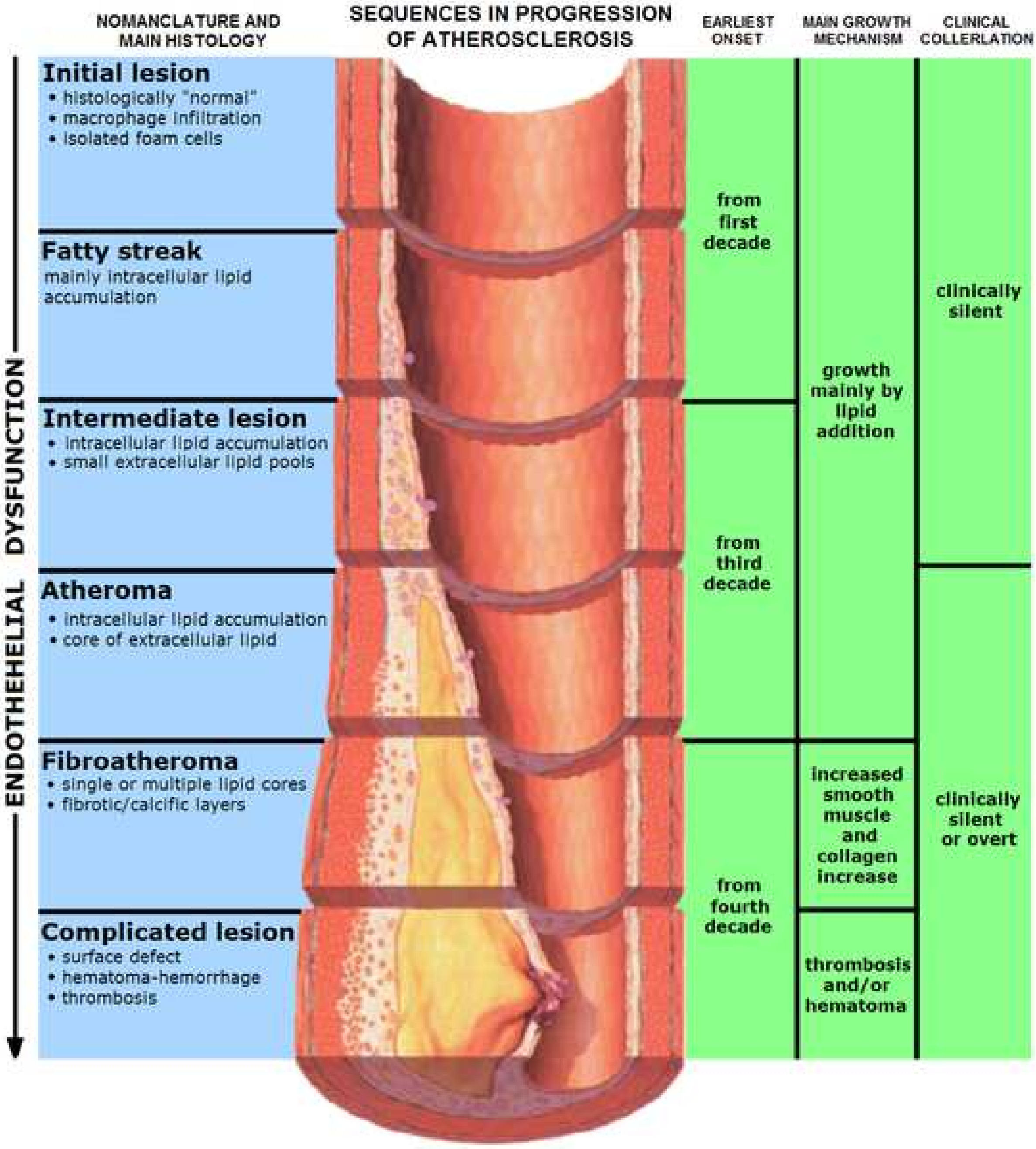
NOMANCLATURE AND MAIN HISTOLOGY
SEQUENCES IN PROGRESSION OF ATHEROSCLEROSIS
EARLIEST ONSET
MAIN GROWTH MECHANISM
CLINICAL COLLERLATION
Initial lesion
• histologically "normal"
• macrophage infiltration
• isolated foam cells
Fatty streak
mainly intracellular lipid accumulation
Intermediate lesion
• intracellular lipid accumulation
• small extracellular lipid pools
Atheroma
• intracellular lipid accumulation
• core of extracellular lipid
Fibroatheroma
• single or multiple lipid cores
• fibrotic/calcific layers
Complicated lesion
• surface defect
• hematoma-hemorrhage
• thrombosis
ENDOTHEHELIAL DYSFUNCTION
from first decade
from third decade
from fourth decade
growth mainly by lipid addition
increased smooth muscle and collagen increase
thrombosis and/or hematoma
clinically silent
clinically silent or overt

Figure 1.1: The development of atherosclerosis [6].

1.2 Platelets and atherothrombosis

When the atherosclerotic vessel is ruptured, thrombogenic substances are exposed and platelets contribute to the pathophysiologic process via adhesion, activation and aggregation stages [9]. At a cellular level, phenotypical and morphological modifications of vascular cells are observed early in atherosclerosis [10] and platelets represent a major link between inflammation, thrombosis and atherogenesis [11], [12]. Beside, activated vascular cells overexpress lectins, such as E-selectin, L-selectin and P-selectin, and proteoglycans on their surface. These are glycoconjugates which carbohydrate moieties play a critical role such as cell-cell interactions, cell growth, lymphocytes trafficking, thrombosis, inflammation, host defense or cancer metastasis [13], [14], [15]. P-selectin, overexpressed on activated platelets, is recognized by a natural ligand PSGL-1 (P-selectin glycoprotein ligand-1) expressed by lymphocytes via the tetrasaccharide sialyl LewisX [17]. Structural features of sialyl LewisX are essential for the recognition of PSGL-1: the hydroxyls of L-fucosyl and D-galactosyl, carboxylic group of sialic acid [16], and sulfated tyrosines in the protein backbone [18].

Fucoidan, heparin and dextran sulfate are sulfated polysaccharides which bind to P-selectin [19], [20] mimicking the interaction with PSGL-1. Low molecular weight fucoidan was formerly demonstrated to be of potential interest for revascularization in cardiovascular diseases [21], [22] and found as the most efficient glycosidic ligand of P-selectin in purified system and in human whole blood experiments [19]. The large amount of P-selectin in platelet-rich thrombi formed after atherosclerotic plaque rupture or erosion makes it a good target for fucoidan.

In this context, P-selectin appears as a good candidate target for the diagnosis of atherosclerosis and a contrast agent able to bind to P-selectin, i.e. vectorized by fucoidan to activated platelets, would efficiently enhance the detection of early thrombus formation.

1.3 Magnetic resonance imaging

MRI is one of the imaging modalities used in this work. One can use MRI like X-ray imaging to measure the artery wall thickness and to assess the blood flow. But one can also use a magnetic contrast agent. The sensitivity to the contrast agent is proportional to the number of magnetic atoms, not the volume of the observed region. If the agent is very specific of a pathology, it will make a bright localized source regardless of its size. This is exactly what we want to do here: to have a contrast agent which binds to the early stages of atheroma that we can detect in a non-invasive manner by MRI.

The magnetic properties of a nucleus are characterized by its spin. Each nucleus acts like a tiny magnet and therefore can be represented by a vector (figure 1.2). Normally, the direction of the spin vector is random. As a consequence, in a large collection of nuclei, the sum of all the spin vectors – called net magnetization - is zero.

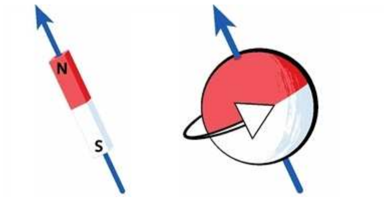

Figure 1.2: The spin of a nucleus is like a tiny magnet

When an external magnetic field $\vec{B}_0$ is applied, their spin vectors will align in a given direction which is determined by the laws of quantum physics.

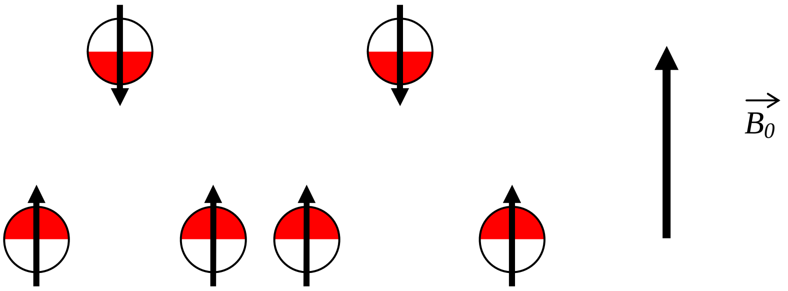

Figure 1.3: Spin vectors align in an external magnetic field

The hydrogen nucleus (namely a proton) is the most frequently imaged nucleus in MRI because it is present in biological tissues in great abundance and it gives a strong signal. The hydrogen nucleus can be in one of the two states (figure 1.3):

- The spin vector aligns with the external field. That corresponds to the lower energy level.
- The spin vector aligns against the external field. That corresponds to the higher energy level.

In fact, the spin vector is not perfectly parallel to the vector of the external magnetic field $\vec{B}_0$, it precesses about the axis of the external field (figure 1.4)

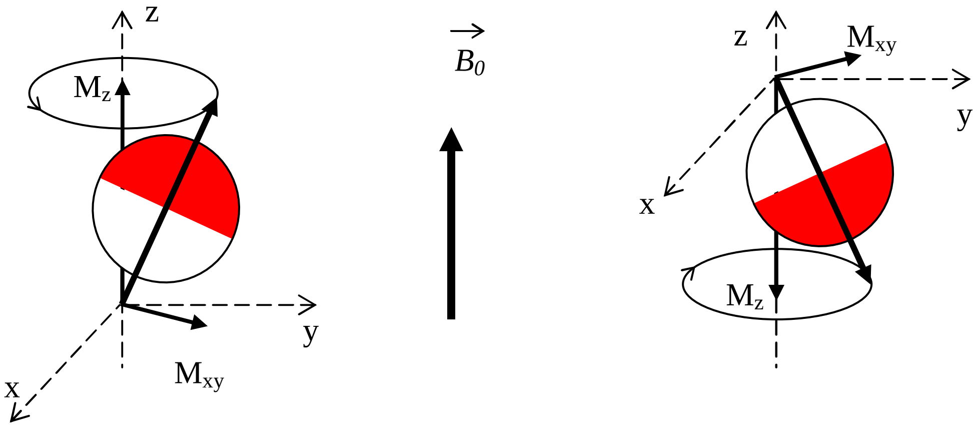

Figure 1.4: The precession of the spin vector

1.3.1 Larmor frequency - Excitation

The precession frequency – *Larmor frequency* – is:

$$\omega_0 = \gamma B_0 \tag{1.1}$$

Each isotope has its own Larmor frequency.

The magnetic vector of the spinning protons includes two orthogonal vector components: a longitudinal or Z component - M_z, and a transverse component, lying on the XY plane – M_{xy}. In the external magnetic field, there are more spins aligned with the field than spins aligned against the field. Therefore, the net magnetization has a longitudinal component aligned with $\vec{B}_0$. As spins do not rotate in phase, the transverse component of the net magnetization is null (figure 1.5).

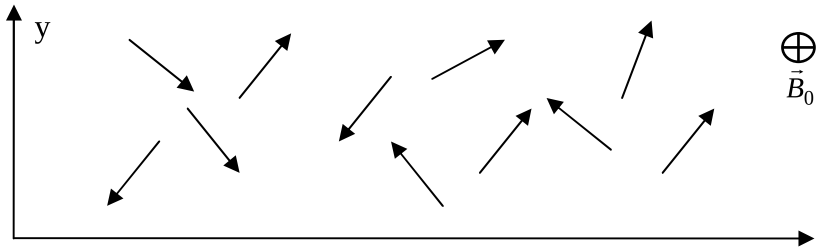

Figure 1.5: The random phases of the transverse component of spin vectors gives a null average magnetization

When hydrogen nuclei are excited by a radio frequency (RF) signal at the Larmor frequency, some nuclei can absorb RF energy and jump to a higher energy level – or change the direction of their spin vector to align with the external field. Two phenomena occur simultaneously:

First, all vector spins precess in phase => $M_{xy} \neq 0$

Secondly, the number of nuclei in the higher energy state increases. M_z decreases. If $M_z = 0$, the excited pulse is called a *90^0 RF pulse* because this pulse cause the net magnetization to flip 90^0 relative to the xy plane. If direction M_z changes to the opposite direction, the excited pulse is called a *180^0 RF pulse*.

1.3.2 Relaxation

When RF pulse terminates, the relaxation process begins. The relaxation combines two mechanisms:

On one hand, a nucleus emits a RF signal when returning to the lower energy level. M_z recovers its initial state. This is characterized by a *longitudinal magnetization recovery* time constant T_1. In general, T_1 values are longer at higher field strengths.

On the other hand, the vector spins get out of phase due to spin-spin interactions, M_{xy} decreases to null. This is characterized by a *transverse magnetization decay* time constant T_2.

T_1 is around one second while T_2 is a few tens of milliseconds. The values of T_1 and T_2 are widely different in different tissues. Imaging uses this difference.

1.3.3 Imaging

Now, how does the MRI work?

To get the 3D MRI, one must “cut” the body in several 2D slices

The spatial encoding

We know that only the RF frequency which coincides with the Larmor frequency has some effects on the nucleus. So the system applies a static magnetic field inside the imaging region with a known gradient. Different spatial slices correspond to different precession frequencies.

Then, we apply pulses of gradients of the magnetic field (gradient echo) or pulses of the RF excitation (spin echo) to select a narrow region.

This process can be repeated when the spins approximately returned to their thermal equilibrium. The whole body is scanned this way.

There is a very large number of possible magnetic and RF pulses configurations, and different manufacturers optimize their hardware and software differently.

Contrast

Contrast is caused by the differences in the MR signal. It helps to distinguish the different tissues. Contrast depends on tissue properties, the T_1, T_2 relaxation times and the proton density of the tissue, and on machine properties, the sequence of pulses parameters.

For example, we consider a spin-echo sequence, which is a common procedure. This sequence uses a 90^o RF pulse followed by an 180^o RF pulse. Spin-echo sequence has two main parameters:

- Echo Time (TE) is the time between the 90° RF pulse and MR signal sampling (the start of MR signal acquisition). The 180° RF pulse is applied at time TE/2.
- Repetition Time (TR) is the time between 90° RF pulses.

Table 1.1: Three weighted modes of a spin-echo sequence.

		TE	
		Long	Short
TR	Long	**T_2 – weighted** The contrast is caused mostly by the different T_2 values (tissue with a longer T_2 is brighter)	**Proton density – weighted** The contrast is caused mostly by the different of the proton density.
	Short	**No signal**	**T_1 – weighted** The contrast is caused mostly by the different T_1 values (tissue with a shorter T_1 is brighter)

In the clinical practice, the values chosen for TR and TE followed these rules [23]:

- TE is always shorter than TR
- A short TR = value approximately equal to the average T_1 value, usually lower than 500 ms
- A long TR = 3 times the short TR, usually greater than 1500 ms
- A short TE is usually lower than 30 ms
- A long TE = 3 times the short TE, usually greater than 90 ms

As an example, the figure 1.6 present a transversal image recorded from a rat we used for our experiments (see Chapter 5 for experimental conditions).

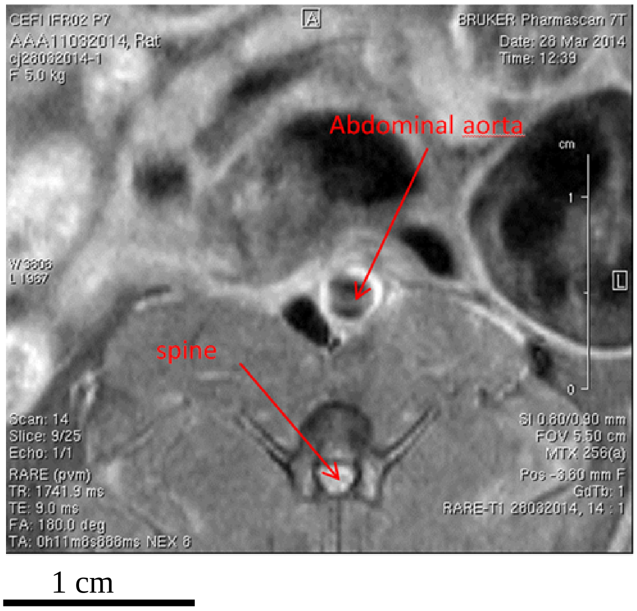
CEFI IFR02 P7
AAA11032014, Rat
cj28032014-1
F 5.0 kg
A
BRUKER Pharmascan 7T
Date: 28 Mar 2014
Time: 12:39
Abdominal aorta
cm
1
W 3808
L 1987
L
spine
0
Scan: 14
Slice: 9/25
Echo: 1/1
RARE (pvm)
TR: 1741.9 ms
TE: 9.0 ms
FA: 180.0 deg
TA: 0h11m8s888ms NEX 8
SI 0.80/0.90 mm
FOV 5.50 cm
MTX 256(a)
Pos -3.80 mm F
GdTb: 1
RARE-T1 28032014, 14 : 1
1 cm

Figure 1.6: transversal image of a rat abdomen. The parameters are mentioned on each side of the image: Magnetic field = 7 T, slice width = 0.9 mm, Matrix of the image 256x256, TR = 1742.9 ms, TE = 9 ms etc…

1.4 MRI contrast agent

MRI contrast agents are by definition designed to enhance the contrast. Their main effect is the shortening of the relaxation times T_1 and T_2 of the hydrogen nuclei of water molecules which surrounds them. The capability of shortening the T_1 and T_2 relaxation times is described by the term "relaxivity". The relaxivity is the increase of longitudinal or transversal relaxation rate, $1/T_1$ or $1/T_2$ respectively, and is denoted by r_1 and r_2. The relaxivity of the contrast agent is the increase of the relaxation rate due to the contrast agent per unit of concentration of the agent. In presence of a contrast agent, the observed relaxivity ($1/T_x$, with x=1 or 2) is the sum of the intrinsic relaxivity of the examined aera in absence of contrast agent ($1/T_x^0$) and that of the contrast agent ($1/T_x^a$). The slope of the curve obtained by plotting $1/T_x$ vs the concentration of agent gives the relaxivity r_x of the contrast agent [24], [25]. In general, r_1 decreases when the magnetic field becomes stronger, whereas r_2 tends to remain constant or even can increase somewhat [25].

The ratio between the relaxation rates r_2 and r_1 determines whether a contrast agent is suitable for the enhancement of T_1-weighted or T_2-weighted imaging.

1.4.1 T_2 contrast agent

The most effective T_2 contrast agent are nanoparticles of magnetite (Fe_3O_4) or maghemite (γ-Fe_2O_3). These are also called superparamagnetic contrast agents [26], [27]. With a diameter ranging from 4 nm to 50 nm, the superparamagnetic agents contain thousands paramagnetic Fe ions (Fe^{2+} and/or Fe^{3+}). Therefore it has a large magnetic moment in an external magnetic field. As a result, superparamagnetic agents introduce strong local field gradients, which accelerates the dephasing of the surrounding water protons [28], i.e induces a shortening of T_2 and an increase of r_2.

Depending on their size, their crystalline structure, and their coating, superparamagnetic agents are called: superparamagnetic iron oxide particles (SPIO), ultrasmall superparamagnetic iron oxide particles (USPIO), very small superparamagnetic iron oxide particles (VSOP), monocrystalline iron oxide particles (MION) and cross-linked iron oxide particles (CLIO) [29], [30], [31], [32], [33].

1.4.2 T_1 contrast agent

Gadolinium ion (Gd^{3+}) is the most common T_1 contrast agent used in the clinic environment because it has a high paramagnetic moment. However the free ion Gd^{3+} is toxic for living tissue like most free ion metals are. Therefore, gadolinium ions need to coordinate with a suitable ligand to form a nontoxic complex. The figure 1.7 [34] present some of the most common commercial gadolinium-based contrast agents: Gd-DTPA (Magnevist), Gd-DOTA (Dotarem), and Gd-HP-DO3A (Prohance).

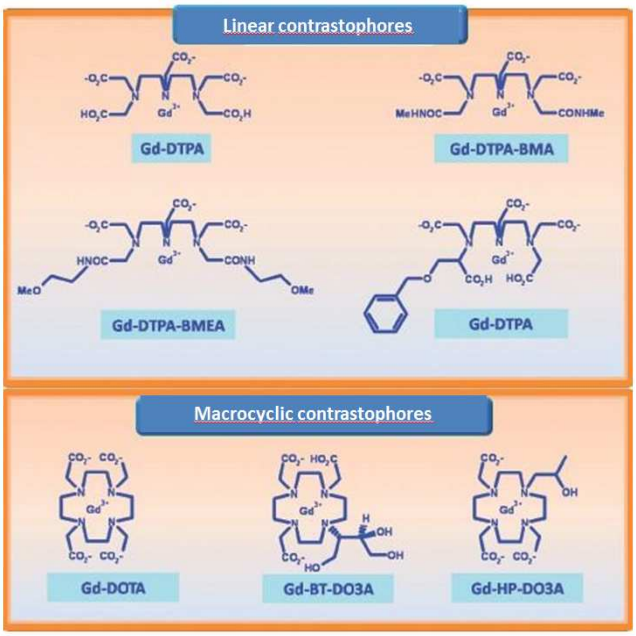

Figure 1.7: Some of the most widespread gadolinium based MR contrast agents

The relaxation mechanism of T_1 contrast agent is described by Solomon-Bloembergen-Morgen (SBM) theory [35], [36], [37]. The relaxation is mainly due to the interaction between Gd^{3+} and water molecules, which directly coordinate with Gd^{3+} ions. This interaction is characterized by the exchange correlation time τ_m. In the complex, Gd^{3+} usually has one directed coordination with a water molecule. The rotation of a complex is also important: because the rotation frequency of Gd complexes is fast compared to the Larmor frequency, the slowing down of complexes closer to the Larmor frequency improves the relaxation. The effect of the complex rotation is characterized by the rotational correlation time τ_r. One way to improve the relaxation of Gd complexes is to link many Gd chelates on a macromolecule. The consequences are both the increase of the rotational correlation time and that of the local concentration of Gd^{3+} ions.

1.4.3 Bimodal MRI/optical contrast agents

In MRI, the use of contrast agents enables image enhancements and therefore opens the way towards more reliable diagnosis. Nevertheless, the best MRI resolution is a few dozen micrometers [2] and such a high resolution requires a long acquisition time. This limitation is not suitable with the study of the distribution of the MRI agents in small volumes like in a single cell or even into the layers of a small artery wall. Yet, if we want to study why a given agent exhibits some affinity for a pathologic tissue, or if we want to modify the agent in order to increase this affinity, we need a very high resolution imaging method. The resolution of

MRI is far worse than the resolution of optical microscopy. Of course, optics is a good imaging method!

To overcome this obstacle, many efforts were done to synthesize fluorescent MRI agents. Many different fluorophores can be linked with MRI agents [38], [39]. However, biological tissues are naturally fluorescent too. Of course, biological tissues are not intensely fluorescent, but modified MRI agents aren't very bright either. To make things worse, emission wavelengths of the main fluorophores used for agents fall in the emission regions of the tissues autofluorescence, making it sometimes difficult to interpret the images. Hence we need to develop more sophisticated markers, for example fluorophores capable of emitting in the near infrared where the fluorescence of the tissues is absent [40]. Another way to solve this issue is to use fluorescent emitters which decay very slowly, a lot longer than the time constant of the autofluorescence decay. Lanthanide complexes, particularly europium and terbium, have been used for forty years in analytical biochemistry [41], [42] with several advantages compared to purely organic fluorophores [43], [44]: very long luminescence decay (some hundred microseconds to some millisecond), better photostability, narrow emission lines and large Stokes shift. These compounds can therefore achieve fluorescence optical imaging with a time-resolved emission in the visible (green light for terbium and red light for europium) easily discriminated from the background noise.

Gadolinium, europium and terbium are lanthanides and have the same physicochemical and biological properties. An MRI contrast agent which would have some of its Gd^{3+} ions replaced by Eu^{3+} or Tb^{3+} ions would make possible a time-gated fluorescence microscopy in the visible wavelengths. Because of the similarity between the lanthanides, and because the metallic ions are shielded from the biological activity, the modified optically active agent can't be noticeably different chemically from the pure MR one. Therefore, any useful information collected using this modified agent remains pertinent for the original agent.

1.5 Optical properties of terbium (Tb3+) and europium (Eu3+) ions

1.5.1 Absorption spectra

The absorption spectra of free ions Gd^{3+}, Eu^{3+} and Tb^{3+} in aqueous solution are presented in the figure 1.8, 1.9, 1.10 [45, p. 179]. The vertical axis represents the molar absorptivity ε (also called molar absorption coefficient or molar extinction coefficient) of the solution. The molar absorptivity is defined by the formula [46, p.33]

$$\varepsilon = \frac{1}{cd}\log\frac{I_0}{I} \ \ [\mathrm{L.mol^{-1}cm^{-1}}] \tag{1.1}$$

where I_0 is the intensity of the incoming light, I is the intensity of the outgoing light, c is the concentration in moles per liter, d is the path length in centimeters. The relation between the molar absorptivity and the absorption cross-section σ is [46, p.33]

$$\sigma = 3.82\times10^{-21}\varepsilon \ \ [\mathrm{cm^2}] \tag{1.2}$$

The top horizontal axis represents the wavelength in nanometers. The bottom horizontal axis represents the wave number in cm^{-1}.

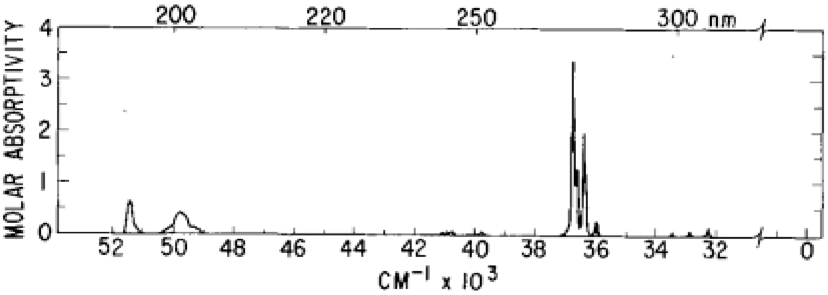

Figure 1.8: The absorption spectrum of Gd3+ in an aqueous solution

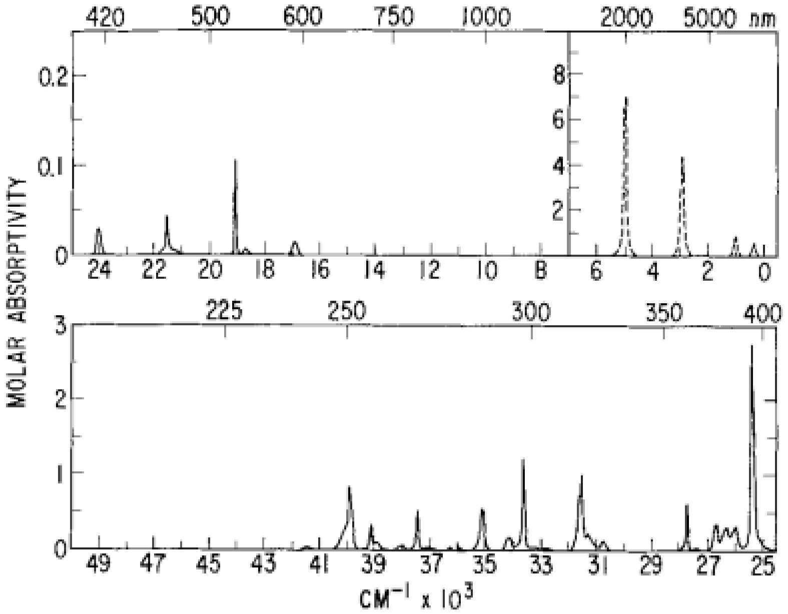

Figure 1.9: The absorption spectrum of Eu^{3+} in an aqueous solution

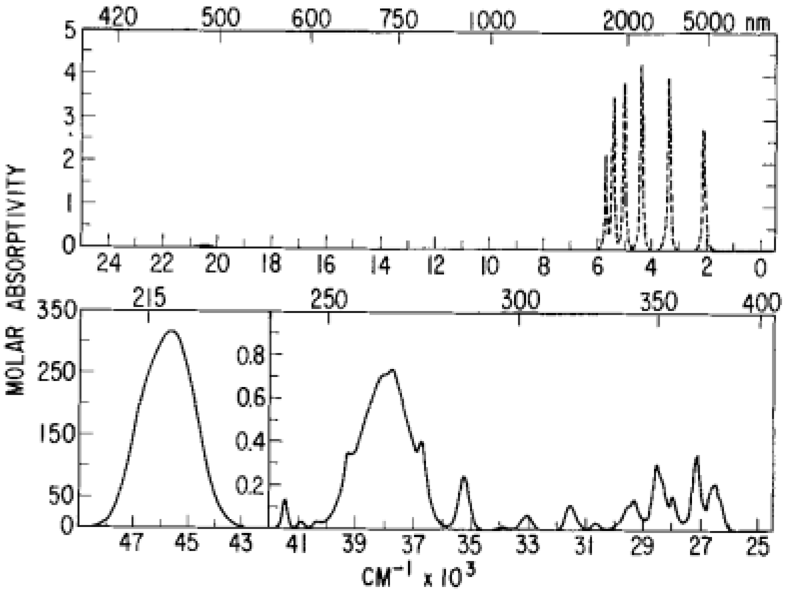

Figure 1.10: The absorption spectrum of Tb^{3+} in an aqueous solution

It is clear that Gd^{3+} only absorbs in the middle UV light. This is not convenient because exciting it requires a quartz optical system and a powerful source in a region where few lasers are available. On the contrary, Eu^{3+} and Tb^{3+} have some wide band absorption in the near UV region. They can be excited by a very compact light source like a LED or a laser diode.

It is worth to remark that the molar absorptivity of Eu^{3+} and Tb^{3+} is very much smaller than the one of the common fluorophores like Carbostyryl 7 ($1.46 \times 10^4 L.mol^{-1}cm^{1-}$ @ 350 nm), Coumarin 4 ($2.10 \times 10^4 L.mol^{-1}cm^{1-}$ @ 372 nm), DASPI ($3.83 \times 10^4 L.mol^{-1}cm^{1-}$ @ 372 nm) … [46]. As a result, the fluorescent intensity we can expect from Eu^{3+} and Tb^{3+} is very low. This is the main obstacle that we must overcome when designing applications with Eu^{3+} and Tb^{3+}.

One straightforward way to increase the fluorescent intensity collected from Tb^{3+} and Eu^{3+} ions is to increase their local concentration. They can be added like dopants in a nano particle like yttrium vanadate [47], [48] or coated on the surfaces of SiO_2 nano particles [49].

Fluorescence resonance energy transfer (FRET) is also used to increase the absorption of excitation light. The excitation light does not excite directly the lanthanide ions. It excites particles which have a large molar absorptivity, and then these particles transfer the excited energy to the nearby lanthanide ions [49], [50], [51], [52].

1.5.2 Emission spectra

Figure 1.11 shows the energy level diagram of lanthanide ions in aqueous solution. It is clear that the emission peak of Gd^{3+} is around 310 nm. Acquiring this wavelength require also quartz optical system and UV detector. Therefore, Gd^{3+} is really not suitable for fluorescent microscopy imaging, both from the absorption and emission points of view.

Eu^{3+} and Tb^{3+} have emission in the visible region as shown in the figure 1.12. This is adapted to a conventional microscope.

It should be noted that while the emission spectra of Tb^{3+} is almost not changed with different ligands, the relative intensity of peaks in the spectra of Eu^{3+} depends strongly on the ligands (figure 1.13 and [53]).

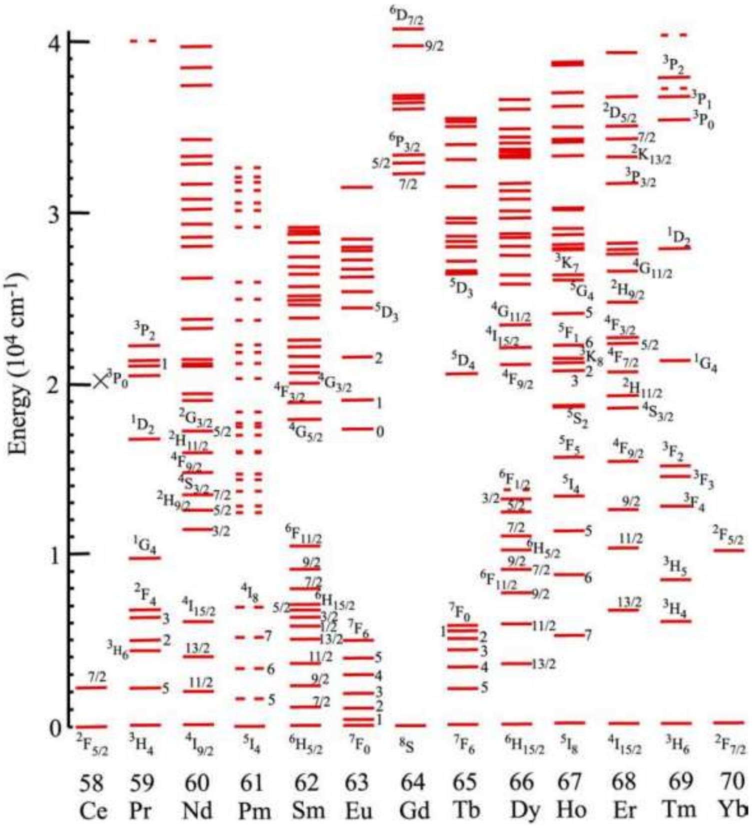
Energy (10⁴ cm⁻¹)
0
1
2
3
4
²F5/2
³H4
⁴I9/2
⁵I4
⁶H5/2
⁷F0
⁸S
⁷F6
⁶H15/2
⁵I8
⁴I15/2
³H6
²F7/2
58 Ce
59 Pr
60 Nd
61 Pm
62 Sm
63 Eu
64 Gd
65 Tb
66 Dy
67 Ho
68 Er
69 Tm
70 Yb
⁵D3
⁵D4
⁵D0
⁶D7/2
⁶P3/2
³P2
³P0
¹D2
¹G4
²F5/2

Figure 1.11: Dieke diagram of free lanthanide ions [54, p.8]

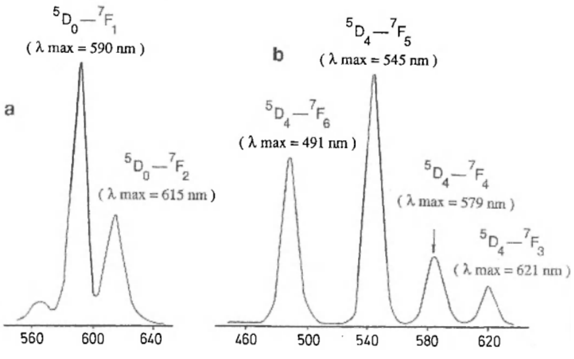

Figure 1.12: Emission of Eu^{3+} (a) and Tb^{3+} (b) in an aqueous solution [55]

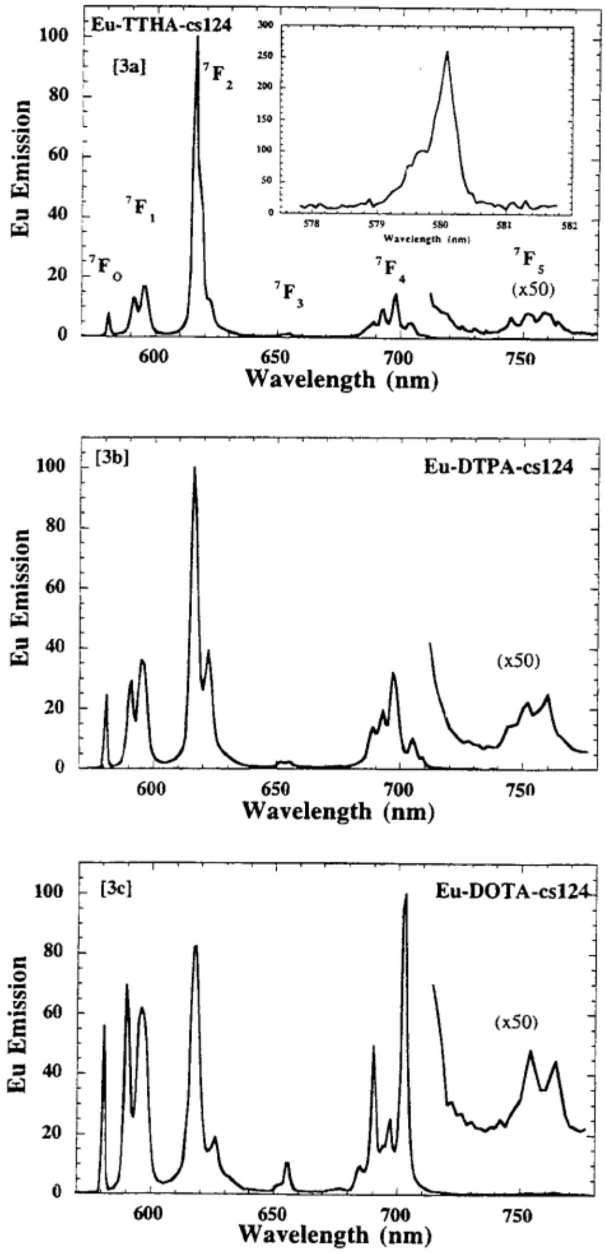

Figure 1.13: Normalized emission spectra of europium complexes [56]

1.5.3 Fluorescent lifetime

The table 1.2 shows the very long fluorescent lifetimes of Eu^{3+} and Tb^{3+} ions. They last approximately 10 milliseconds. In fact, fluorescent lifetimes of these ions in aqueous solution are much shorter. They last only about 0.45 milliseconds for Tb^{3+} and 0.13 milliseconds for Eu^{3+} [57], [58], [53], [59]. The interaction of Tb^{3+} and Eu^{3+} with water molecules is the one reason [57], [60], [58]. Therefore, the binding of Eu^{3+} and Tb^{3+} with a ligand is a good solution to eliminate this interaction.

The table 1.3 shows the fluorescent lifetime and quantum efficiency of Eu^{3+} and Tb^{3+} in H_2O and D_2O solutions. It is clear that Eu^{3+} and Tb^{3+} in complexes have longer fluorescent lifetimes and therefore a higher quantum yield. One can note that the data shows that the increase of the quantum yield usually is higher than the increase of the fluorescent lifetime.

Table 1.2: Calculated radiative lifetimes of excited states of lanthanide ions in an aqueous solution [54, p. 197]

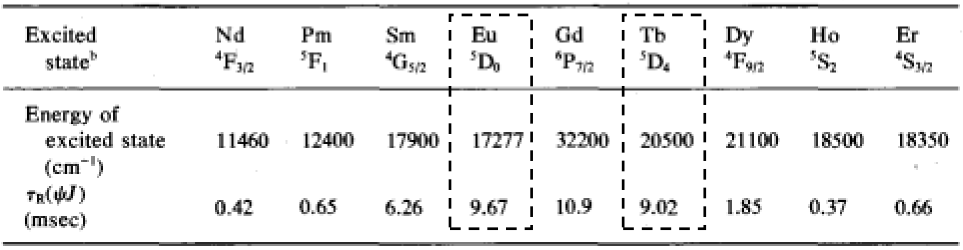

Excited state[b]	Nd $^4F_{3/2}$	Pm $^5F_1$	Sm $^4G_{5/2}$	Eu $^5D_0$	Gd $^6P_{7/2}$	Tb $^5D_4$	Dy $^4F_{9/2}$	Ho $^5S_2$	Er $^4S_{3/2}$
Energy of excited state (cm^{-1})	11460	12400	17900	17277	32200	20500	21100	18500	18350
$\tau_R(\psi J)$ (msec)	0.42	0.65	6.26	9.67	10.9	9.02	1.85	0.37	0.66

Table 1.3: The fluorescent lifetimes and quantum yields of Eu^{3+} and Tb^{3+}.

	H_2O		D_2O		Ref.
	Fluorescent lifetime (ms)	Quantum yield (%)	Fluorescent lifetime (ms)	Quantum yield (%)	
Eu^{3+} (aqueous)	0.13	*0.9*	1.65	*11.2*	[58]
Eu^{3+} (aqueous)	0.10		2.27		[59]
EuEDTA	0.26		2.05		
Eu^{3+} (aqueous)		*0.65*			[55]
Eu^{3+} (aqueous)	0.11		2.86		[53]
EuDOTA	0.60		2.13		
EuDPA	1.54		2.94		
EuEDTA	0.34		2.10		
EuDTPA	0.63		2.27		
EuDTPA-cs124	0.62	*16.7*	2.42	*65.2*	[50]
EuTTHA-cs124	1.19	*42.3*	1.79	*63.6*	
EuDOTA-cs124	0.62	*13.7*	2.25	*49.7*	
Tb^{3+} (aqueous)	0.48	*3.4*	2.39	*16.7*	[58]
Tb^{3+} (aqueous)	0.43		3.3		[59]
TbEDTA	0.41		3.20		
Tb^{3+} (aqueous)	0.47		1.3		[57]
Tb^{3+} (aqueous)		*2.9*			[55]
TbDTPA-cs124	1.55	*48.6*	2.63	*81.8*	[50]
TbTTHA-cs124	2.15	*73.0*	2.37	*80.6*	
TbDOTA-cs124	1.54	*43.6*	2.61	*74.9*	
Tb(DTPA-2pAS)	1.45	*7.67*			[61]

We can increase the signal to noise ratio (SNR) of Eu^{3+} and Tb^{3+} ions fluorescence in an organic medium by taking advantage of their long fluorescent lifetimes. Organic matter emits a strong autofluorescence under UV illumination. Its fluorescent lifetime is several nanoseconds. It is very short compared to the fluorescent lifetimes of Eu^{+3} and Tb^{3+}. Therefore, if we acquire the Eu^{3+} and Tb^{3+} fluorescence emission after the decay of the tissue's autofluorescence we can obtain a considerably increased SNR [38], [41], [62], [63], [64], [65] despite a lower total energy capture (we lose the fluorescence emitted at shorter times). This technique is named time-resolved or time-gated fluorescence. The principle of the time diagram for this technique is shown in the figure 1.12.

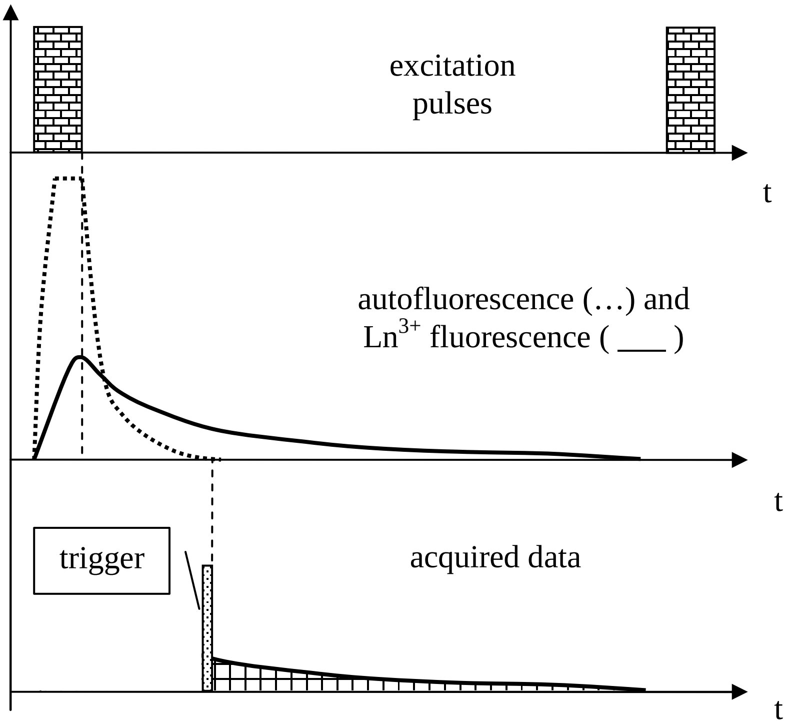

Figure 1.14: Principle of time-gated fluorescence

Chapter 2

Microscope system setup for time-gated fluorescence

We built a microscope system designed to acquire low intensity, long lifetime, fluorescence images of artery specimens labeled by the P717Tb complex. The time-gated technique is used to discard the strong "fast" autofluorescence which comes from organic samples under UV light.

This system is capable to measure the fluorescent spectrum of artery specimens excited by UV light.

For colorized samples, the system supports a color imaging acquisition.

2.1 The microscope

We must excite the samples fluorescence with UV light. Therefore, all the optical elements in the excitation path must transmit UV with a good efficiency and emit minimal parasitic fluorescence. Samples fluorescence is emitted in the visible region. It is mainly green. Ordinary microscope optics is suitable here. We also wish to be able to perform tissues identification, in order to determine where the fluorescent marker is fixed. An anatomo-pathologist must have a good quality color image for this identification. If the color and fluorescent image are acquired exactly by the same experimental setup, it is easier to make the correspondence between the two images. No software rescaling, translation, etc is necessary.

An inverted microscope perfectly corresponds to all these needs. Therefore, the microscope fluorescence system was built from an Axio Observer A1m inverted microscope. Above the sample's platform, we are free to build the illumination system without constraints about shape and size. All the microscope functions are below the sample's platform. Fluorescence is seen as 'transmitted' through the sample. We still need a filter to block UV propagation into the microscope system, somewhere after the sample (labeled F2 in the following, see figure 2.14). White light illumination, for the color image, comes from below and the color image is "reflected' from the sample. The image path and camera is the same for fluorescence and color images.

This microscope has two output ports. Four objective lenses EC Epiplan whose magnifications are respectively: 10x, 20x, 50x and 100x.

2.2 The laser

The terbium ions require an excitation by UV light as described in the previous chapter. We have chosen a laser diode as a source for excitation because it possesses valuable properties: it's compact, operates in continuous wave and pulsed modes, its output power can be easily adjusted and it can be synchronized with other parts of system.

We bought a Laser Stradus 375 made by Vortran Medical Technology, Inc. Some parameters of this laser are shown in the table 2.1:

Table 2.1: Specifications of the Vortran UV laser

Center wavelength (nm)	*371*
FWHM (nm)	2
Power output (mW, CW mode)	15
Spatial mode	TEM_{00}
Beam diameter (mm, $1/e^2$)	~ 1.3
Beam divergence (mrad)	~ 0.5
M^2	< 1.25
Beam circularity	> 90%
Polarization extinction ratio	> 100:1
Power stability (over 24 hours)	< 0.5%
Digital modulation	200 MHz
Digital rise time	< 2ns
Analog modulation	500 kHz
Analog rise time	< 0.7 µs
Operating temperature	10^oC to 45^oC

Stradus TM 375
VORTRAN
LASER TECHNOLOGY, INC.
SMB
USB
LASER INPUT
MADE IN USA

Figure 2.1: The UV laser head

We measured the emission spectrum of this laser on an EG&G 1461 digital triple grating spectrometer. It shows only one narrow peak at 371 nm (figure 2.2). This wavelength is suitable to excite terbium ions.

However, we encountered two problems.

The first one was easily solved: the laser emits some visible light at the wavelength we want to observe. Maybe it comes from some fluorescence from the laser's materials; maybe it's due to some emission between junctions in the laser. In any case, a good filter (labeled F1 in the following, see figure 2.14) centered on the emission wavelength should rule out this parasitic emission.

The second problem was a little more difficult to deal with: when the laser pulse is switched off, UV light at 371 nm is still emitted by the laser chip (figure 2.3). This light emission decays during some hundred microseconds. It decreases faster than an exponential decay function. This residual UV light is extremely weak compared to the ordinary UV laser emission, but it can cause autofluorescence in biological samples and on some of the glass optics in the microscope. Autofluorescence is a lot more intense than our desired signal and can overwhelm the signal from terbium ions. One mechanic chopper must be used to eliminate the residual light (see section 2.4)

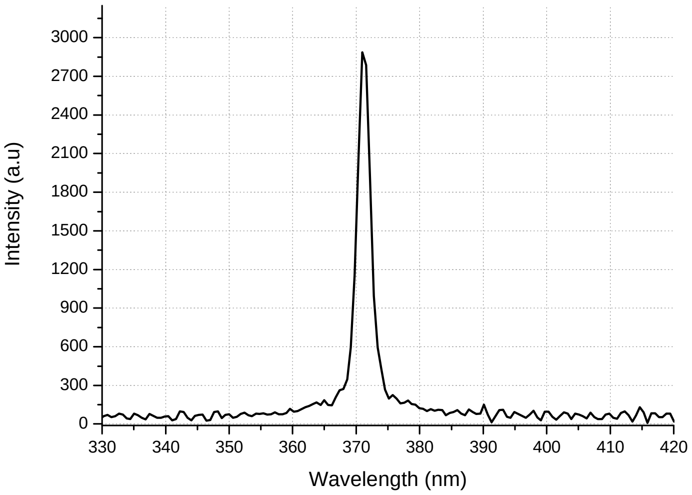

Figure 2.2: The UV laser emission spectrum

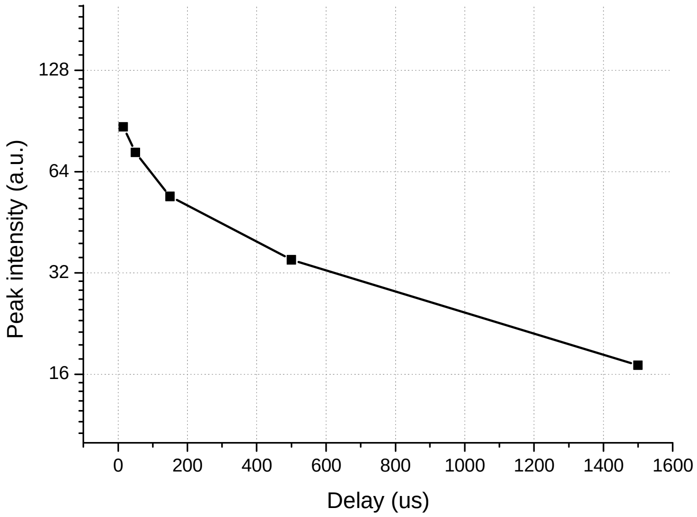

Figure 2.3: The residual UV light at 371 nm (in a logarithmic scale) .

The absorption of energy by the terbium ions is very low; moreover, the power of our UV laser is low too. Its maximum power in continuous mode is 15 mW. The specimens is only receive 5 mW due to losses on the filter F1 and the focus lens.

The laser beam diameter (FWHM) is approximate 0.76 mm, so the average intensity on a specimen is only 1W/cm^2.

A single focusing lens is used to concentrate laser light on a specimen. The size of the laser spot on the specimen is adjusted by changing the distance between the lens and the specimen. That's the way we used to choose the adequate light intensity by defocusing.

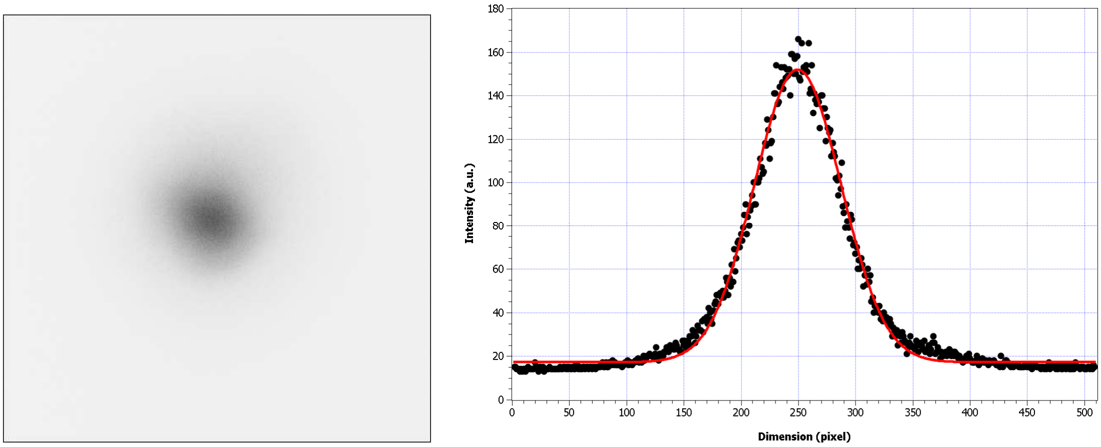

(a) (b)

Figure 2.4: Image of the laser spot at the sample's position

The figure 2.4a shows the image of a fluorescent spot of terbium in a solution when it was excited by the UV laser. This was also the real image of laser spot's size. The chart in the figure 2.4b is the power distribution of the laser beam (vertical cut in figure 2.4a). We fit this data to a Gaussian function

$$y = y_0 + A\exp\left(-\frac{(x - x_0)^2}{2w^2}\right)$$

and the comparison gives us $w = 38.0 \pm 0.2$ pixels. The FWHM diameter equals 89.3 pixels.

By taking a standard image, we estimate that the distance between two pixels is equivalent the distance of 0.7 micrometer on the specimen. Therefore, the FWHM diameter of laser beam is approximate 62 micrometer. The average intensity on a specimen now is 182 W/cm^2.

The field of view of the objective 20x is approximately 1 mm. Therefore, only one small part of specimen is excited. To get a full image of specimen, we need scan the laser spot on the specimen. The image area around each excited position is collected. Those data will be used to build by software the whole fluorescent image of the specimen.

2.3 The filters

The first single filter (F1) eliminates the parasitic visible light from the excitation laser. We purchased it from Horiba, code EM XF01 330WB60. The transmission spectrum of this filter is shown in the figure 2.5

The second single filter (F2) is the Semrock filter with has the code LP02-442RS-25. It is a broadband high-pass filter. This filter is placed after the microscope objective to block the UV laser light (317 nm) from propagating further into the microscope and possibly creating autofluorescence in it. This filter allows the transmission of the fluorescence emitted by the terbium ions in the visible region. The transmission spectrum of this filter is shown in the figure 2.6.

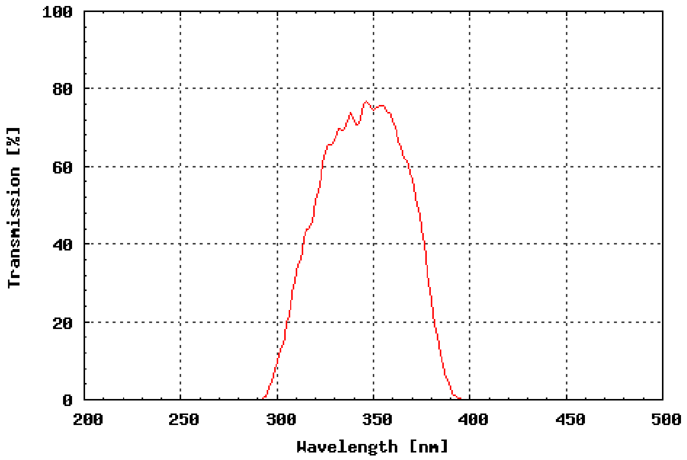

Figure 2.5: The transmission spectrum of the EM XF01 330WB60 filter

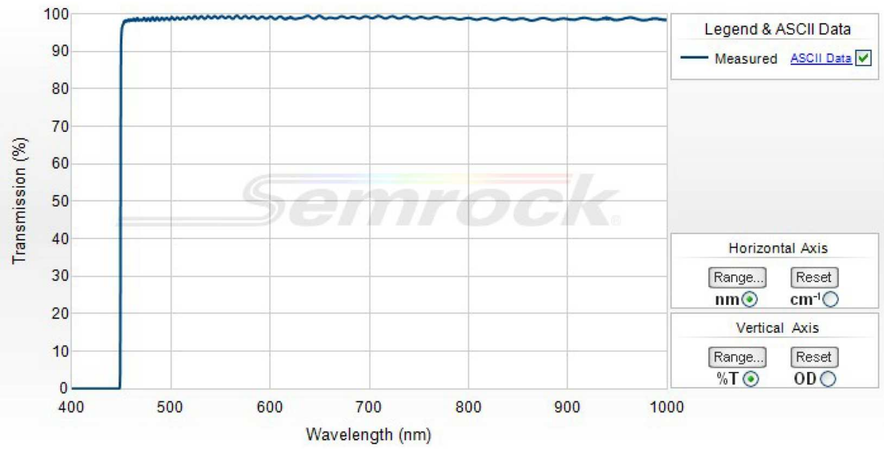

Figure 2.6: The transmission spectrum of the LP02-442RS-25 filter.

The filter set (FS) includes three optical cast plastic color filters from Edmund Optics. The colors transmitted by those filters are successively red, green and blue. We use them to synthesize a color image, as we'll explain below. We place them between the white light halogen lamp of the microscope and specimens. The color of the illumination light is chosen by selecting one of those filters. For each color, the camera gives us a "gray scale" image. Then the three gray scale images, corresponding to the three primary colors of the RGB image, are assembled with the corresponding weights. The result is a real color image of specimens (see figure 2.7)

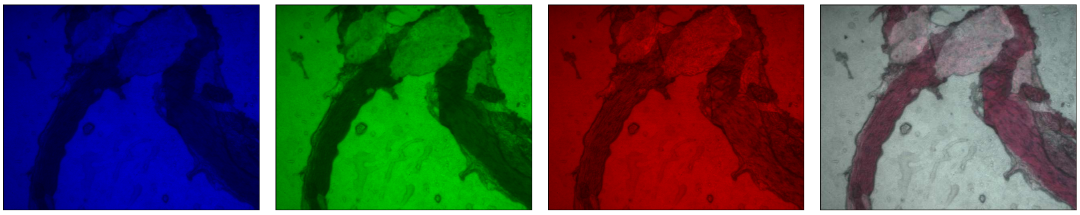

Blue filter + Green filter + Red filter => Color image

Figure 2.7: The process to acquire the color image of a specimen

2.4 The chopper

The mechanic chopper was made by EG&G Instruments (model 651). eliminates the residual light of UV laser. Our working frequency is 80 Hz. The TTL timer signal is used as the master synchronizing pulse of the whole system.

2.5 The EMCCD camera

Since the power of the fluorescence signal of the metallic ions is low, we need a very good camera to get a correct signal to noise ratio. The camera we have chosen is an Andor iXon3 DU-897D. We estimated it could be sufficient to acquire the fluorescent image of artery specimens when they are labeled by our bimodal contrast agent. This camera has an up to 1000x electron multiplication gain and its sensor can be cooled down to -100^{o}C to get a very low dark current noise. Therefore, it can acquire a very low intensity image. The camera module is fitted with an external trigger port to allow the camera to be synchronized with other parts of the system like the chopper and the UV laser diode. We give more details about the specifications of this camera in the table 2.2. The spectrum sensitivity of the camera covers completely the visible range with a high quantum efficiency. Its maximum sensitivity is obtained from 500 nm to 700 nm. That matches very well the emission spectrum of terbium ions (figure 2.8).

Table 2.2: Specifications of the Andor iXon3 DU-897D camera

Sensor	CCD back illuminated standard AR coated
Blemish specification	Grade 1 sensor (CCD97)
Active pixels	512 x 512
Pixel size (μm)	16 x 16
Image area (mm)	8.2 x 8.2 (100% fill factor)
Cooling - Air cooling (^{o}C) - Liquid cooling (^{o}C)	- 80 - 95
Thermostatic precision (^{o}C)	± 0.01
Digitalized resolution (bit)	16
Triggering	Internal External External Start External Exposure Software Trigger
Dark current (e-/pixel/sec) @ -85°C	0.001
Spurious background (events/pix) @1000x gain / -85°C	0.0018
Active area pixel well depth (electrons)	180,000
Gain register pixel well depth (electrons)	800,000
Pixel readout rates (MHz) - Electron Multiplying Amplifier - Conventional Amplifier	 17, 10, 5, 1 3, 1 & 0.08
Vertical clock speed (μs)	0.3 – 3 (variable)

Read noise (e-) @10 MHz through EMCCD amplifier - without electron multiplication - with electron multiplication	65 < 1
Linear absolute electron multiplier gain	1 - 1000 times via RealGain™ (calibration stable at all cooling temperatures)
Linearity	> 0.99

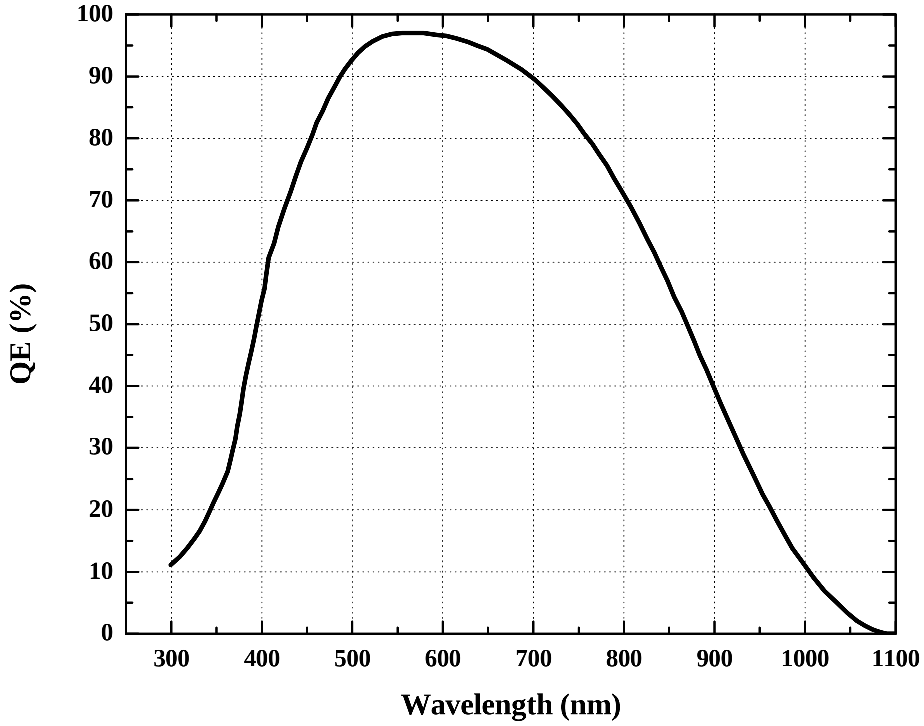

Figure 2.8: quantum efficiency spectrum of the Andor iXon3 DU-897D camera

This EMCCD camera have two major acquisition modes: Frame transfer mode (FT) and Non frame transfer mode (NFT)

Frame Transfer Mode

In Frame Transfer acquisition mode, the iXon3 EMCCD camera can deliver its fastest performance while maintaining an optimal signal to noise ratio. It achieves this through simultaneously acquiring an image onto the image area while reading out the previous image from the masked frame storage area. Thus there is no time wasted during the readout and the camera operates with what is named as a 100% ‘duty cycle’.

Non-Frame Transfer Mode

The camera can also operate as an FT CCD in a Non-Frame Transfer (NFT) mode. In this mode of operation, an FT CCD acts much like a standard CCD.

Since this camera is one of the most important components of this experiment, and incontestably it is the most complex one, it deserves its own chapter 3 below. There, we will present extensively its rich possibilities and some nice “tricks” we could do with it!

2.6 The shutter

In order to avoid parasitic light accumulation, the camera needs a shutter to protect it. We should open the shutter just before starting the image acquisition, and close it at the end. The shutter requires neither a very fast transition slope nor an extraordinary frequency. Therefore, we used for this purpose a hard disk voice-coil actuator. We attached a razor blade where we usually find the read/write heads. Every experiment has its own characteristic sound. The regular ‘tchack’, ‘tchack’, ‘tchack’ of the actuator became the emblematic sound of this system.

2.7 The spectrometer

We built a spectrometer, added to the microscope, in order to measure the emission spectra of specimens excited under UV light. Detector is a camera. The high sensitivity of this camera allows us to acquire the spectrum of very low intensity light. We use this spectrometer as a control device. With it we can ensure that the collected light indeed corresponds to the terbium emission spectrum. Figure 2.11 shows the scheme of the spectrometer.

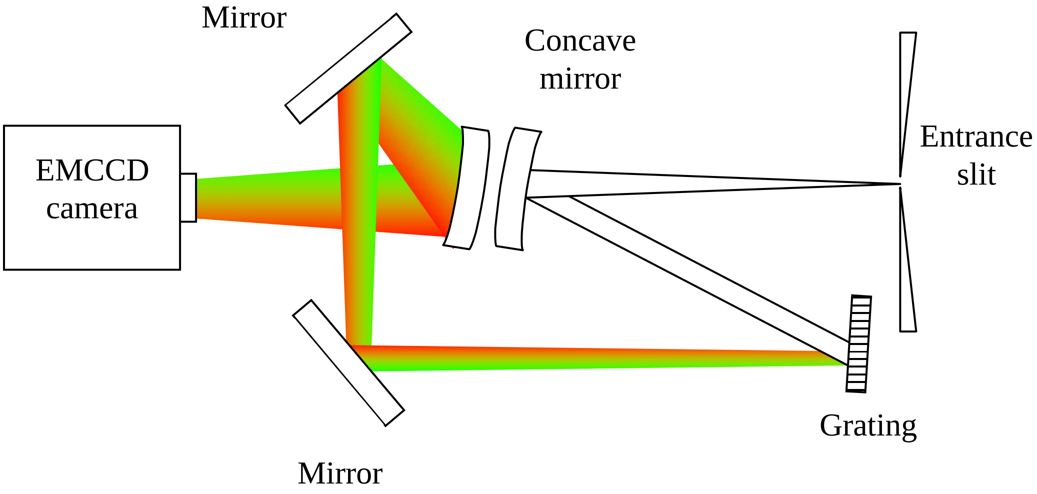

Figure 2.11: The spectrometer.

2.8 Electrical synchronization

The time-gated technique requires a very good synchronization between the chopper, the UV laser diode and the cameras. We also want to adjust and modify the synchronization’s parameters, for example in order to add another function like the spectrometer. A software on a ordinary PC may offer the maximum freedom, but no random is allowed and it’s extremely difficult to guarantee a real-time processing of the synchronization events when using a multitasking operating system. We used a standard technique: a dedicated microcontroller. The synchronization is controlled by a Picdem FS USB demo board purchased from the Microchip Company.

The PICDEM™ FS-USB is a demonstration and evaluation board for the PIC18F4550 family of Flash microcontrollers with full speed USB 2.0 interface. The board contains a

PIC18F4550 microcontroller in a 44-pin TQFP package, representing the superset of the entire family of devices offering the following features:

- 48 MHz maximum operating speed (12 MIPS)
- 32 Kbytes of Enhanced Flash memory
- 2 Kbytes of RAM (of which 1 Kbyte dual port)
- 256 bytes of data EEPROM
- Full Speed USB 2.0 interface (capable of 12 Mbit/s data tranfers), including FS-USB transceiver and voltage regulator

The demonstration board provides the following functions:

- 20 MHz crystal
- serial port connector/interface (for demonstration of migration from legacy applications)
- connection to the MPLAB® ICD 2 In Circuit Debugger
- voltage regulation, with the ability to switch from external power supply to USB bus supply
- expansion connector, compatible with the PICtail™ daughter boards standard
- temperature sensor TC77 (connected to the SPI bus)
- potentiometer (connected to RA0 input) for A/D conversion demonstrations
- 2 LEDs for status display
- 2 input switches
- reset button

The board comes pre-loaded with a USB bootloader. The PIC18F4550 can be re-programmed in circuit without an external programmer, but we used a full development system for maximum flexibility and ease of use.

2.9 How to get a fluorescent image?

The complete time-gated fluorescent microscope is shown in the figure 2.13. Its scheme is presented in the figure 2.14.

Because the system uses time-gated technique to enhance the signal to noise ratio, the time synchronization between the chopper, the laser and the camera is very important. The figure 2.12 shows the time frame for each device.

1. While the chopper opens, the laser turns on. Specimen is illuminated.
2. The laser turns off; chopper closes to block the residual UV light of laser as it decays.
3. The camera shutter opens at this time. The exposure process begins at the same time.
4. When the exposure process is completed, the camera shutter closes and read-out process is started.

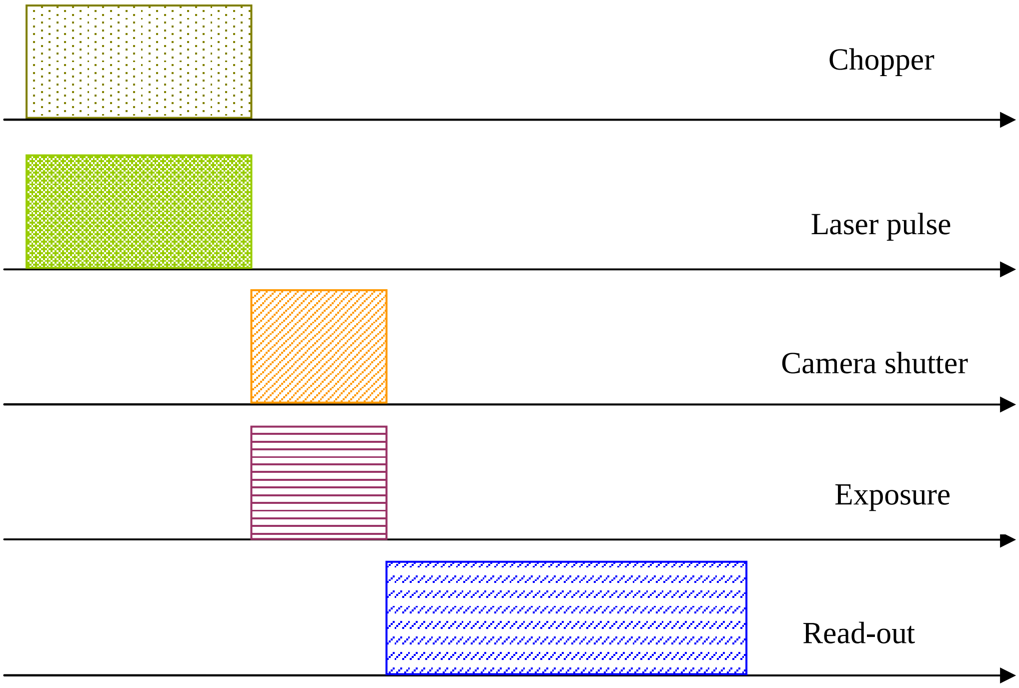
Chopper
Laser pulse
Camera shutter
Exposure
Read-out

Figure 2.12: Time synchronization of system

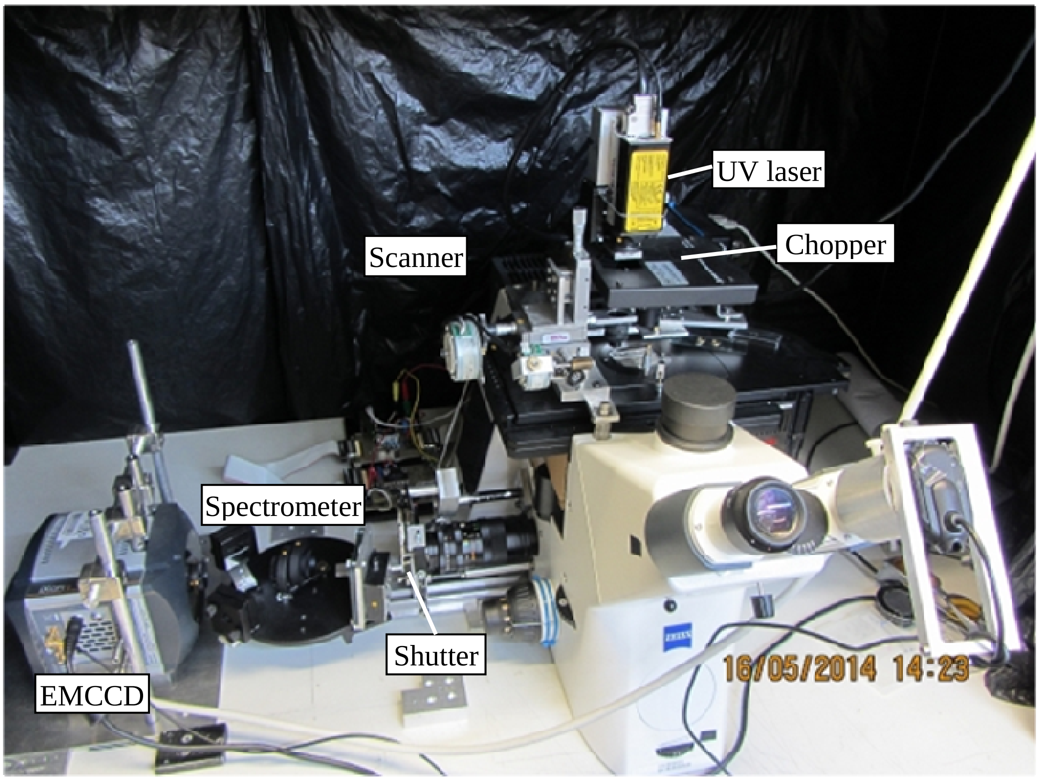
UV laser
Chopper
Scanner
Spectrometer
Shutter
EMCCD
16/05/2014 14:23

Figure 2.13: Our time-gated fluorescent microscope with spectrometer

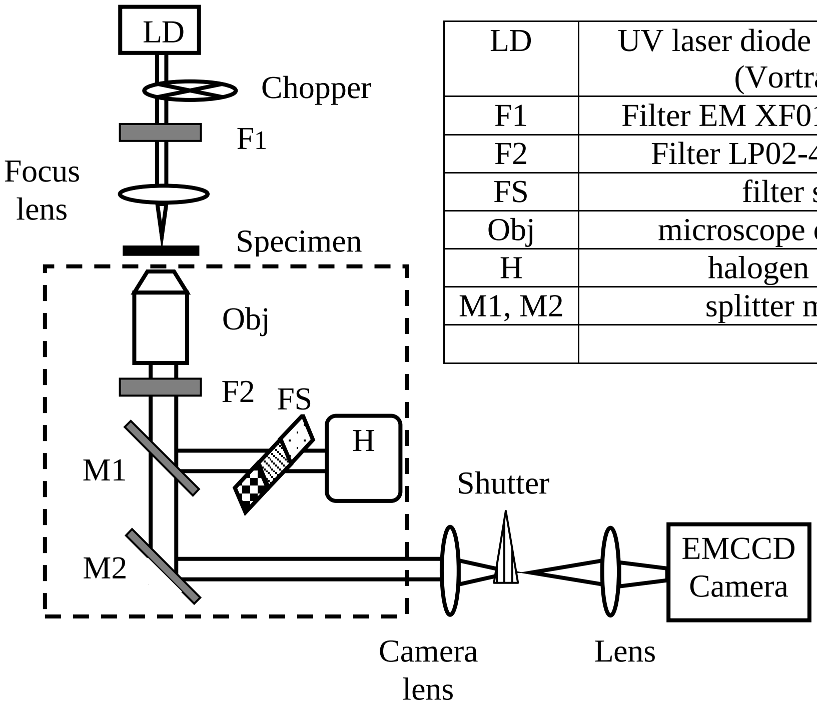

LD	UV laser diode Stradus 375 (Vortran)
F1	Filter EM XF01 330WB60
F2	Filter LP02-442RS-25
FS	filter set
Obj	microscope objective
H	halogen lamp
M1, M2	splitter mirror

Figure 2.14: The scheme of time-gated fluorescent microscope imaging

2.10 “Mosaic” imaging

Absorption of excitation light is low for two reasons: molar absorption is intrinsically low and the samples on the microscope must be thin. Consequently, the fluorescence signal for a single shot of the laser is very small. We have two ways to collect a sufficiently large number of photons per pixel in order to have a good image. The first one is to increase the number of laser shots integrated on one image, or take several images and add them. Noises will also add with the different shots. The second possibility is to increase the laser power, but this solution also has its limits, like cost and availability of the laser, danger for the operator, thermal destruction of the sample (the contrast agent is fortunately very resistant to photobleaching).

However, the optimal laser spot is a lot smaller than a full image of the sample seen by the microscope. We then decided to take images only in the small region illuminated by the laser, scan the laser on the surface of the sample, and assemble the small images by software to form the full sample image. We don’t add the noise of each image in the dark regions.

We purchased a bare-bones microscope with a manual translation stage. It would be difficult to motorize it, but not too complex to move the source above the sample. The accuracy of the steps is not very tight, since it corresponds to the laser’s spot size and since we want to quickly scan the whole sample surface to find the bright regions where the contrast agent is accumulated. The sample does not move on the microscope, then the laser positioning on it is easy to determine. For the 2D scan, we simply used two step motors salvaged from an old ink jet printer.

2.11 System background noise

We measured the background noise of the system when the excitation laser is off (case 1) and when it is turned on without a sample (case 2). The main measurement parameters are listed in the table 2.3. These parameters were those used in all other measurements.

Table 2.3: The measurement parameters

Excitation pulse width (ms)	6.25
EM gain	1000
Vertical shift (μs)	0.9
Read-out rate (MHz)	10
Pre-amplifier	5.1
Operating temperature (^{o}C)	-75
Baseline clamp mode	Selected

The average value given by a pixel in the observation area is 104 for the first case. The background noise for this first case is mostly due to the internal working of the camera: the read-out noise, the clock-induced charge and the thermal noise. In the second case, the average value of a pixel increases a little bit to 109. It may come directly from residual laser light (see section 2.2) scattered by the surrounding equipment, that the chopper does not eliminate. The objectives are made from glass that may emit a long lifetime fluorescent and causes the increase of the background.

The low concentration of Tb^{3+} as low as 20 micro-mole can easily be detected as shown in the figure 2.15. This limit can pushed lower if we increase the integration time, that is if the camera collects emission light of many excitation pulses before the read-out process begins.

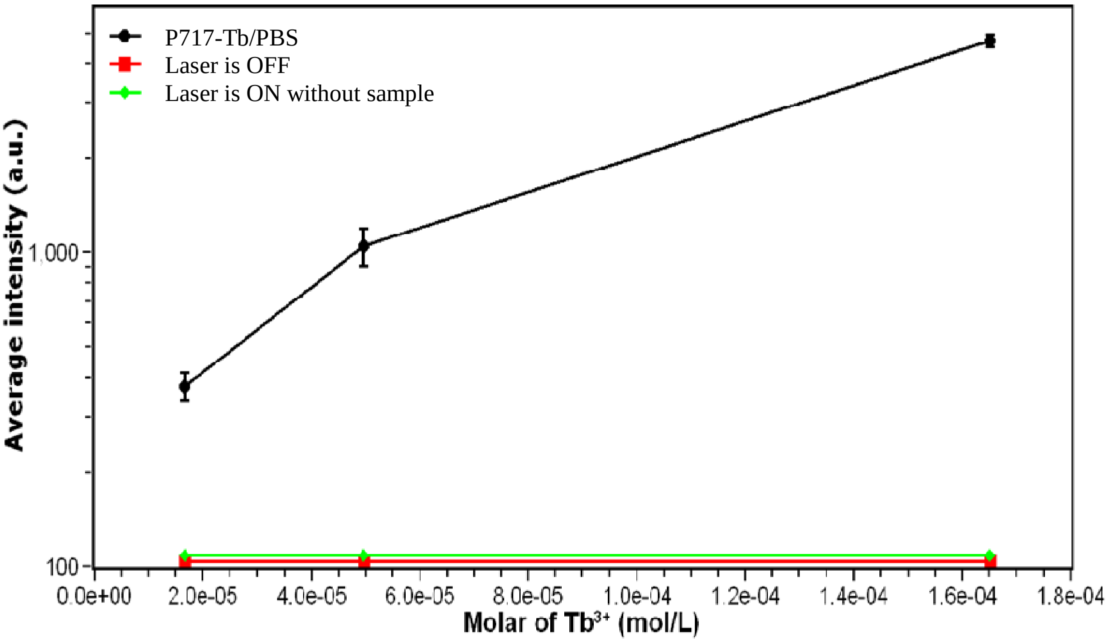

Figure 2.15: The background of the microscope system

2.12 Conclusion

For this thesis, we built the complete system from scratch. On a good inverted microscope, we adapted a simple UV laser source and purchased the best camera we could find. Some elements of this experiment are home-built, like the translation stages and the spectrometer. A time-resolved measurement needs a good synchronization of its different parts, of course, so we developed all of the electronics and software. There is no black box here, any parameter can be measured and modified. Therefore, we are confident in the quality of our results. And, last but not least, the whole system is quite comfortable to use!

Chapter 3

The EMCCD camera

We want to acquire very low fluorescence images; therefore we need a camera with a very good quantum efficiency, low noise and with a controllable gain. Time-resolved fluorescence imposes a precise control of the exposition time. We bought the best camera we could find.

3.1 CCD camera

The Charge-Coupled Device (CCD) is an image sensor, which is widely used in everyday life and in science. It was primarily developed to generate images for television broadcasting and many design details of the CCD sensors show this legacy. An image is a two-dimensional signal whereas a radio wave is a one-dimensional function of time. The television tube was designed to easily display, with very few analog components, the images after demodulation of the radio signal. It is just an electron beam, which scans the image line after line (interleaved but we will ignore this small detail here) and excites a phosphor proportionally to the beam’s intensity. Therefore, a video signal is the succession of the luminance variations of the lines, one after the other, with synchronization between lines and between successive images. The CCD sensor is a solid-state circuit designed to generate a signal suitable for TV transmission. The basic elements of a CCD are columns of p-doped metal-oxide-semiconductor (MOS) capacitors. These capacitors are organized into an array. Each capacitor is a pixel of the image. The individual capacitor has two main functions:

- It convert light to photoelectrons like a photodiode and stores them during the accumulation phase.

- It transfers its charges to the next capacitor, below itself in the column, during the readout phase, where the 2D signal is converted to an 1D one, while receiving the charges from the capacitor above itself.

The way that charges are transferred from a pixel to a neighboring pixel is a main characterization of CCD.

3.1.1 The transfer of charges

Each pixel has two or three electrodes. For the sake of simplicity, we assume in our example that a pixel has three electrodes. All the pixels of all the columns, on a same line, share the same electrodes. During the integration phase of the image, only one of the three electrodes - the one at the center - in each pixel is held at a positive potential. This electrode attracts the photoelectrons and then it accumulates the charges proportionally to the light incident on the cell. The neighboring electrodes, with their lower potentials, act as potential barriers that eliminate the drift of charges to the neighbor pixels. Lateral barriers, permanently defined by doping the semiconductor, separate the column from each others.

During the readout phase, the charges are transferred from pixel to pixel on the columns – it is called the shift. This process is performed by sequentially changing the voltage of electrodes, since the negative charges follow the most positive potential (see figure 3.1):

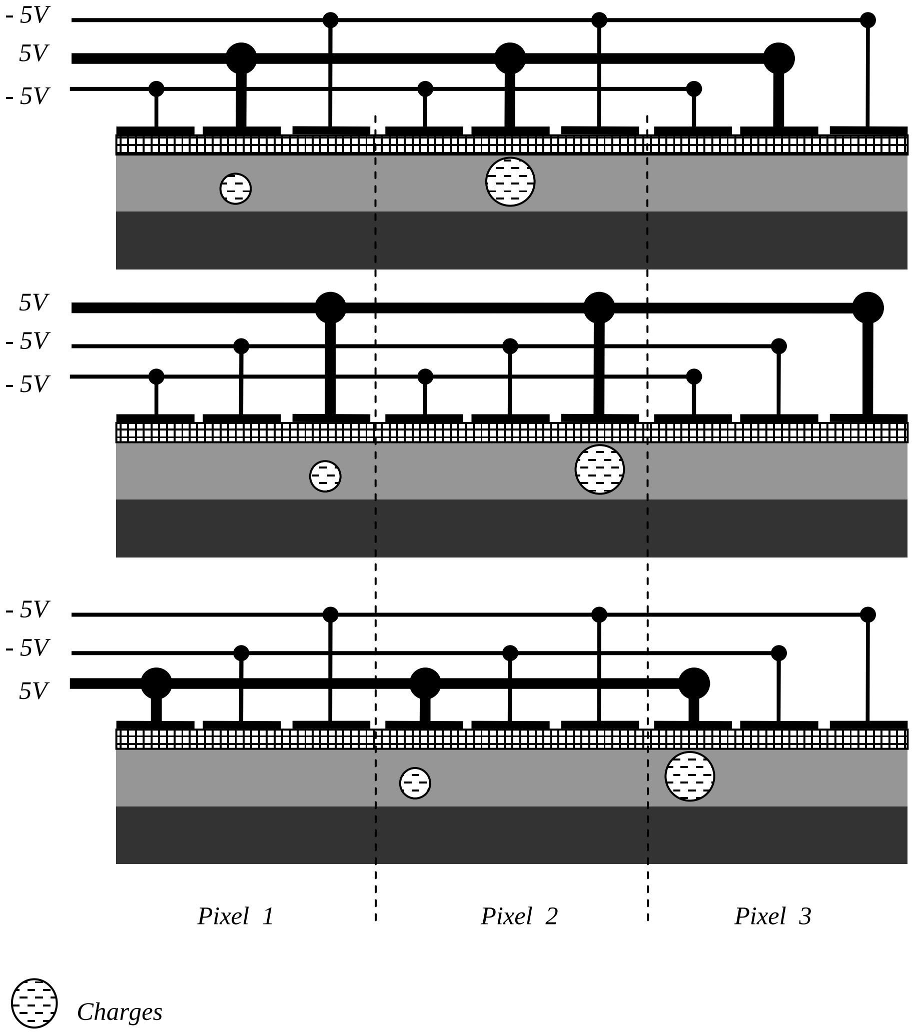

Figure 3.1: The shift of charges in CCD

3.1.2 The CCD cameras architectures

There are three main architectures for CCD cameras.

The Full Frame CCD

Nearly all the sensor area is used to collect photons so this architecture is very sensitive. The accumulated charges in the image area are shifted vertically, all the row simultaneously, by one pixel. Therefore, the bottom line of the image is transferred into the horizontal serial register. Then the horizontal serial register is shifted horizontally to the read-out circuit where each individual pixel is amplified by a common gain and output to the A/D converter (or to the modulator if we want an old-style analog TV signal). The main disadvantage of a full frame sensor is the charge smearing caused by light falling on the sensor whilst the read-out process. To avoid this, a mechanical shutter is used to cover the sensor during the read-out. The shutter is not needed when a pulsed light source is used.

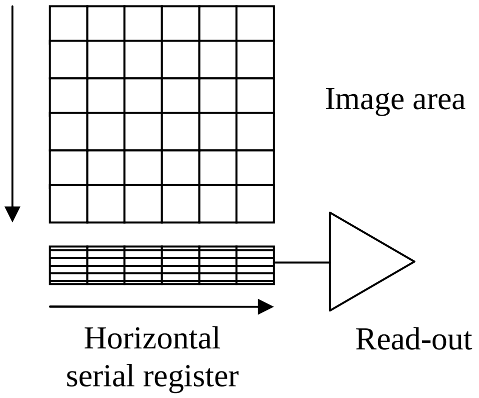

Figure 3.2: The full frame architecture

The frame transfer CCD

A storage area is added between the image area and the horizontal serial register (figure 3.3). The storage area has the same dimension as the image area and is protected from light by a light-tight mask. When the exposure time is over, the accumulated charges in the image area are shifted quickly to the storage area. While the storage array is read, the image area can accumulate charges for the next image. A frame transfer CCD imager can operate continuously without a shutter at a high rate. The sensor circuit is bigger and then more expensive than the full frame sensor since the storage area is approximately as large as the active area. The fill ratio of the active area is very good, nearly 1, like for the full frame sensor.

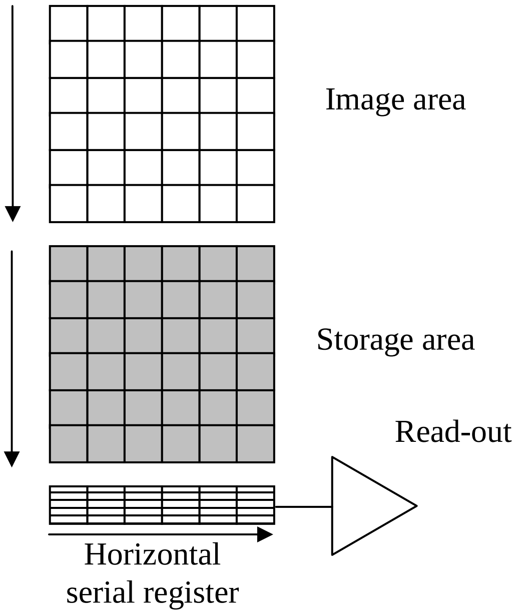

Figure 3.3: The frame transfer architecture

The Interline Transfer CCD

The interline-transfer CCD has charge transfer channels called Interline Masks (the gray area in the figure 3.4). These are immediately adjacent to each photodiode. They play the same role as the storage area of the frame transfer CCD, but since they are very close to the accumulation regions, the accumulated charges can be rapidly shifted into the channels after the exposure time. The very rapid image acquisition virtually eliminates image smear. The disadvantage of interline transfer architecture is the interline mask reduces the light sensitive area of the sensor as is decreases the fill ratio.

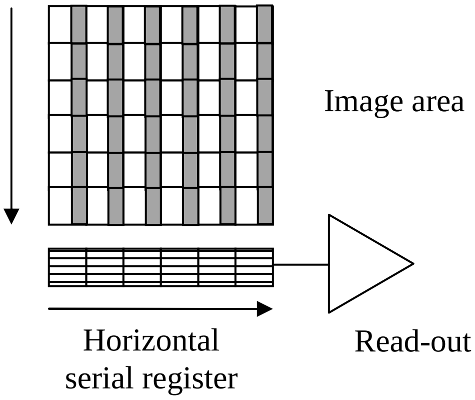

Figure 3.4: The interline-transfer architecture

3.2 Quantification of the signal provided by our camera

Our EMCCD camera is a frame transfer camera, but with the addition of a programmable gain. We now explain how we use it and how we studied the histograms of the data collected from the camera. With these diagrams, we developed a numerical method to calculate the average number of photoelectrons at the input of the multiplying register. Therefore, we can estimate the average number of photons incident on the camera sensor.

3.2.1 Theory

In the EMCDD camera, after the exposure process, the photoelectrons in the image area move quickly to the storage area. Then the charges in the pixels of each row are shifted to the horizontal serial register line by line. This process is similar to the one in an ordinary frame transfer CCD. The difference is that those charges are multiplied by a multiplication register before they reach the readout circuit (figure 3.5).

The multiplication register contains many hundreds of cells that are driven with a sequence of voltage to move the charges to the next element. An avalanche multiplication of the electrons occurs as they are moving through each element of this register. The gain per cell is actually quite small, only around 1.01–1.015. Nevertheless, with a large number of cells, a substantial total mean electron multiplication gain G is achieved. To ensure a good dynamic range and gain stability, among other considerations, the actual gain is normally no bigger than 1000.

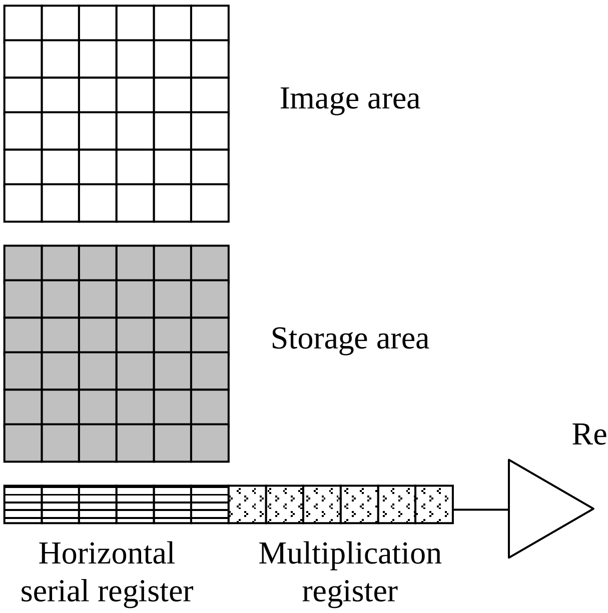

Figure 3.5: EMCCD architecture

Due to the stochastic nature of the multiplication process, each photoelectron, which passes through the multiplication register, has different gains from the other photoelectrons. As a result, a large range in the number of output charges could be produced from each possible number of input photoelectrons n. The distribution of output charges m can be approximated by the formula 3.1 [66]

$$\begin{aligned} T_n(m) &= \frac{m^{n-1}\exp\left(\frac{-m}{G}\right)}{G^n(n-1)!} && n>0 \\ &= \delta_0^m && n=0 \end{aligned} \qquad (3.1)$$

where δ_0^m is the Kronecker delta

If the Analog to Digital Conversion (ADC) process is perfectly linear, each small set of m values will correspond to a digital value k, and we could rewrite the formula 3.1 to

$$\begin{aligned} f_n(k) &= \frac{k^{n-1}\exp\left(\frac{-k}{g}\right)}{g^n(n-1)!} && n>0 \\ &= \delta_0^k && n=0 \end{aligned} \qquad (3.2)$$

$f_n(k)$ is the histogram that corresponds only to n photoelectrons entering the electron multiplying register, and g is a constant number. In other word, the probability to obtain the value k at the output of ADC is $f_n(k)$ for n input photoelectrons.

In the fact, the ADC process is not perfect. When there are no input charges, we have the Gaussian-shape histogram

$$F_0(k) = A\exp\left(-\frac{(k-k_c)^2}{2\sigma^2}\right) \tag{3.3}$$

Therefore, if there are only *n* photoelectrons entering the electron multiplying register, the histogram will be the convolution of $f_n(\underline{k})$ and $F_0(k)$

$$F_n(k) = F_0(k) * f_n(k) \tag{3.4}$$

Some functions $F_n(k)$ are plotted on figure 3.6. However, the function $F_n(k)$ is not a real histogram that we can measure. In reality, the incoming photoelectrons number obeys a Poissonnian distribution:

$$P(n,\lambda) = \frac{\lambda^n e^{-\lambda}}{n!} \tag{3.5}$$

where *n* is the number of photoelectrons and where λ is its average. Therefore, the formula, which corresponds to the observed histogram, is

$$F_\lambda(k) = \sum_{n=0}^{N} F_n(k) P(n,\lambda) \tag{3.6}$$

Formula (3.6) presents a real histogram we have when the average number of input photoelectron is λ (see figure 3.7). Therefore, if we have histograms of the camera, we can have a quantitative estimation for the average number of incoming photoelectrons.

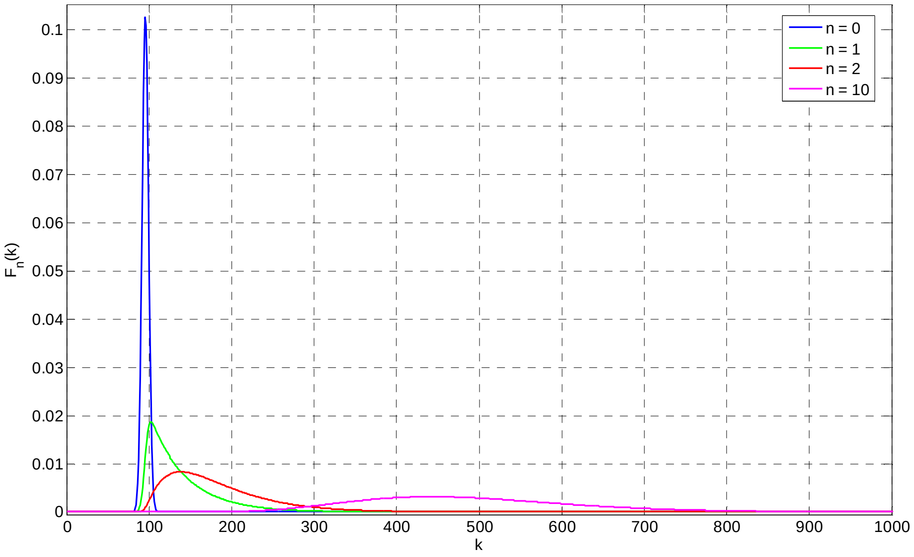

Figure 3.6: The functional forms of $F_0(k)$, $F_1(k)$, $F_2(k)$, $F_{10}(k)$

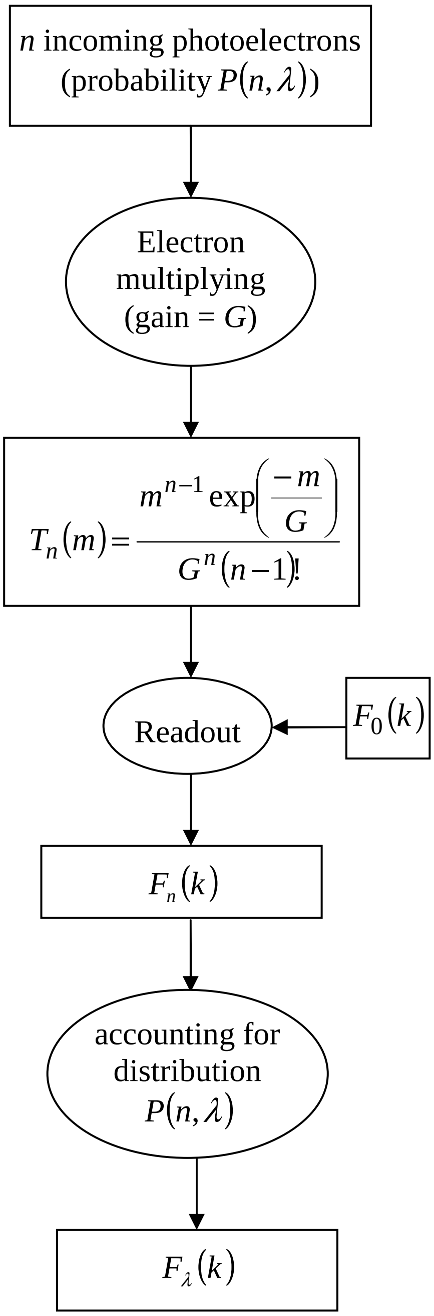
n incoming photoelectrons (probability $P(n,\lambda)$)
Electron multiplying (gain = G)
$T_n(m)=\dfrac{m^{n-1}\exp\left(\dfrac{-m}{G}\right)}{G^n(n-1)!}$
Readout
$F_0(k)$
$F_n(k)$
accounting for distribution $P(n,\lambda)$
$F_\lambda(k)$

Figure 3.7: How to get the histogram of the photoelectrons

3.2.2 The function $F_0(k)$ and exponential constant g

In order to apply the theory we described in the section 3.2.1; we must know the function $F_0(k)$ and the constant *g*.

The function $F_0(k)$ is the histogram we will have when the shutter of the camera is closed. It is very easy to get. The histogram data is fitted to the Gaussian function (3.3) to estimate the values of k_c and σ.

Evaluating the parameter *g* is a little more complicated. In fact, we cannot get the histogram corresponding to the function $f_1(k)$. If we consider a very low intensity light incident on the camera during one exposure duration, with $\lambda << 1$, either one photoelectron or zero photoelectron would be generated in each pixel, and from formula (3.5) and (3.6) the measured histogram should be approximated by

$$F_\lambda(k) = F_0(k)P(0,\lambda) + F_1(k)P(1,\lambda) = e^{-\lambda}F_0(k) + \lambda e^{-\lambda}F_1(k) \tag{3.7}$$

with

$$F_1(k) = F_0(k) * f_1(k) \tag{3.8}$$

In the expression (3.7), the distribution $F_0(k)$ peaks around $k \sim k_c$, and can be neglected outside this region (see figure 3.6). In the same way, the convolution by $F_0(k)$ in (3.8) will have its primarily influence in this region $k \sim k_c$, where there is a jump of the distribution $f_1(k)$. Outside this region, this distribution $F_0(k)$ is really narrow compared to the behavior of $f_1(k)$ and will act as a Dirac delta function, leading to $F_1(k) \sim f_1(k)$ and to

$$F_\lambda(k) \propto \exp\left(-\frac{k}{g}\right) \tag{3.9}$$

Therefore, we fitted, for $\lambda \ll 1$, the part of the histogram with an exponential behavior, outside the zone $k \sim k_c$, and then we estimate the value of g.

3.2.3 Numerical method to estimate average number of photoelectrons λ at input

It is not easy to find the analytic form of $F_\lambda(k)$, so in order to estimate the value of λ from the histogram of camera, we used a numerical method.

3.2.3.1 R^2

In statistics, the coefficient R^2 measures how successful is the fit in explaining the variations of the data. R^2 can take any value in the range from 0 to 1; a value near 1 indicates that the model accounts for a greater proportion of variance. R^2 is defined as [67]

$$R^2 = 1 - \frac{SSE}{SST} \tag{3.10}$$

where *SST* is called total sum of squares and is defined by the formula

$$SST = \sum_i (y_i - \bar{y})^2 \tag{3.11}$$

and where *SSE* is called sum of squares due to errors and is defined by

$$SSE = \sum_i (y_i - f_i)^2 \tag{3.12}$$

Here y_i is the observed data, $\bar{y}$ is the average value of y_i and f_i is the predicted value from the fitting function. The minimum value of quotient $\frac{SSE}{SST}$ corresponds to the best fit.

3.2.3.2 Numerical method

In summary, we propose to implement the following protocol: a part of the camera sensor is uniformly illuminated, and we collect the histogram of the values from the different pixels in the region of interest. We then fit the histogram using the theoretical model we just have previously presented. The data y_i in (3.11) and (3.12) therefore corresponds to the number of pixels with a value i.

The figure 3.8 shows an example of the dependence of quotient $\frac{SSE}{SST}$ on the average number of photoelectrons λ. It is easy to see that there is only one minimum value of the quotient. The algorithm we used to estimate the value of λ is presented in the figure 2.6

Step 1: 5 values λ_j in a given range [$\lambda_{\min}$, $\lambda_{\max}$] are selected.

Step 2: $\frac{SSE}{SST}(\lambda_j)$ of each value of λ_j is calculated.

Step 3: find out the index $j\min$ for the smallest value of $\frac{SSE}{SST}(\lambda_{j\min})$.

Step 4: The range of λ will be changed: $\lambda_{\min} = \lambda_{j\min-1}$, $\lambda_{\max} = \lambda_{j\min-1}$ (figure 3.8) and return Step 1 until the evolution of $\frac{SSE}{SST}(\lambda_{j\min})$ is smaller than a given error value.

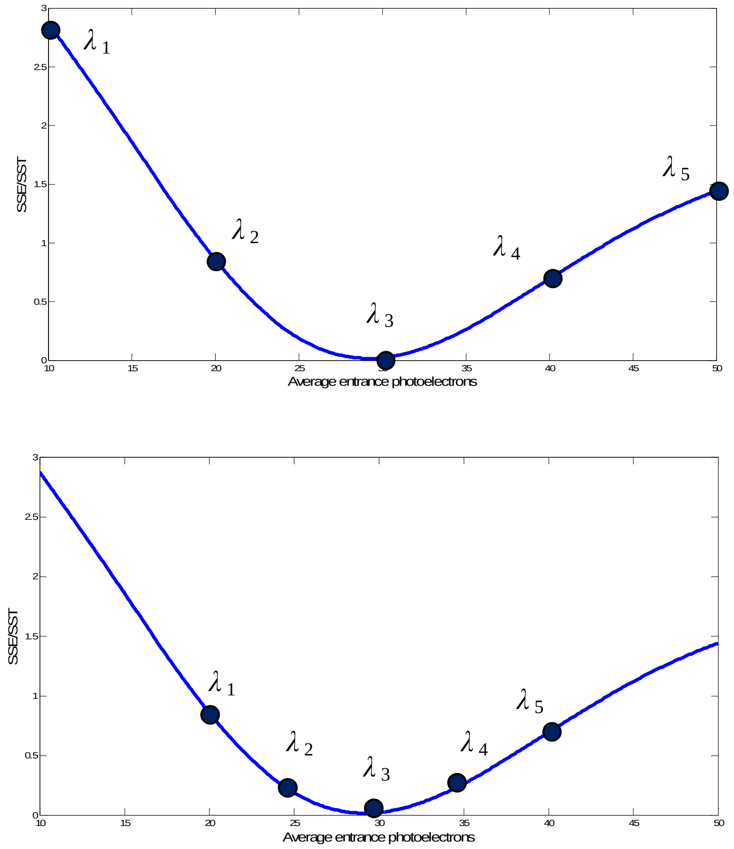

Figure 3.8: Selection of the value of λ_j in our algorithm

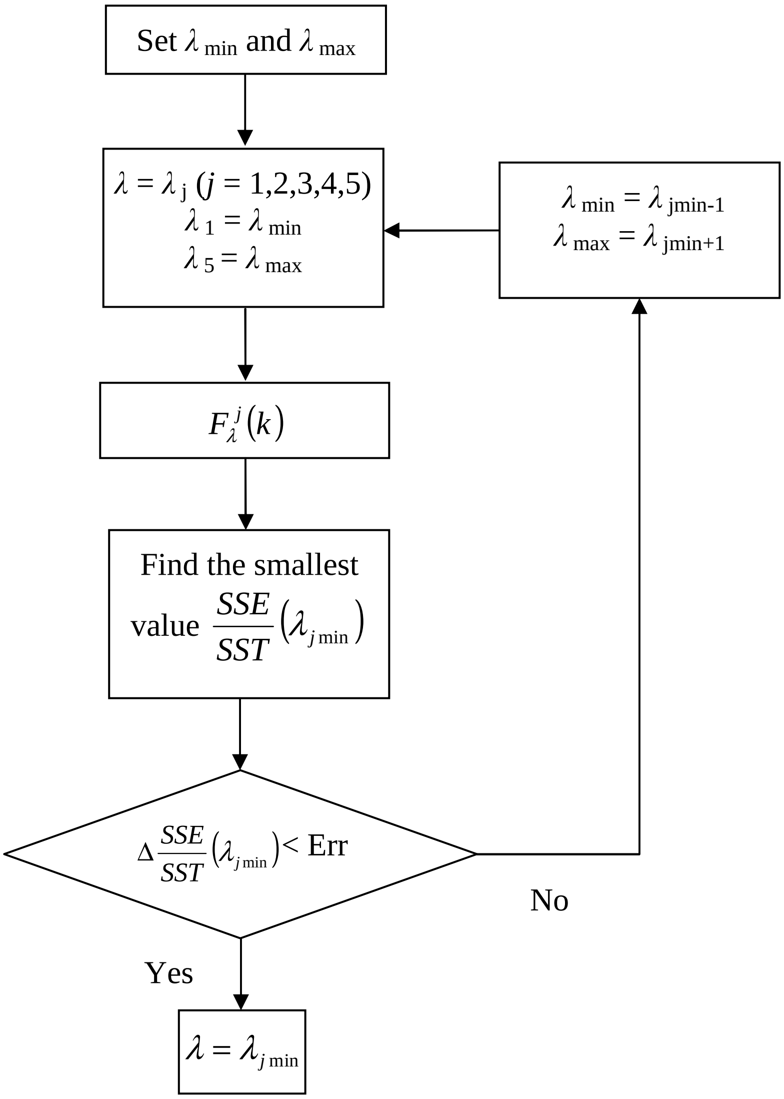
Set $\lambda_{\min}$ and $\lambda_{\max}$
$\lambda = \lambda_j$ (j = 1,2,3,4,5)
$\lambda_1 = \lambda_{\min}$
$\lambda_5 = \lambda_{\max}$
$\lambda_{\min} = \lambda_{j\min-1}$
$\lambda_{\max} = \lambda_{j\min+1}$
$F_\lambda^j(k)$
Find the smallest value $\frac{SSE}{SST}(\lambda_{j\min})$
$\Delta\frac{SSE}{SST}(\lambda_{j\min})$< Err
No
Yes
$\lambda = \lambda_{j\min}$

Figure 3.9: The flowchart of the algorithm

3.2.4 An example

This model was applied on the EMCCD camera Andor iXon3 DU-897D. Table 3.1 shows the parameters of camera we used in the experiment.

Table 3.1: Parameters of the camera

Electron multiplying gain	1000
Pre-amplifier	5.1
Exposure time	0.04 s
Read-out rate	10 MHz
Vertical shift	0.9 μs
Triggering	External
Operating temperature	-72 ^{o}C

We recorded the histograms with and without the Baseline Clamp option. The baseline (or bias level) is an electronic offset added to the output signal from the EMCCD sensor to ensure that the signal level is always higher than the zero level.

In the fact, small changes in heat generation of the driving electronics within the detector head when acquiring data may cause some drift of the baseline level. Baseline Clamp option is used to correct any drift in the baseline level. Baseline Clamp corrects each individual image for any baseline drift by subtracting an average bias signal from each image pixel and then adding a fixed value to ensure that the displayed signal level is always a positive number of counts. As a result, the baseline remains at a stable value [68].

The experimental setup is shown on figure 3.11: the red light from a He-Ne laser is scattered many times in an integrating sphere. The integrating sphere is designed to provide a uniform distribution at its output port (figure 3.10). Using a beamsplitter, we controlled the laser's power, measured by a powermeter "Fieldmaster" made by Coherent. We used an attenuator to choose the laser light intensity. We recorded this intensity for different attenuation values and the corresponding histograms recorded from the camera.

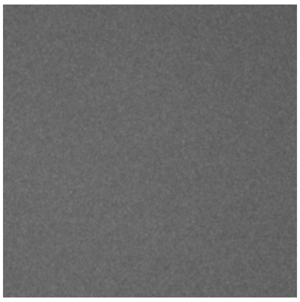

Figure 3.10: Distribution of light at the output of the integrating sphere

It is really flat, as we should expect

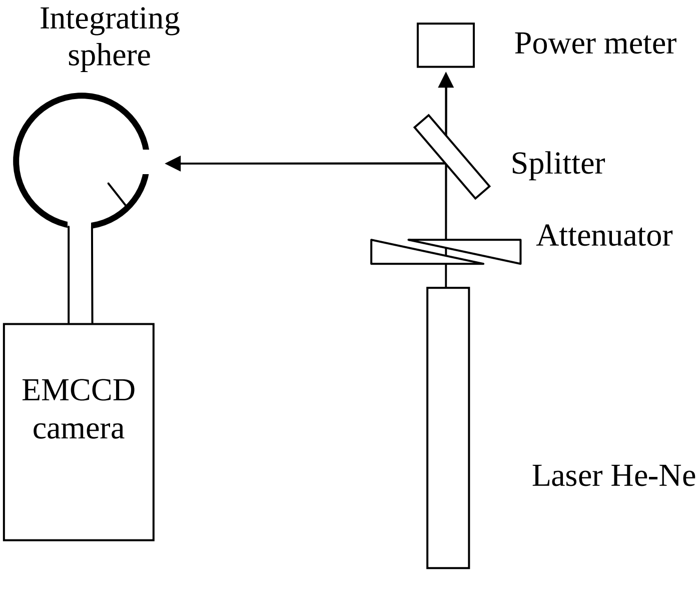

Figure 3.11: The principle of the experimental setup for histogram acquisitions

3.2.4.1 Histograms and fitting curves

The histograms and the corresponding fitting curves at different laser intensities are presented in the table 3.3. The average numbers of photoelectrons and the coefficients R^2 are shown in the table 3.2.

Table 3.2: average number of photoelectrons

laser intensity (μW)	“Baseline Clamp” is off		“Baseline Clamp” is on	
	λ	R^2	λ	R^2
0.005	0.44	*0.499*	0.16	*0.998*
0.013	0.50	*0.544*	0.25	*0.998*
0.050	0.88	*0.647*	0.69	*0.990*
0.099	1.32	*0.816*	1.24	*0.971*
0.157	1.90	*0.874*	1.85	*0.960*
0.311	3.14	*0.965*	3.13	*0.980*
0.418	3.96	*0.984*	3.98	*0.992*
1.020	9.51	*0.990*	9.50	*0.997*
4.040	39.1	*0.976*	38.5	*0.984*
7.000	66.3	*0.964*	66.1	*0.974*
10.00	95.2	*0.956*	94.9	*0.965*
13.20	124	*0.951*	124	*0.955*
16.10	149	*0.942*	149	*0.954*
19.10	175	*0.943*	175	*0.950*
22.30	202	*0.929*	202	*0.934*
25.10	226	*0.919*	226	*0.936*
28.10	251	*0.925*	251	*0.939*
31.30	277	*0.925*	276	*0.933*
34.00	290	*0.927*	290	*0.967*
37.30	309	*0.991*	308	*0.987*
40.10	326	*0.999*	325	*0.999*
43.20	344	*0.999*	343	*1*
46.20	360	*0.999*	359	*1*
49.20	374	*1*	373	*1*
52.10	389	*1*	388	*1*
55.20	404	*1*	398	*1*
58.10	417	*1*	407	*1*
63.10	443	*1*	441	*1*

We can see that, when the “68” option is off, the histograms and fitting lines do not match well at low laser intensity (0.005 and 0.05 μW) and that we have better fits at higher laser intensity. This is reflected in the R^2 coefficients. When “68” option is on, we have good fits for any value of the laser intensity. Obviously, the drift of the baseline level has a strong influence on the histograms when very low light is incident on the CCD sensor. The fitting results show very good performance of the “68” option.

Table 3.3: Histograms and fitting curves at different laser intensities

Laser power (µW)	**“Baseline Clamp” is off**	**“Baseline Clamp” is on**
0.005	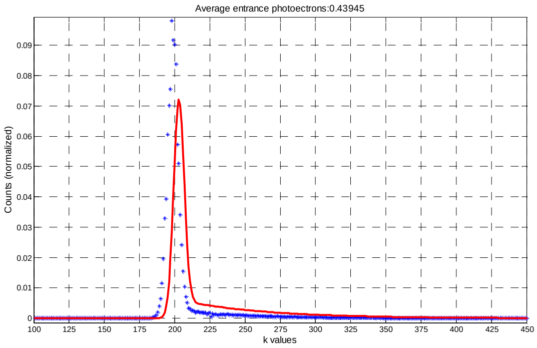	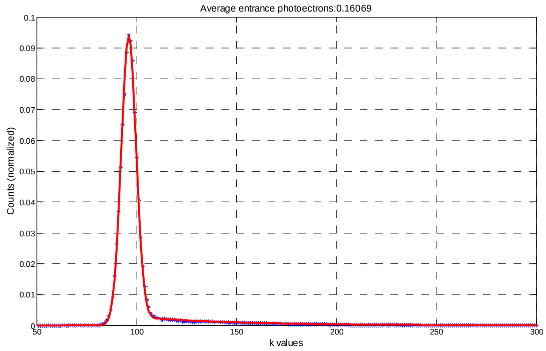
0.050	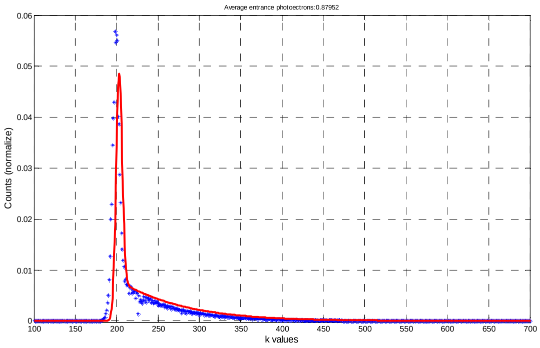	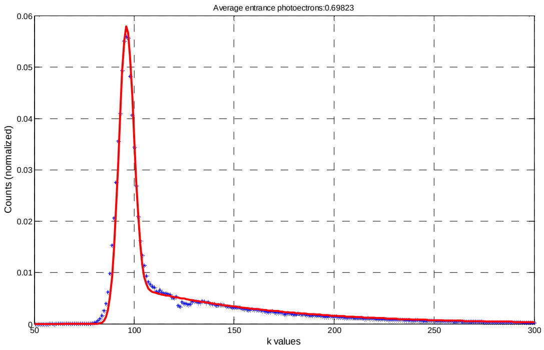
0.157	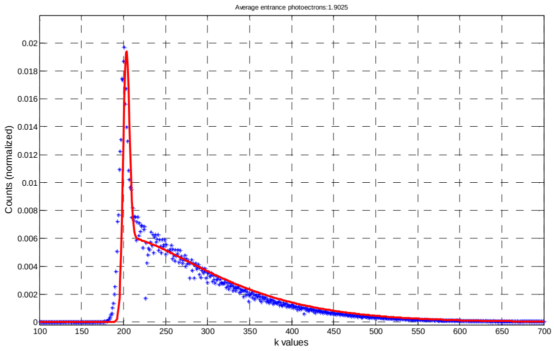	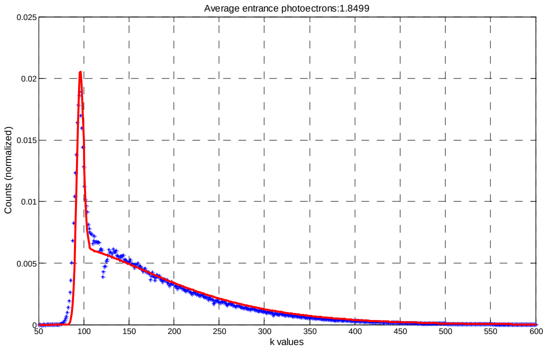
0.311	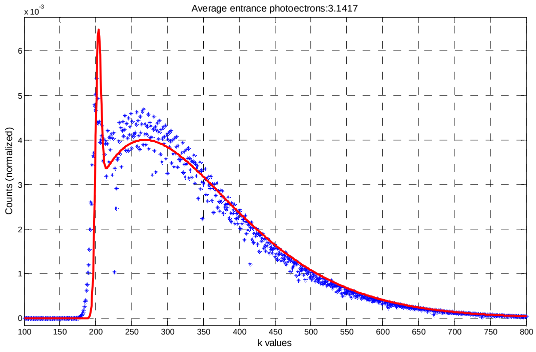	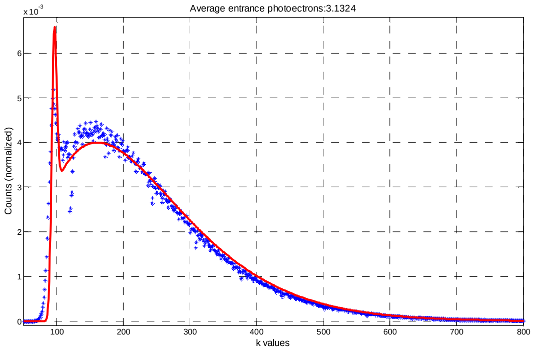

0.418	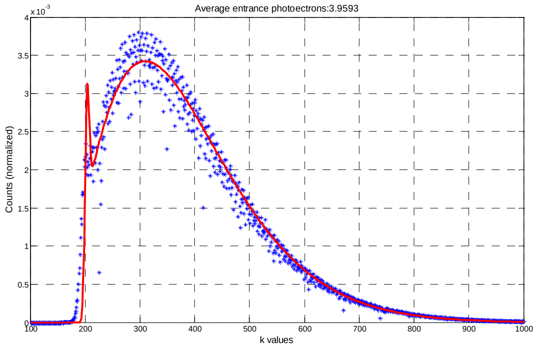	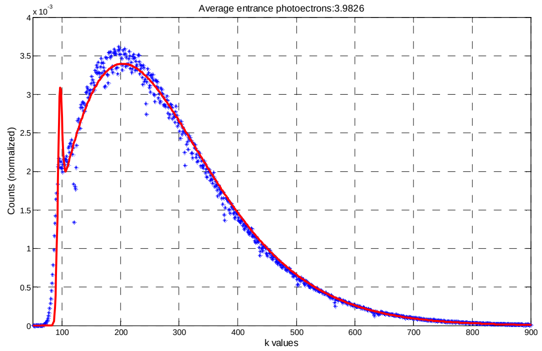
1.020	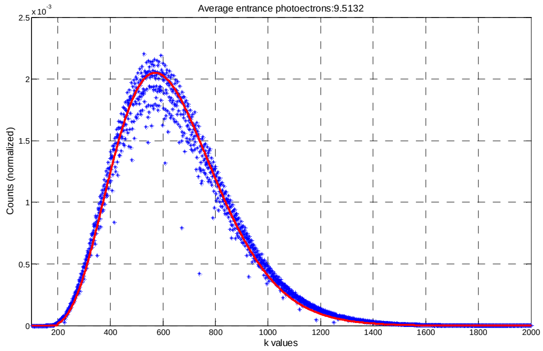	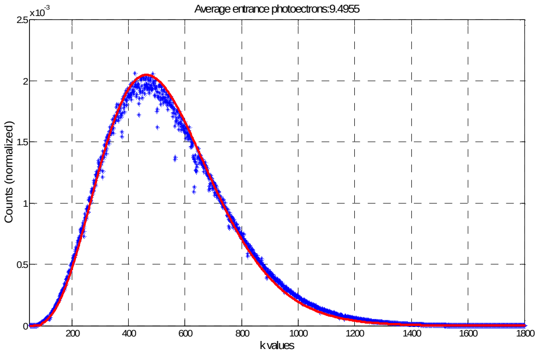
16.10	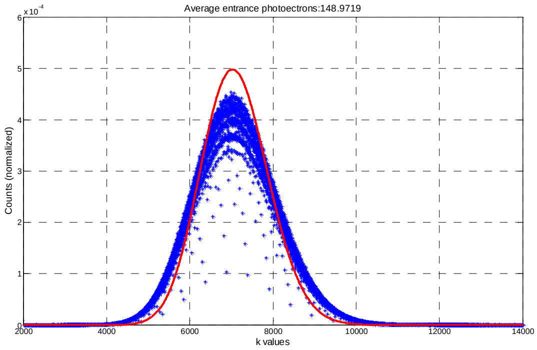	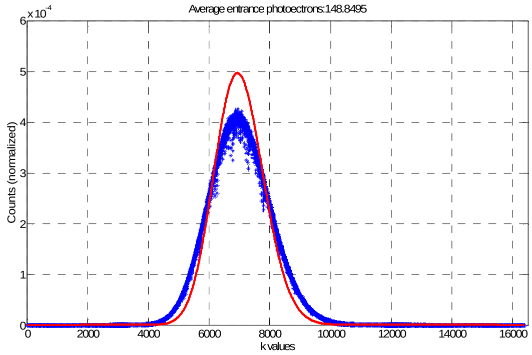
28.10	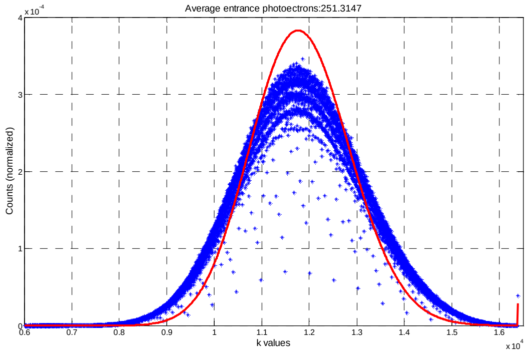	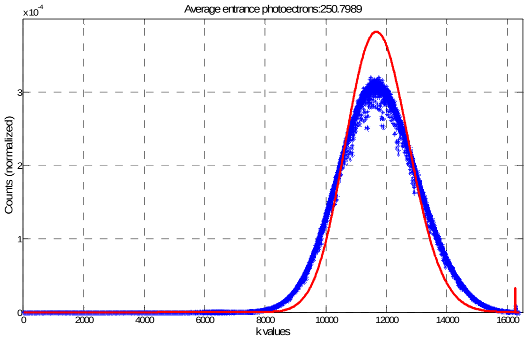

31.30	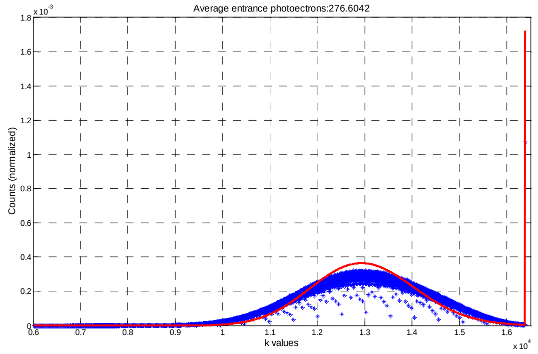	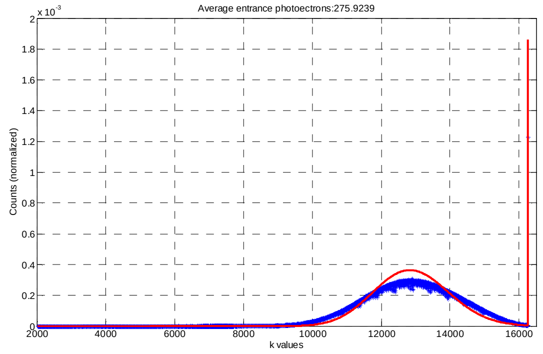
34.0	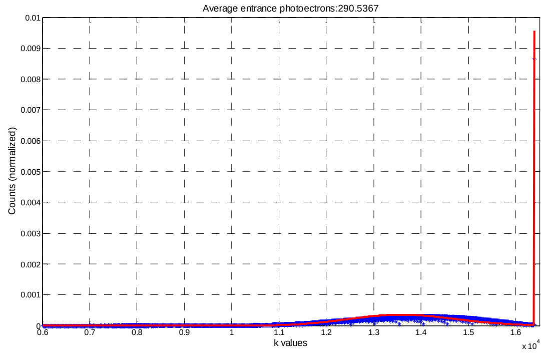	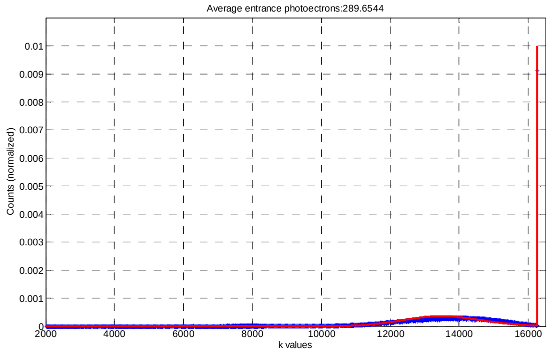
40.10	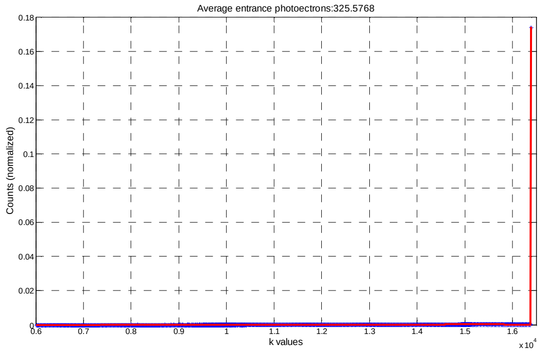	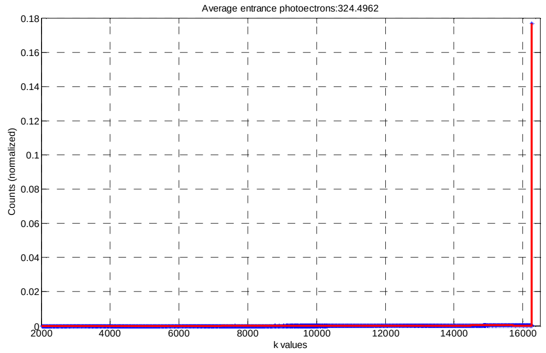

We present an interesting result in figure 3.12. The circle dots show the values of incoming photoelectrons as estimated by the computer program from the histograms. The squared dots show the average value of all pixels in the illuminated area. *The result shows that this method increased the dynamic range of the camera and opens the possibility of distinguish the saturated pixels*.

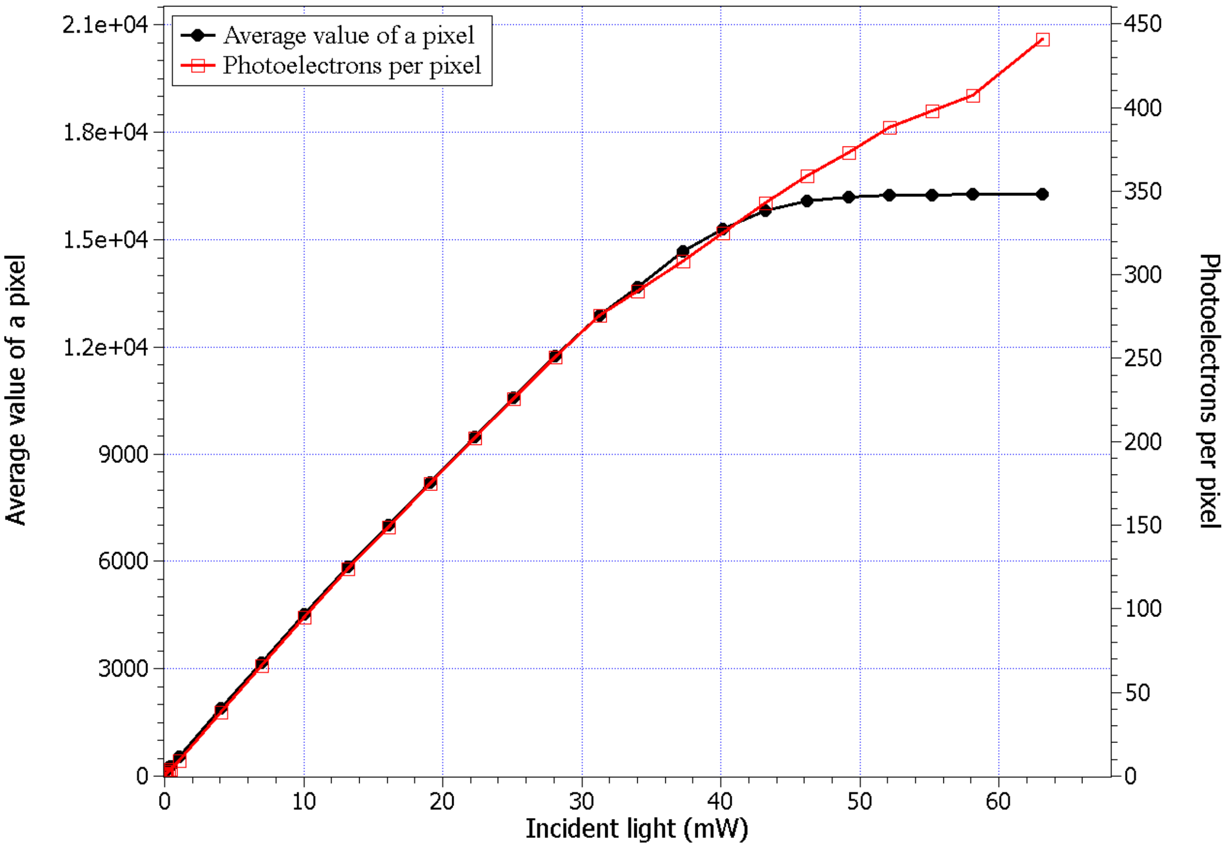

Figure 3.12: dependence of the average value of photoelectrons in a pixel on the incident light when the Baseline Clamp option is selected

The figure 3.12 shows that a linear relationship exists between the average value of a pixel's illumination and the quantity of photoelectrons generated by the pixel in the range from 100 to 13500. We fit this result to the function y = a +b*x by the use of the SciDAVis software with

$a = -2.0 \pm 0.010$

$b = 0.02153 \pm 3.1 \times 10^{-5}$

$R^2 = 0.99996$

This means that, if we know the average value produced by a pixel, we can calculate the number of photoelectrons from this pixel (figure 3.13). Therefore, the average number of photons incident on the pixel can be estimated if the quantum efficiency of camera is known. One can note that the values of *a* and *b* are dependent on many parameters, namely the electron multiplying gain, the operating temperature, the pre-amplifier gain, the read-out rate, the vertical shift.

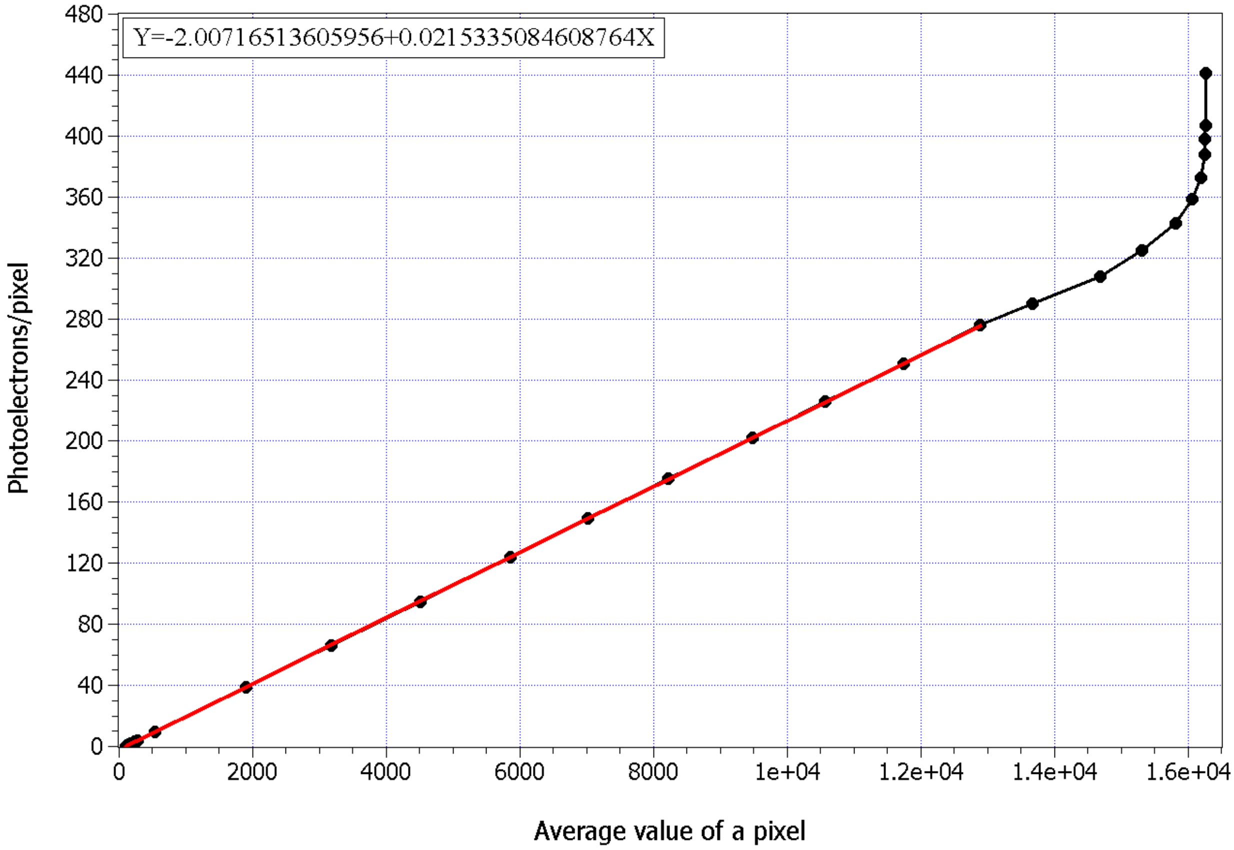

Figure 3.13: Dependence of the number of photoelectrons on the average value given by a pixel when we select the Baseline Clamp option

3.3 Use of the Camera for Long Decay Fluorescent Measurement

We now describes how we can use the EMCCD camera to directly measure long fluorescent lifetimes in the range some hundreds microsecond to some millisecond.

This EMCCD camera have two major acquisition modes: Frame transfer mode (FT) and Non frame transfer mode (NFT). We now briefly details the pertinent parameters for each mode.

Frame Transfer Mode

In Frame Transfer acquisition mode, the iXon3 EMCCD camera can deliver its fastest performance while maintaining an optimal signal to noise ratio. It achieves this through simultaneously acquiring an image onto the image area while reading out the previous image from the masked frame storage area. Thus, there is no time wasted during the readout and the camera operates with what is named as a 100% ‘duty cycle’.

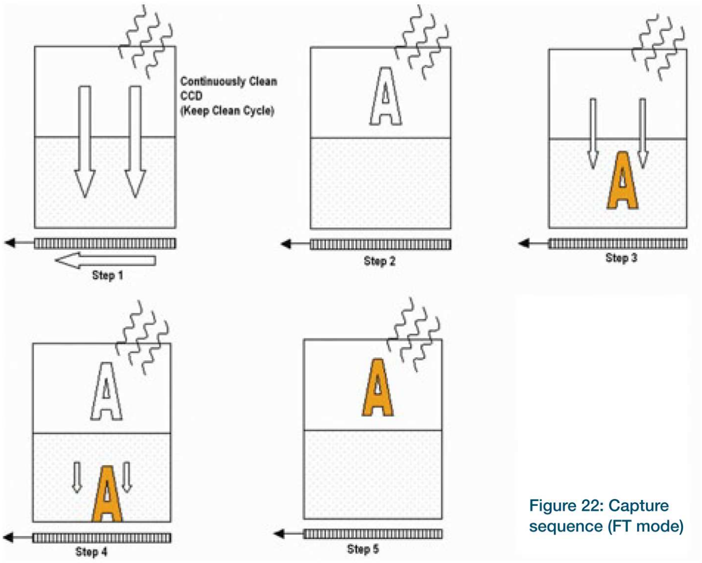

Figure 3.14: Image capture sequence in frame transfer mode

The capture sequence in FT mode follows in 5 steps:

Step 1: both image and storage areas of the CCD are fully cleaned out by process called "Keep clean cycle". When in standby, "Keep clean cycle" occurs continuously to ensure that the camera is always ready to start an acquisition when required.

Step 2: When the camera receives a start acquisition command the camera stops the "Keep clean cycle". This allows the image (photoelectric charge) to build up in the image area of the CCD. The CCD remains in this state until the exposure time has elapsed, at which point the read-out process starts.

Step 3: the first phase of the readout process is to quickly shift the charge, built up in the image area, into the storage area. The time required to move the charge into the Storage area is approximately calculated as follows:

Time = Number of rows in the Image area x Vertical shift rate

Step 4: once the image area has been shifted into the storage area, the image area stops vertically shifting and begins to accumulate charge again, i.e. the next exposure starts. While the image area is accumulating charge the storage area is being read out. This readout phase can take tens of milliseconds to seconds depending on the image size, readout pattern and readout speed.

Step 5: When the readout is completed, the system will wait until the exposure time has elapsed before starting the next read-out (i.e. returning to Step 3).

Non-Frame Transfer Mode

The camera can also operate as an FT CCD in a Non-Frame Transfer (NFT) mode. In this mode of operation, an FT CCD acts much like a standard CCD. The capture sequence for this mode is illustrated here:

The capture sequence in NFT mode follows in 5 steps.

Steps from one to four are the same in the FT mode. In the step 5, the CCD will remain in the "Keep clean cycle" until the end of the accumulation or kinetic cycle time, depending on the acquisition mode, i.e. back to Step 1. At least one "Keep clean cycle" is performed between each exposure. The minimum exposure time is no longer constrained by the time needed to read out the image.

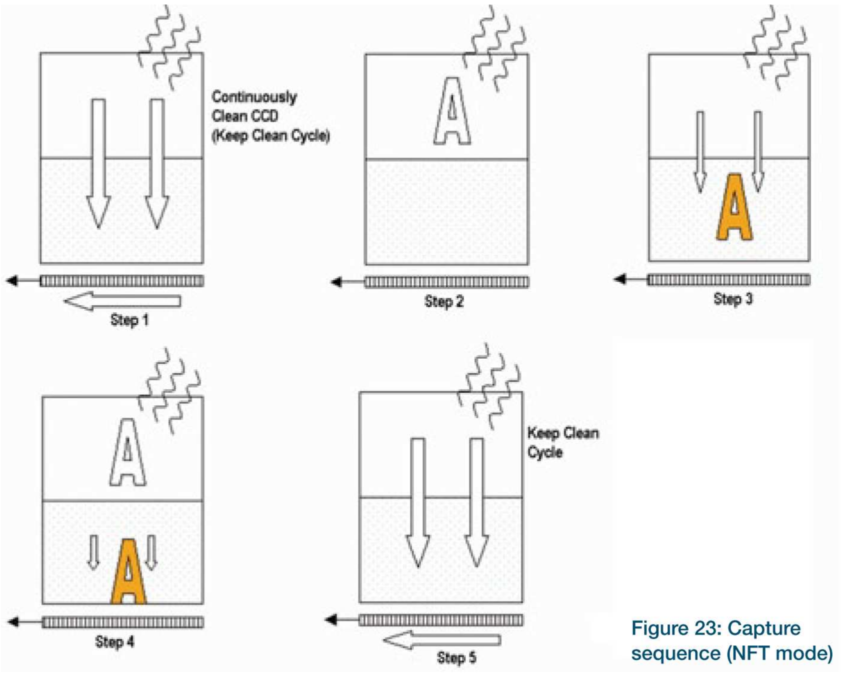
Continuously
Clean CCD
(Keep Clean Cycle)
A
Step 1
Step 2
Step 3
Step 4
Keep Clean
Cycle
Step 5
Figure 23: Capture
sequence (NFT mode)

Figure 3.15: Image capture sequence in non-frame transfer mode

3.3.1 Effect of vertical shift speed on the streaking of image

The vertical shift speed is the time taken to vertically shift all pixels one row down, with the bottom row entering the shift register.

Faster vertical shift speeds also have benefits such as lower Clock Induced Charge (CIC). A drawback with faster vertical shift speeds is that the charge transfer efficiency is reduced, effectively reducing the pixel well depth – the maximum number of electrons in a single pixel. This is particularly important for bright signals as a pixel with a large signal is likely to have some charge left behind if the vertical shift speed is too fast. This will result in degraded spatial resolution.

In the time-gated fluorescent microscope, if there is a good synchronization between chopper, laser and EMCCD camera (figure 3.17), the streaking effect doesn't happen (figure 3.16).

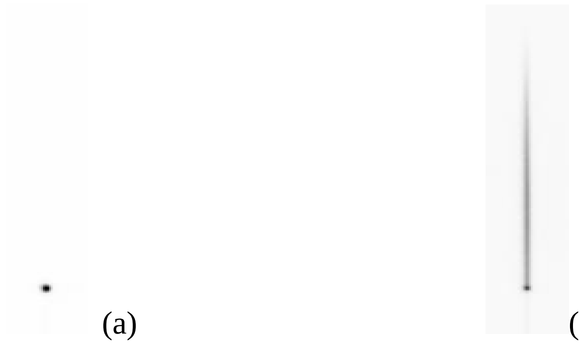

(a) (b)

Figure 3.16: The correct image (a) and the wrong image (b) due to the streaking (the color is inverted)

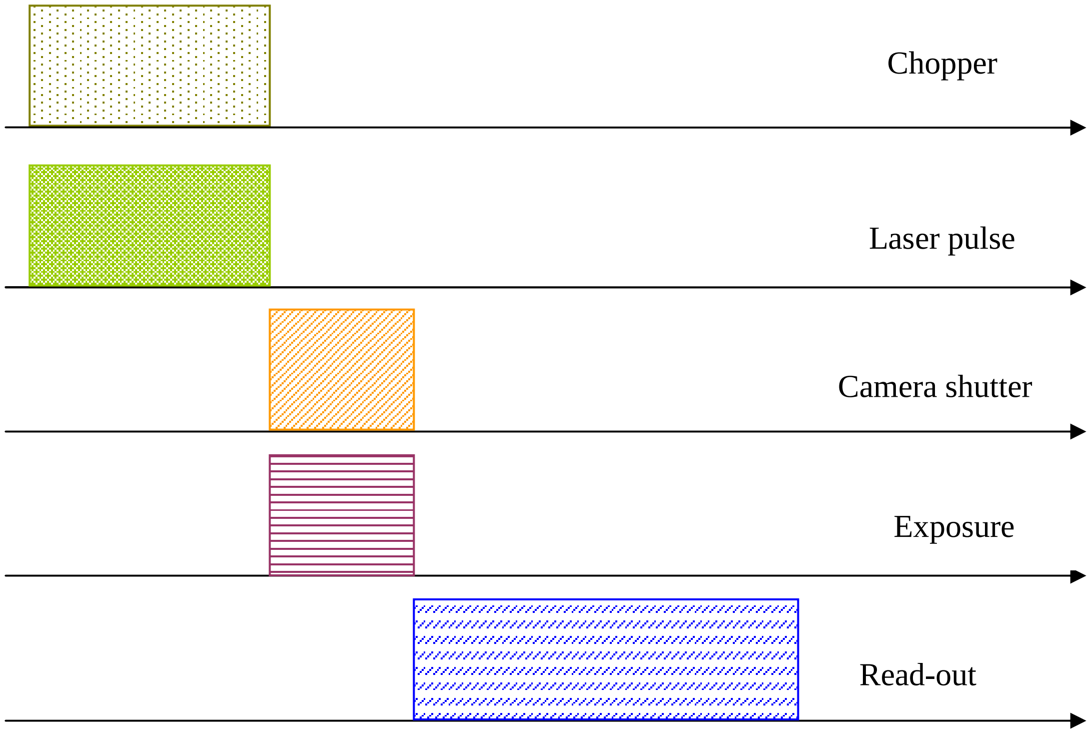

Figure 3.17: Time synchronization in the system

There are two cases to cause the streaking in the EMCCD Andor iXon3 camera.

The case 1: The exposure process begins later than the opening of the camera's shutter, with a delay of duration T1 (figure 3.18).

We consider one column of vertical pixel. On this column, only one pixel on the row 100th is illuminated by a exponential decay light. In the non frame transfer mode of EMCCD camera, when the exposure process has not yet begun, the keep clean cycle process is running. Every rows move down at vertical shift speed V_s.

In the figure 3.19, the illuminated pixel collected 100 photon-induced charges at the time camera shutter was opened.

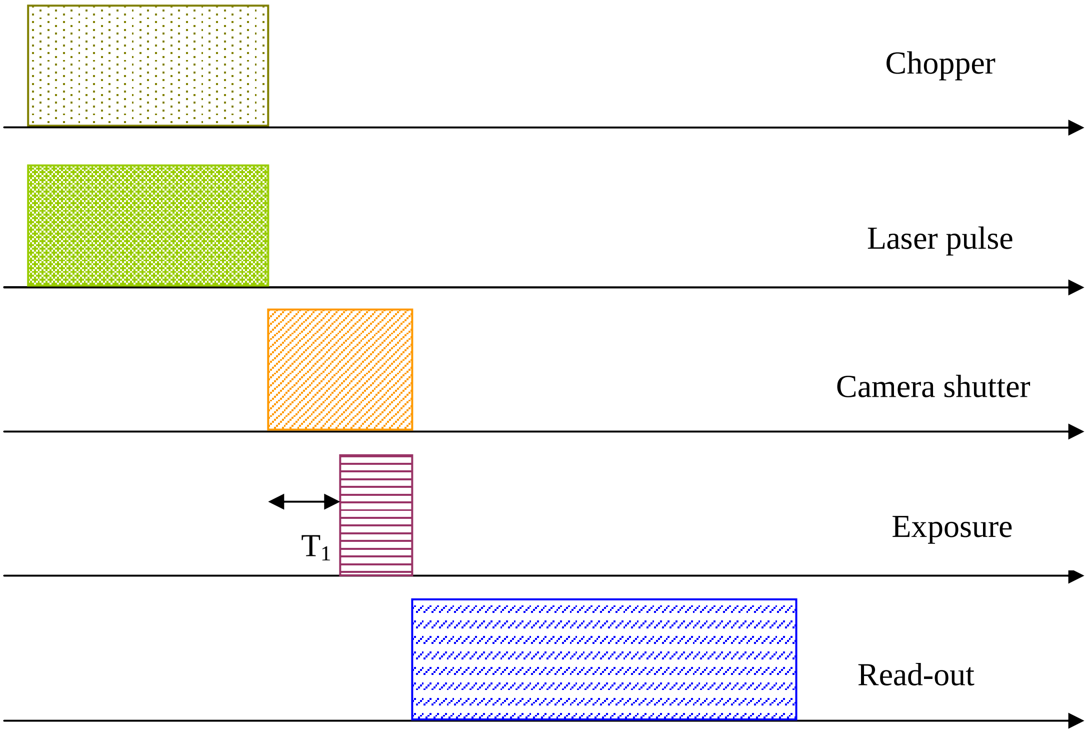

Figure 3.18: The exposure process begins late

In the first vertical shift, the 100 charges of illuminated pixel move down to next pixel – pixel 101th. Because the illuminated pixel is exposure by an exponential decay light, a smaller charges – 90 – is collected.

In the second vertical shift, total charges in the pixels 101th and 100th are down respectively to pixels 102th and 101th. After that, the illuminated pixel collects 82 charges.

This process is continued until the exposure process begins. At this time, we assume that five vertical shifts are taken and the numbers of photoelectrons in the pixel 100th to 105th are a function of the decay rate of light.

When exposed, during the exposure duration window, more charges are collected by pixel 100th. We can use the number of charges in the pixels 101th to 105th to estimate the decay constant.

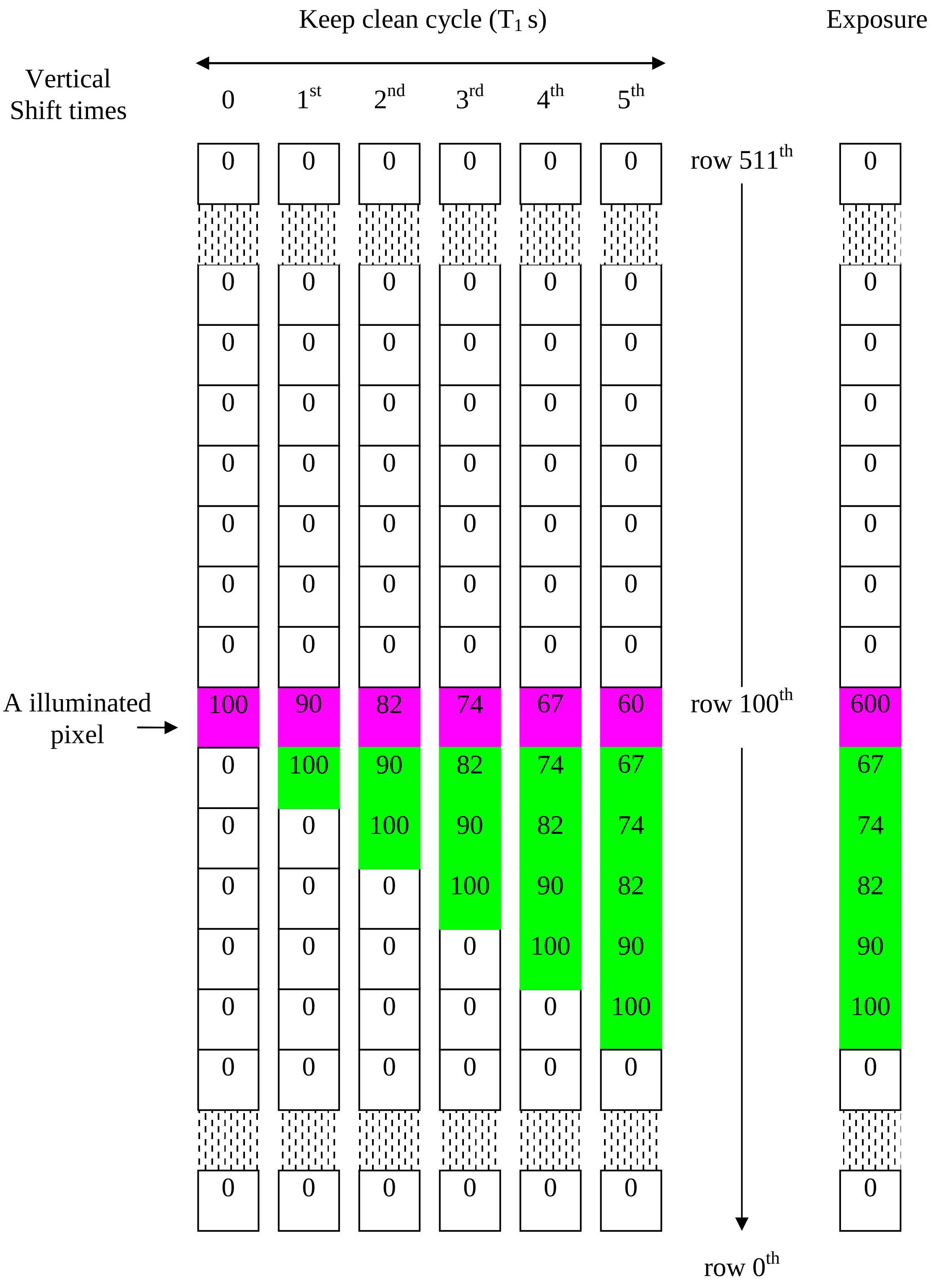
Keep clean cycle (T_1 s)
Exposure
Vertical Shift times
A illuminated pixel
row 511th
row 100th
row 0th

0	1st	2nd	3rd	4th	5th	Exposure
0	0	0	0	0	0	0
⋮	⋮	⋮	⋮	⋮	⋮	⋮
0	0	0	0	0	0	0
0	0	0	0	0	0	0
0	0	0	0	0	0	0
0	0	0	0	0	0	0
0	0	0	0	0	0	0
0	0	0	0	0	0	0
0	0	0	0	0	0	0
100	90	82	74	67	60	600
0	100	90	82	74	67	67
0	0	100	90	82	74	74
0	0	0	100	90	82	82
0	0	0	0	100	90	90
0	0	0	0	0	100	100
0	0	0	0	0	0	0
⋮	⋮	⋮	⋮	⋮	⋮	⋮
0	0	0	0	0	0	0

Figure 3.19: The creation of streaking in the case 1

The case 2: The exposure process finishes before the closing of the camera's shutter (figure 3.20).

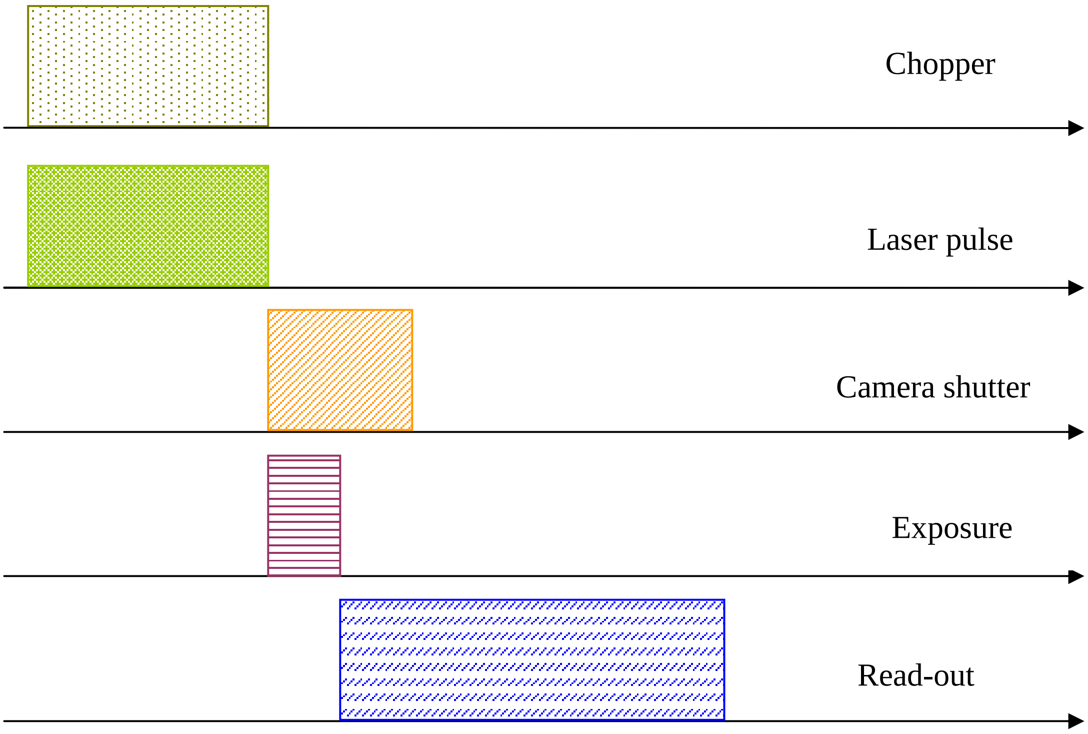

Figure 3.20: The exposure process is too short

The read-out process begins by quickly shifting charges from the image area towards the storage area. However, the image area is still illuminated because the camera's shutter is still open. Every row before row 100th will pass through the illuminated position and collect contaminating charges (figure 3.21). The number of contaminating charges depends on the light intensity and the selected vertical shift speed.

Similarly to the case 1, we can estimate the decay constant of light from the values of pixels from row 99th to 0th and the vertical shift speed.

The camera Andor iXon3 DU-897D support five vertical shift speeds in the read-out process: 0.3 - 0.5 - 0.9 - 1.7 - 3.3 microseconds. In the external trigger mode, the vertical shift speed of "keep clean cycle" process is 6.6 microseconds (see section 3.3.2). The fluorescent lifetime of Tb complex is of some milliseconds, therefore the longer vertical shift speed of the first method is more convenient to measure it.

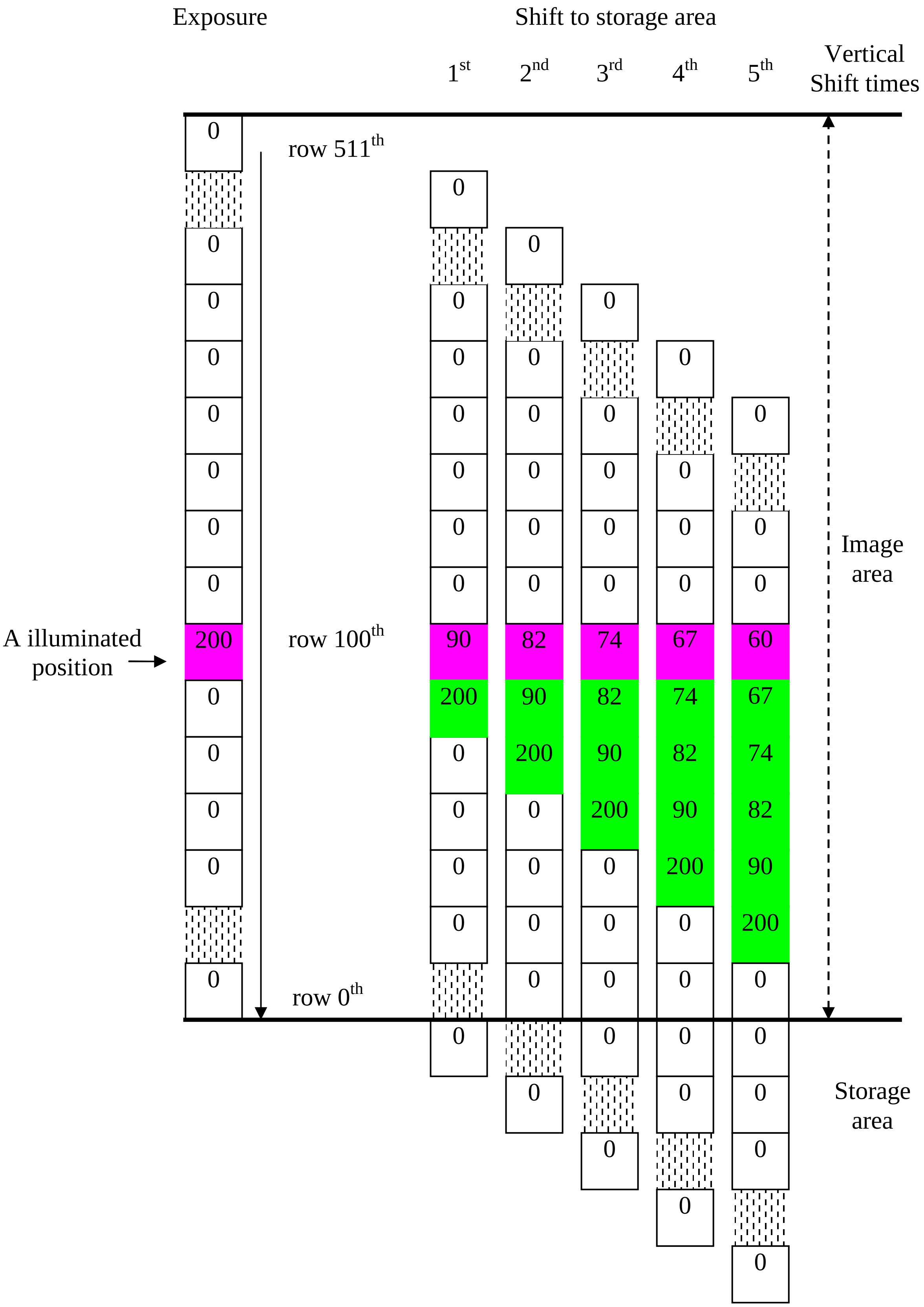
Exposure
Shift to storage area
1st
2nd
3rd
4th
5th
Vertical Shift times
row 511th
row 100th
row 0th
A illuminated position
Image area
Storage area
0
200
90
82
74
67
60

Figure 3.21: The creation of streaking in the case 2

3.3.2 Application of vertical shift for lifetime measurement

From the section 3.3.1, it is clear that we can use the streaking effect of an EMCCD camera to measure the lifetime of long decay fluorescence. In this section, we will use the first method to measure the fluorescent lifetime of terbium ions in solution.

A P717-Tb solution layer is kept between two quartz slices separated by a few dozen micrometers. The laser beam is focused on the P717-Tb layer by a single lens. The fluorescent image of the solution is a tiny dot on CCD sensor, so the result of the streaking is not too affected by spatial convolution by the dot’s size. The streaking is controlled by changing the value of exposure delay T_1 (see figure 3.18).

.

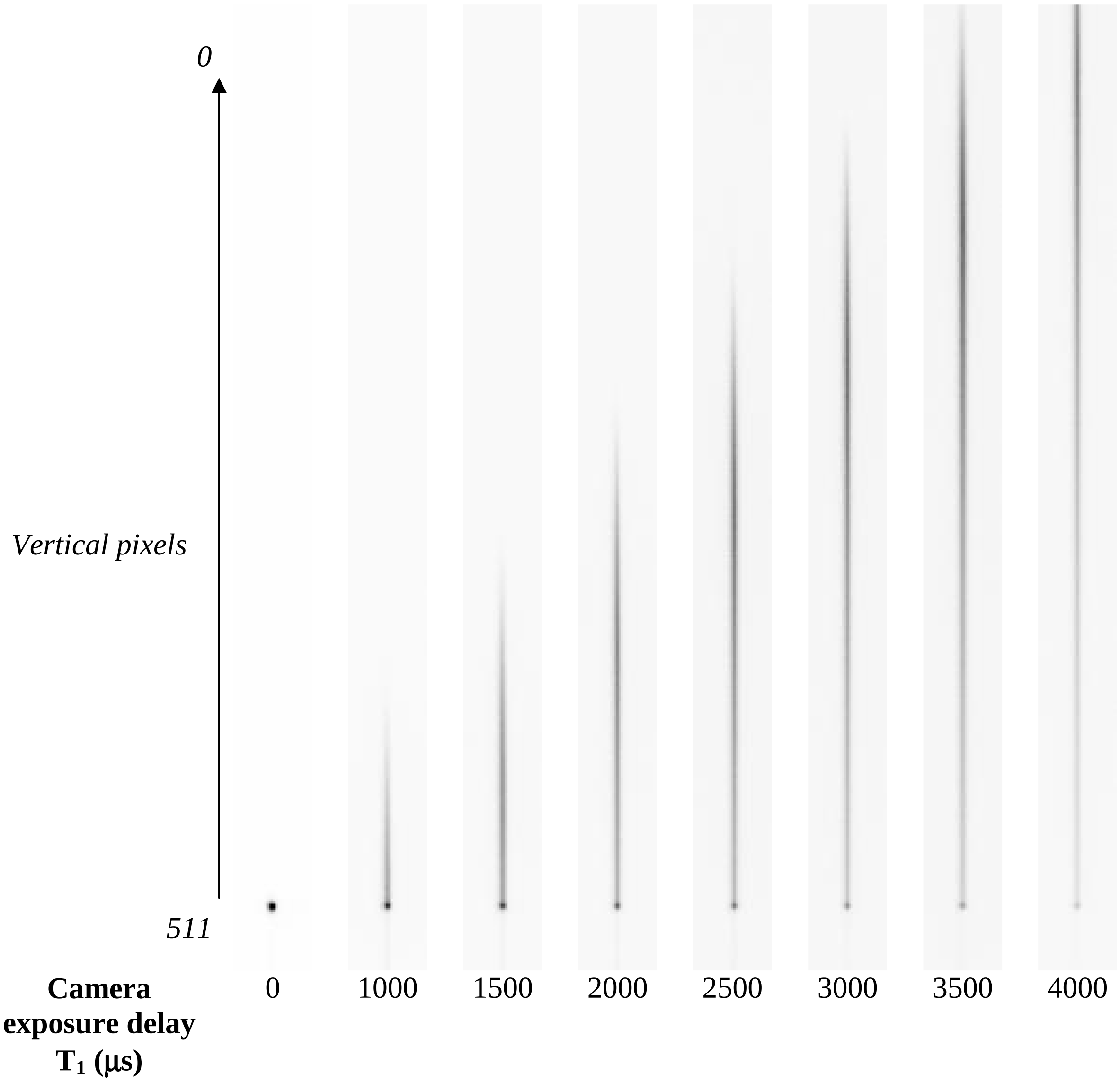

Figure 3.22: The streaking lines at different T_1 values in the case 1 (the color is inverted)

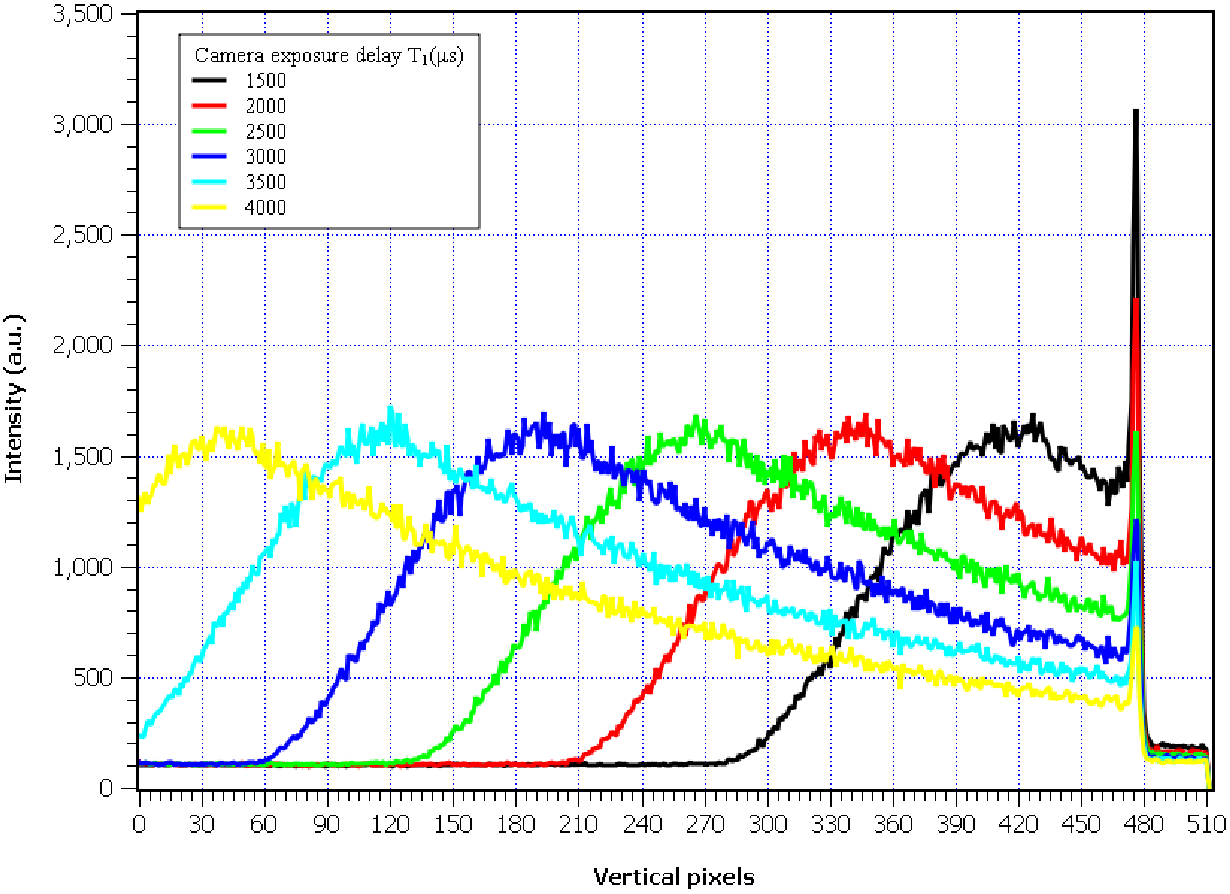

Figure 3.23: streaking from one pixel column at different T_1 values in the case 1

To estimate the lifetime of fluorescent light, we need to know the period T_{shift} to move charges from one row to the next. The technical documentation of EMCCD Andor iXon3 doesn't provide the vertical shift speed which is used in the "keep clean cycle" process.

The figure 3.23 shows the evolution of streaking lines at different camera exposure delays. The opening of camera shutter and the decay of light intensity cause the left rising edge. The right falling edge is caused only by the decay of light.

The peak intensity of all charts is the same. It shows that all charges in any pixel are move perfectly to the next. The position of the peak moves to lower pixel when T_1 increases. The figure 3.23 shows the dependence of peak position in pixel on the T_1 value (black dot). We fit the data to linear function by the SciDAVis software

$$y = A*x + B$$

and the result is:

$A = - 6.61 \pm 0.03 \mu s/pixel$

$B = 4260 \pm 8 \mu s$

with the coefficient of determination $R^2 = 0.999915$

This result shows that the vertical shift speed of camera in the "keep clean cycle" process is 6.6 microseconds. It means that the time for a charge to move from pixel 511th to pixel 0th is 6.6 x 511 = 3372.6 microseconds.

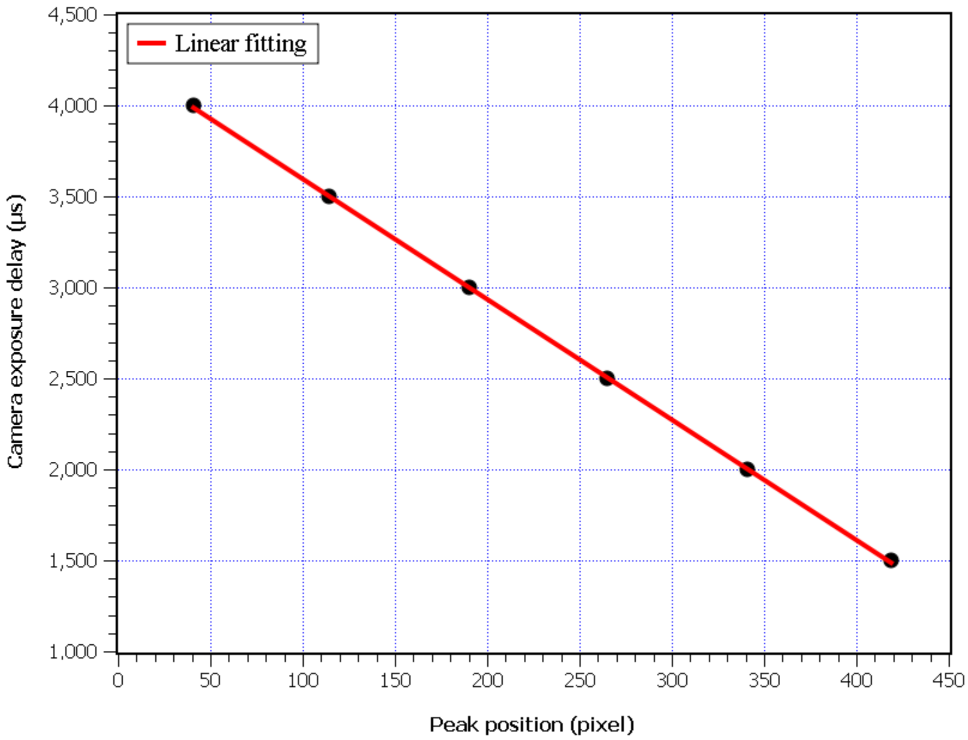

Figure 3.24: dependence of the peak position in pixels on the T_1 value

The figure 3.25 shows the fluorescent decay data of P717-Tb when it is dissolved in pure water. This data is fitted to an exponential function by the SciDAVis software:

$$y = y_0 + A * \exp(-x/t)$$

with the result is:

A = 920 ± 28

t = 1.18196 ± 2.0e-05ms

y_0 = 100 ± 10

R^2 = 0.99694

The fluorescent lifetime for the terbium ion was 1182 microseconds. The measurement time in figure 3.25 excess the maximal value of 6.6x511=3372.6 microseconds by merging acquisitions at different T_1 values. It is similar to the values which are published in the literature [50], [69].

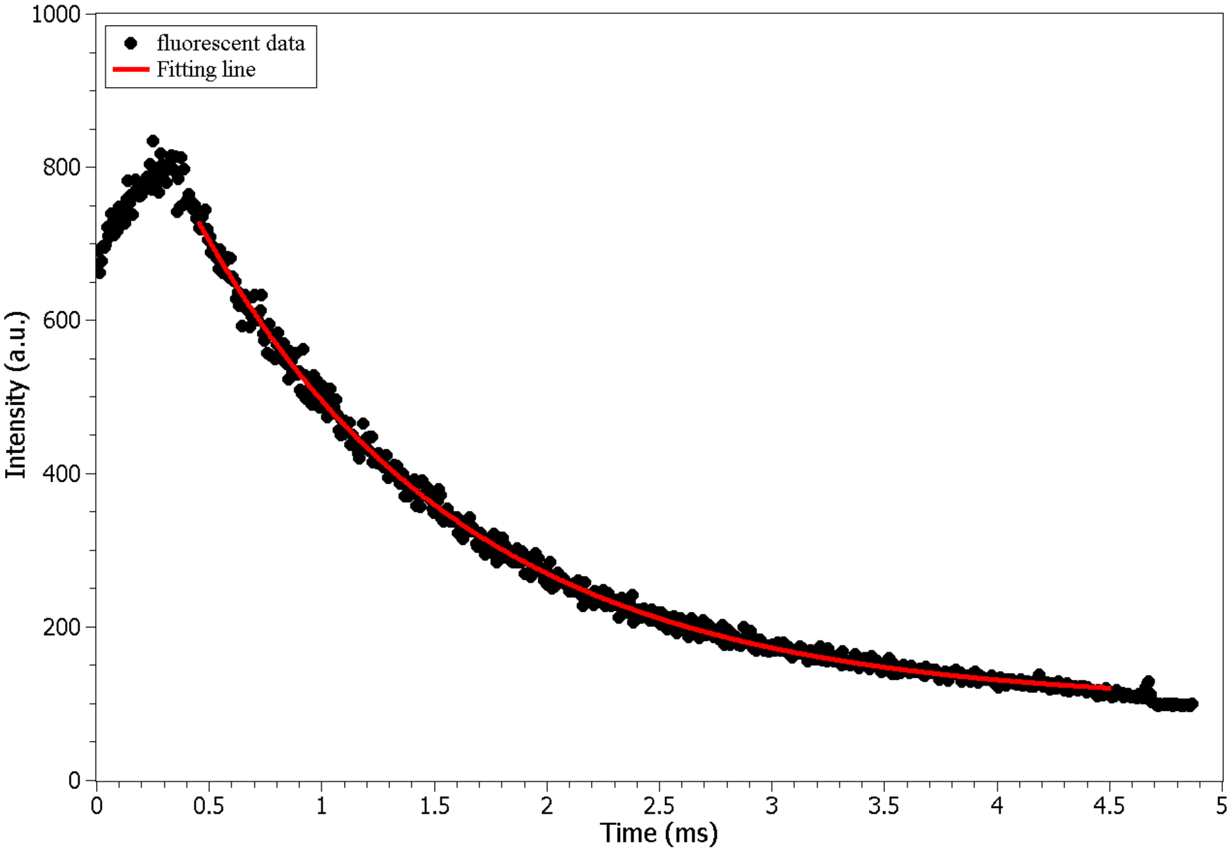

Figure 3.25: The decay data of P717Tb in pure water

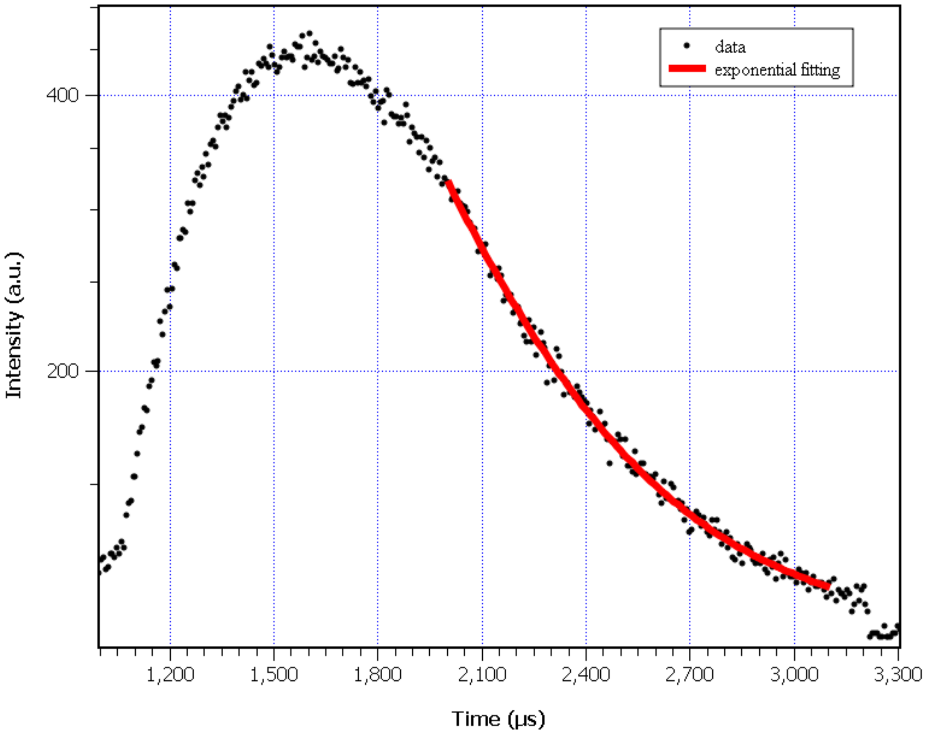

Figure 3.26: The decay profile of $TbCl_3$ in pure water

We also used this method to measure the fluorescent lifetime of terbium ion in the $TbCl_3$ when it is dissolved in pure water. We present the result in figure 3.26. The fluorescent lifetime of terbium in the solution of $TbCl_3$ is 388 microseconds. This is consistent with results published in the literature [58], [57].

3.4. Conclusion

In this chapter, we present how we can use the camera to measure the number of photons incident on a pixel. This gives us hope to evaluate the fluorescence absolute intensity therefore to estimate the concentration of the fluorescent agent in the sample, provided we know many other parameters like the optical system's function.

We also present the causes of the streaking effect on the CCD camera and how to use this effect to measure the fluorescent lifetime in the range from some hundreds to some milliseconds.

We present some experimental estimations of the fluorescent lifetime of terbium ion in solution of P717Tb and $TbCl_3$.

This method allows us to measure the fluorescent lifetime by one excitation pulse only. It could be extremely useful when the fluorescent particle is photo bleached quickly.

Chapter 4

P717-Tb Experimental results

This chapter presents the experimental results of optical properties of P717-Tb in solution and in rat artery. Fluorescent images of artery specimens labeled by P717-Tb are presented.

4.1 Synthesis of the fluorescent molecule

We have prepared 2 fluorescent contrast agents:

(i) P717 complexed with Tb3+ ions (P717-Tb)

(ii) P717-Tb linked to fucoidan (P717-Tb-F) to endow it with biospecificity for platelets.

4.1.1 Synthesis of P717-Tb

P717-Tb have been prepared from a precursor, LP717, namely the carboxymethylated dextran-DOTA macro molecule. This polymer was produced by Guerbet Laboratories for this project. When complexed with gadolinium ions it has been used as a blood pool agent [70]. As previously mentionned (§ 1.4.2) DOTA is often used as a ligand for lanthanide complexes [50], [71], [72]. There are 0.23 DOTA group per glucosidic unit in each macro molecule, and the relaxivity is about 10 /mM Gd/s in the frequency range from 20 to 200 Mhz [73].

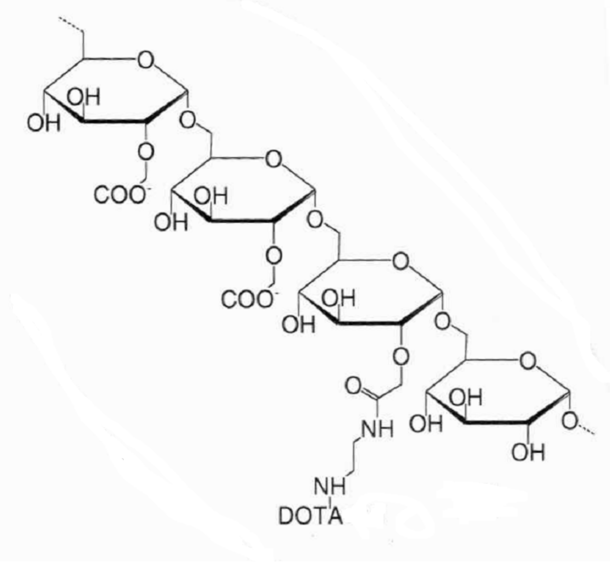

Figure 4.1: Schematic structure of LP717 molecule

The fluorescent molecule - P717-Tb - synthesis is performed from LP717 – with the aid of our colleagues in the Inserm 1148 unit. The flowchart of the synthesis process is shown on the figure 4.2. Protocols are easy to handle and complexes were obtained in a few days in good yields.

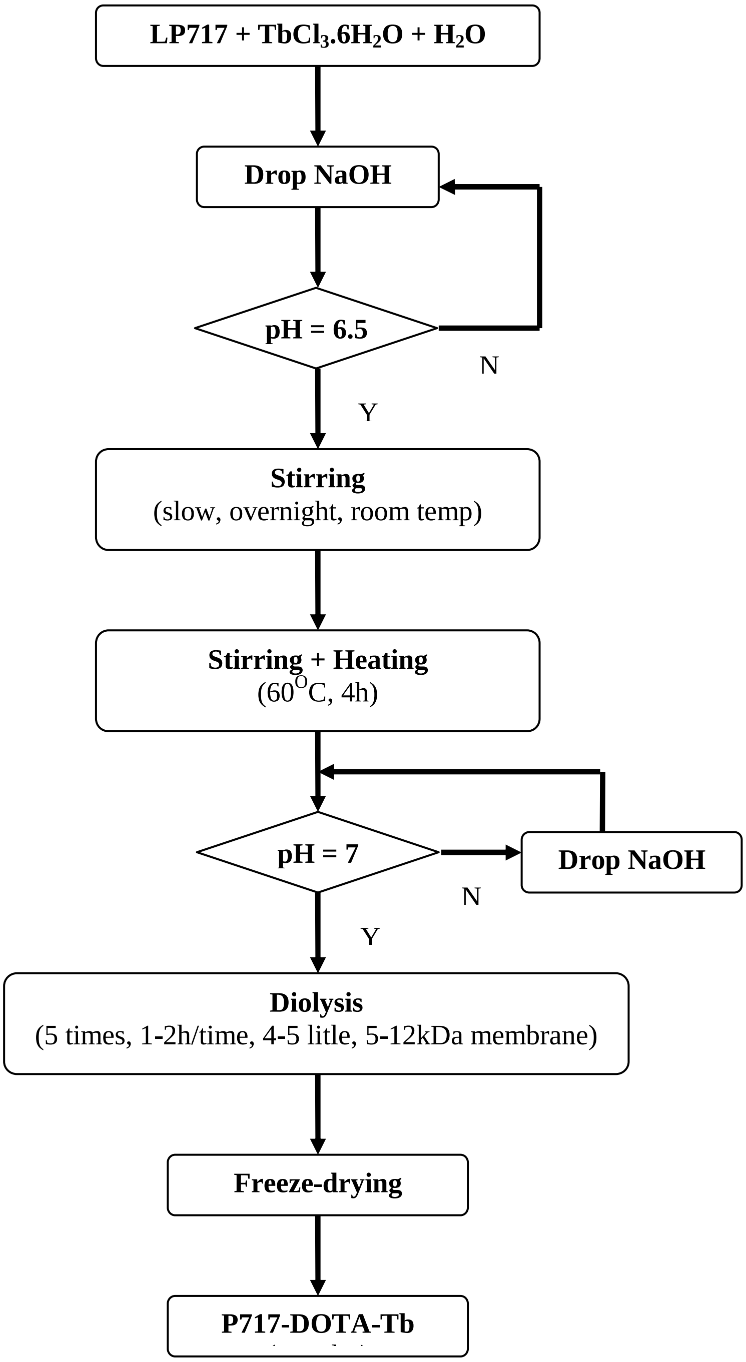
LP717 + TbCl3.6H2O + H2O
Drop NaOH
pH = 6.5
N
Y
Stirring
(slow, overnight, room temp)
Stirring + Heating
(60OC, 4h)
pH = 7
Drop NaOH
N
Y
Diolysis
(5 times, 1-2h/time, 4-5 litle, 5-12kDa membrane)
Freeze-drying
P717-DOTA-Tb

Figure 4.2: The synthesis process of P717-Tb

4.1.2 Synthesis of P717-Tb-F

P717-Tb complexes were chemically linked to fucoidan in order to endow them with the capacity to bind to P-selectin in vivo.

Description of fucoidan

Fucoidans refer to a type of polysaccharide which contains high percentages of L-fucose and sulfate ester groups, mainly derived from brown seaweed [74], [74]. Since the

1990's, some researchers from Inserm U1148 have a long experience in the field of fucoidan research [75], [76]. Fucoidan structure involves sulfated fucose polymer: [→3)-α-L-Fuc(2OSO$_3^-$)-(1→4)-α-L-Fuc(2,3diOSO$_3^-$)-(1]$_n$ (figure 4.3).

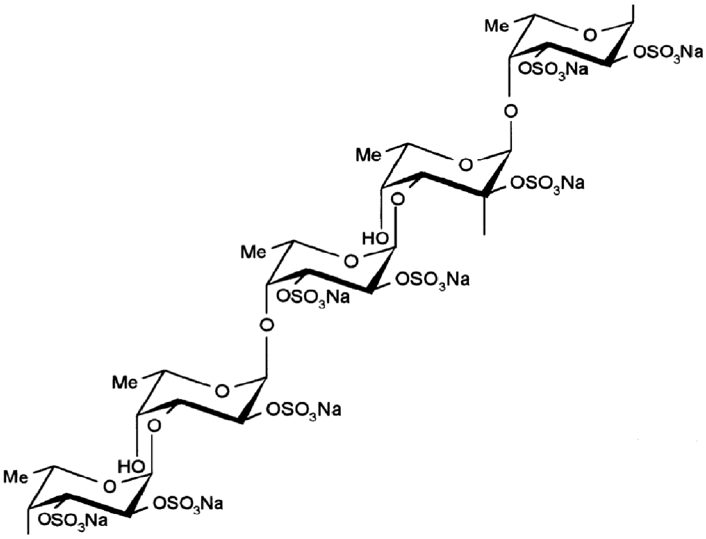

Figure 4.3: Schematic structure of fucoidan extracted from Ascophyllum nodosum [19]

Fucoidans have a large panel of biological actions, including anti-inflammatory, anticoagulant, anti-angiogenic, and anti-adhesive activities [78]. The interaction of P-selectin with different low molecular weight polysaccharide (fucoidan, heparin and dextran sulfate) has been compared [19]. Using several binding assays (microtiter plaques, mass spectrometry, surface plasmon resonance, flow cytometry on human whole blood) it was evidenced that fucoidan: i) prevented P-selectin binding to Sialyl Lewis X with an IC(50) of 20 nM (as compared to 400 nM for heparin and >25 000 nM for dextran sulfate), ii) exhibited the highest affinity for immobilized P-selectin with a K_D of 1.2 nM (two orders of magnitude greater than for the other polysaccharides), iii) formed of a complex with P-selectin. The intensity of the fucoidan binding to platelets was dependent on the level of platelet activation. Competition between fucoidan and an anti P-selectin antibody demonstrated the specificity of the interaction. As compared to antibodies or Sialyl Lewis X, fucoidan is a low cost product, and already produced by several companies.

In 2011, Rouzet *et al* demonstrated that ^{99m}Tc radiolabelled fucoidan was able to detect different vascular thrombi and activated endothelium in different experimental models with a high sensitivity and specificity [79]. More recently fucoidan-coated USPIO were evidenced as able to strongly bind to activated human platelets [80].

Experimentals

The link of fucoidan to complexes was performed as following: (i) amination of the reductive end of the fucoidan to introduce one primary amine/fucoidan molecule, (ii) coupling of aminated fucoidan with some free carboxymethyl groups of the complexes via EDC/NHS classical strategy.

Amination

5.4 mL of 1.5 M diaminopropane in glacial acetic acid was added to 500 mg of fucoidan in a glass tube. The tube was sealed and heated to 90°C for three hours. Then, the tube was cooled before adding 1.4 mL of 3 M dimethylborane in acetic acid. The tube was again sealed, heated to 90 °C for three more hours, cooled and then neutralized with diluted sodium hydroxide (NaOH). The product was then dialyzed (cut-off 1000 Da) five times against a carbonate buffer pH 9.6 with 1 M NaCl, five times against a water/ethanol (80/20) solution with 0.5 M NaCl and five times against distilled water. Finally, the product was frozen at -80 ° C and lyophilized.

The amount of primary amine was determined with phtalaldehyde colorimetric assay using bromopropylamine as the standard 50.

Chemical composition (w/w): fucose, 39.4 ± 5.0 %; uronic acids, 13.8 ± 1.5 %; sulfate groups, 29.7 ± 2.0 %. Molecular weights: =7,800 g/mol; =10,600 g/mol.

EDC/NHS Coupling

The P717-Tb was then coupled with aminated fucoidan by coupling reaction with conventional agents EDC/NHS (1-Ethyl-3-(3-dimethylaminopropyl) carbodiimide hydrochloride / N-hydroxysuccinimide). Briefly, 300 mg of P717M are dissolved in 5 mL of bidistilled water. 20 mg of EDC and 12 mg of NHS were added and stirring was maintained for 15 min at room temperature. 200 mg of aminated fucoidan were added to the mixture ([fucoidan]= 40mg/ml) and maintained under agitation for 2 hours more. Purification was performed by dialyzing the suspension against NaCl 1M (2x) and bisdistilled water (5x) Finally, the conjugate was obtained as a fluffy powder after freeze-drying.

4.2 Optical properties of P717-Tb in solution

P717-Tb is dissolved in phosphate buffered saline (PBS) – P717-Tb/PBS. The solution is kept between two quartz slides with a controlled spacing.

4.2.1 Spectrum

The emission spectrum of P7171-DOTA-Tb/PBS solution with a concentration equal to 10mg/mL (the molar concentration of terbium ions is 4.6x10-3 mol/L) is presented on the figure 4.4. We can note the four peaks characteristic of terbium ions: 488 nm; 545 nm; 586 nm and 620 nm. It is of course similar to the spectra which are published in [55], [69].

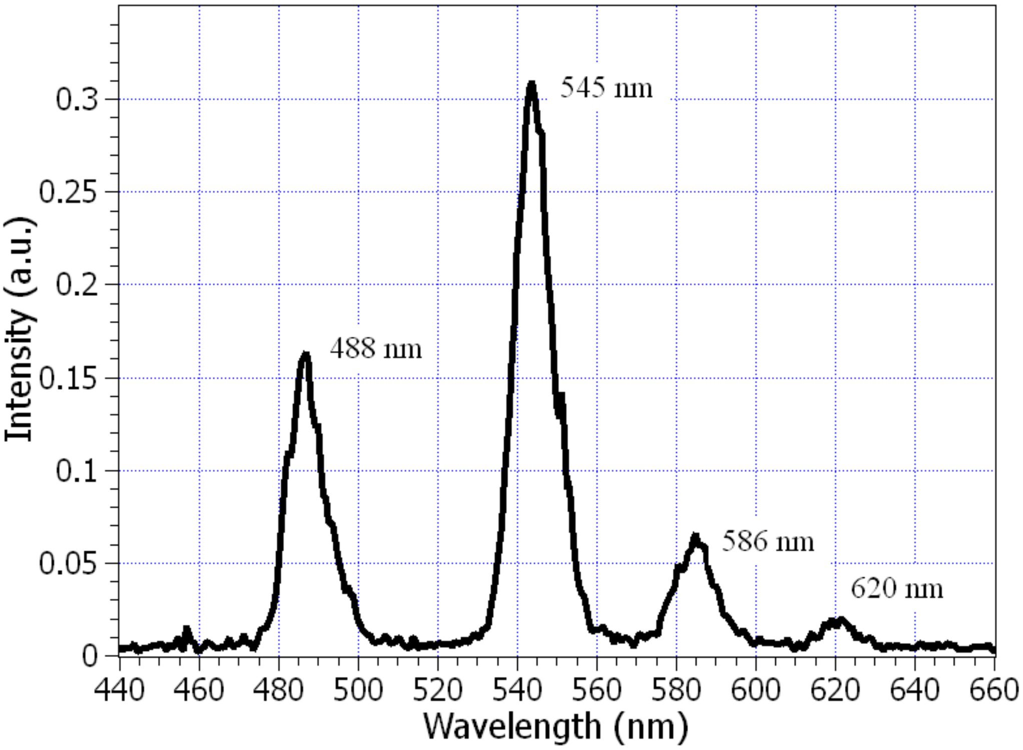

Figure 4.4: Spectrum of terbium ions in the P717-Tb/PBS solution

4.2.2 Fluorescent lifetime

We measure the fluorescent lifetime of terbium ion in solution by the use of the method we described in section 3.3. The data are acquired at some different values of the camera exposure delay T_1. Then all data are assembled to get a larger range for the delay in time.

Figure 4.5 shows this result when the data was measured at different T_1: 4000, 5500 microseconds.

The fitting procedure gives us:

A = 1438 +/- 5.0

T = 1.980 +/- 0.0076ms

y_0 = 82 +/- 6.9

R^2 = 0.99435

We can see that the coefficient of determination is close to 1 and the y_0 value matches the background average intensity at the gain of 1000x (see section 3.9). The fluorescent lifetime of terbium complex in PBS is 1980 ± 8 microseconds. It is similar to the values are published in the literature [50], [69].

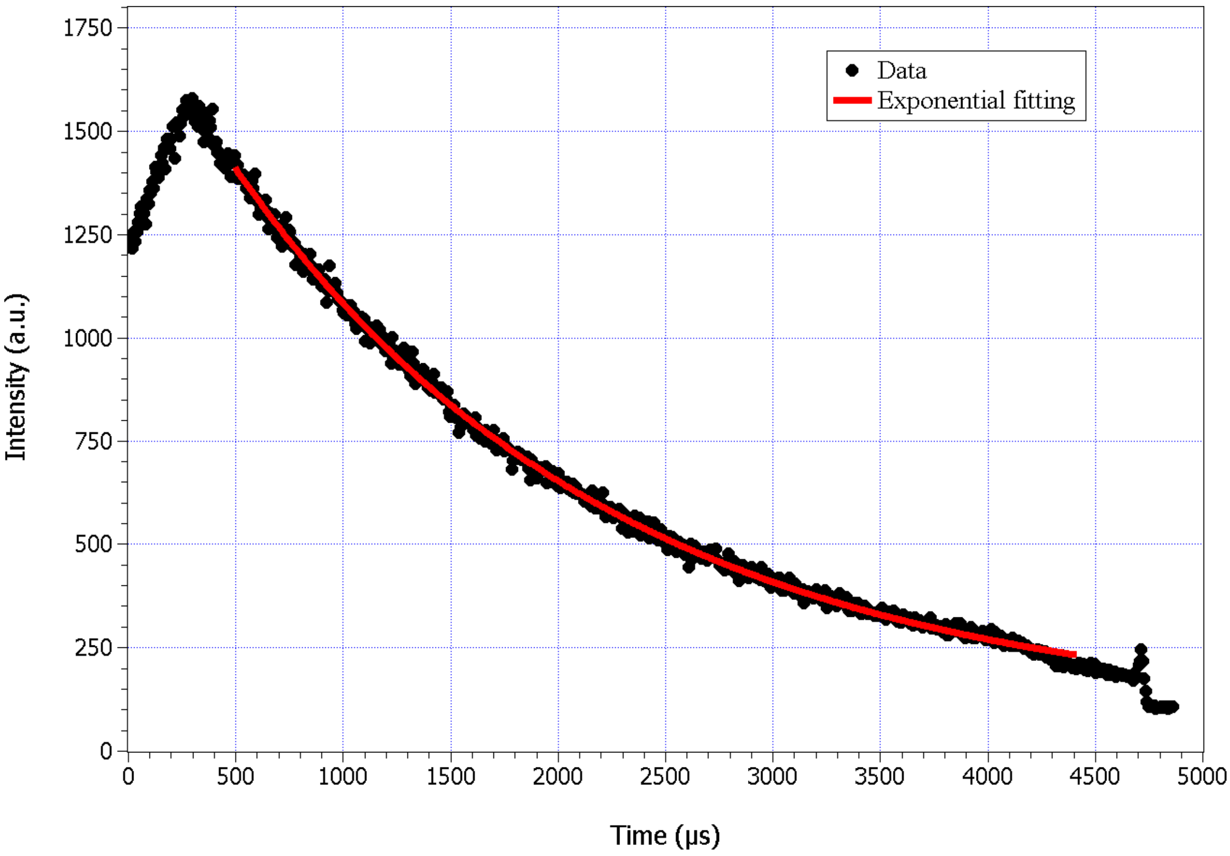

Figure 4.5: The fluorescent lifetime of P717-Tb/PBS

4.2.3 Absorption cross-section

It is very difficult to measure directly the absorption cross-section of Tb^{3+} in a complex. The absorption spectrum of Tb^{3+} in the near UV, so the ligand absorbs excitation light too. It is not easy to know which part of this light is absorbed by Tb^{3+}. In the appendix A, we developed a theory which allows us to measure indirectly the value of absorption cross-section.

In the appendix A, we proved that, when the very thin layer sample is excited, the total emitted photons that are collected by a microscope system can be approximated by the formula:

$$n_p \approx \frac{\pi\rho YNLw^2}{2}\ln\left(1+\frac{2\tau\sigma}{\pi w^2 h\nu_e}P\right)$$

where N is the collection efficiency of the microscope system, P is the excitation power, $h\nu_e$ is the photon energy, w is the beam radius of the excitation light and L is the thickness, σ is the absorption cross-section, ρ is the emission particle density, Y is the quantum yield, and τ is the fluorescent lifetime of the sample. If the camera has quantum yield η, the total of photoelectrons that camera acquire is

$$n_e \approx \frac{\pi\rho\eta YNLw^2}{2}\ln\left(1+\frac{2\tau\sigma}{\pi w^2 h\nu_e}P\right)$$

When P is low, we have

$$n_e \approx \frac{Y\rho\eta NL}{h\nu_e}\tau\sigma P-\frac{Y\rho\eta NL}{\pi(h\nu_e)^2}(\tau\sigma)^2P^2 = AB\sigma P-\frac{1}{2}A(B\sigma)^2P^2$$

with $A = \frac{\pi\rho\eta YNLw^2}{2}$ and $B = \frac{2\tau}{\pi w^2 h\nu_e}$

This theory is verified by the investigation of solutions of $TbCl_3$ dissolved in water. The excitation light power is adjusted from 0.2 to 4.6 mW. Emission light is collected by x20 magnification objective with NA=0.4. The lost of light in the optical path is 1/2. So collection efficiency of the microscope system in this case is

$$N = \frac{1}{2}\frac{NA^2}{4n^2} = \frac{1}{2}\frac{0.4^2}{4*1.33^2} = 0.0113$$

The excitation light has only one peak at 371nm. Its full width at half maximum is 2nm. The average photon energy of excitation light is $5.30*10^{-16}$ mJ.

The quantum efficiency of camera in the range 400 nm to 500 nm is 0.95.

The optical properties of the $TbCl_3$ solution are shown in the table 4.1

Table 4.1: optical properties of the TbCl3/H₂O solution

Density of Tb^{3+} (μm^{-3})	ρ	$1.63*10^6$
Quantum yield of Tb^{3+} [Elbanowski 1989]	Y	0.029
Thickness of the solution (μm)	L	35
Fluorescent lifetime (s)	τ	0.00043
Absorption cross-section of Tb^{3+} (@371nm) (μm^2) [Gschneidner 1979, p. 179]	σ	$6.876*10^{-14}$

We thus have

$$\left(AB\sigma\right)_{theory} = \frac{\pi\rho\eta YNLw^2}{2}\frac{2\tau}{\pi w^2 h\nu_e}\sigma = \frac{\rho\eta YNL\tau}{h\nu_e}\sigma = 988.33 \text{ mW}^{-1}$$

(4.1)

Figure 4.6 shows the experimental data. The relationships between the total photoelectron and excitation light is linear. It shows that the excitation intensity is very far from the saturation excitation power of Tb^{3+}. The experimental data is fitted to the first order polynomial $y = a_0 + a_1 x$. The fitting results is

a_0 = -156 ± 38

a_1 = 957 ± 15mW^{-1}

$$=> \left(AB\sigma\right)_{\exp eriment} = a_1 = 957\,\text{mW}^{-1} \qquad (4.2)$$

There is a good match between theory (4.1) and experimental data (4.2)

The optical properties of P717-Tb solution are shown in the table 4.2. All the other parameters are the same as above.

Table 4.2: The optical properties of the P717-Tb/PBS solution

Density of Tb^{3+} (μm^{-3})	ρ	10354
Quantum yield of Tb^{3+} [Xiao 2001]	Y	0.436
Thickness of the solution (μm)	L	35
Fluorescent lifetime (s) (see section 5.2.2)	τ	0.001911
Absorption cross-section of Tb^{3+} (@371nm) (μm^2)	σ	??

The relationships between the total photoelectron and excitation light is shown in the figure 4.7. Fluorescent of P717-Tb is a bit saturated. The reason may be due to the increase of the lifetime of the excited states.

The experimental data is fitted to the second order polynomial $y = a_0 + a_1 x + a_2 x^2$. The fitting result is

a_0 = -5 ± 5.8

$a_1 = 410 \pm 6.1\text{mW}^{-1}$

$a_2 = -21 \pm 1.3\text{mW}^{-2}$

$R^2 = 0.99971$

$(AB\sigma)_{\exp eriment} = a_1 = 411\ \text{mW}^{-1}$ and A = 5222.0; $B = 1.17*10^{12}$

$$=> \sigma = 6.72*10^{-14}\,\mu\text{m}^2 \qquad (5.3)$$

It can be seen that the absorption cross-sections of Tb^{3+} in P717-Tb/PBS solution (4.2) and free Tb^{3+}in aqueous (table 4.1) are the same. In P717-Tb, the Tb^{3+} ion is directly excited at the wavelength equal to 371 nm.

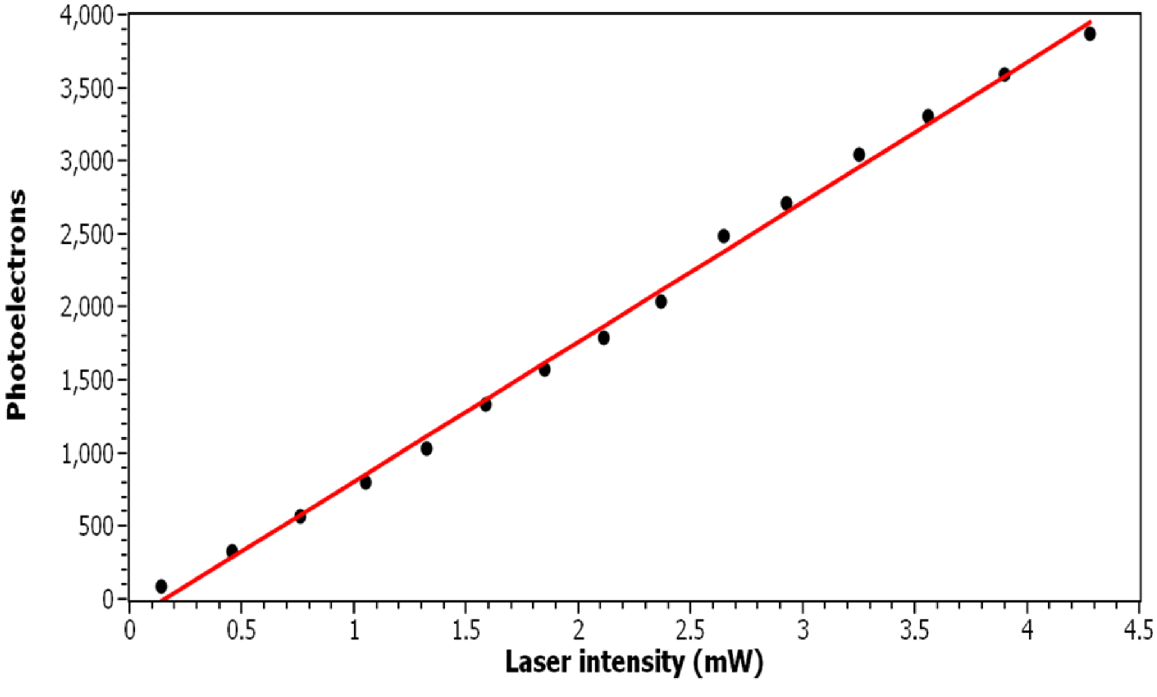

Figure 4.6: Dependence of the total number of photoelectrons on the excitation light power for the TbCl$_3$ solution

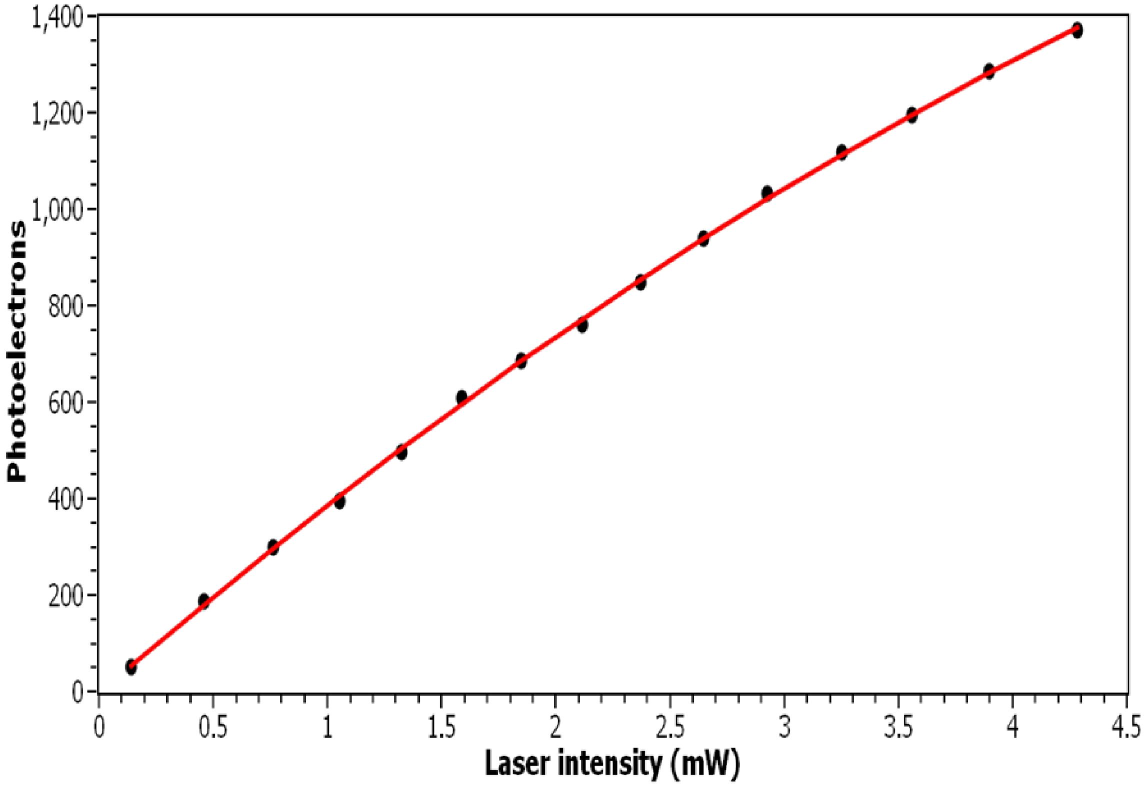

Figure 4.7: Dependence of the total number of photoelectrons on the excitation light power for the P717-Tb solution

4.3 Fluorescent images of P717-Tb/PBS in healthy artery

4.3.1 Preparation of the samples

The healthy arteries of rats are processed as presented in figure 4.8. This process was done with the help of colleagues at the Pathology department of Bichat-Claude Bernard hospital.

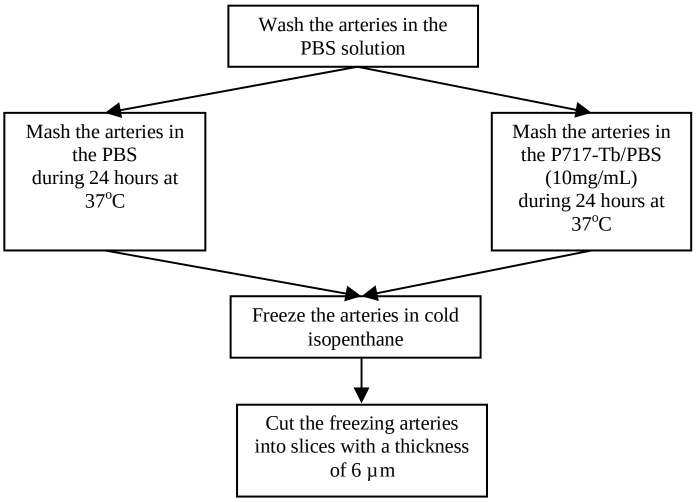
Wash the arteries in the PBS solution
Mash the arteries in the PBS during 24 hours at 37°C
Mash the arteries in the P717-Tb/PBS (10mg/mL) during 24 hours at 37°C
Freeze the arteries in cold isopenthane
Cut the freezing arteries into slices with a thickness of 6 µm

Figure 4.8: The process to prepare healthy arteries

4.3.2 Fluorescent images

Figure 4.9, 4.10 present the white field (a) and fluorescent images of artery specimens (b), which were incubated in PBS and P717-Tb/PBS solutions, respectively. We used the 20x magnification objective. The laser's spot diameter is 56 μm. Laser power is 5 mW in CW mode. Therefore, the average intensity of laser on the specimens is 250W/cm^2. During our experiment, the laser emits a squared pulse of light where the repetition rate is 7.3 Hz and the pulse duration is 6.2 ms.

The grayscale images are the white field images of specimens and noted (a). Each specimen was scanned up to six times to acquire the fluorescent image (b). Fluorescent intensity is measured in photoelectron.

In the figure 4.9, performed with artery specimens incubated in PBS as a control sample, we can observe the existence of a long lifetime emission from the media layer of artery wall. We should note that this emission only appears on the media layer of artery wall. We do not see any emission from the adventitia layer. This emission is quickly photobleached: in the sixth image (b6) there is a significant decrease of the intensity compared to the first image (b1). This parasitic emission is quite surprising as auto-fluorescence was not expected with such a delay-time, and this point will need further investigation.

For the artery wall treated by the P717-Tb/PBS solution, the emission is observed in both media and adventitia layers of the artery wall (figure 4.10). The intensity of light from the adventitia layer is stable while it decreases slightly in the media layer. The emission spectrum (figure 4.11) shows that the source of this emission is the Tb^{3+} ion. Note that the emission spectrum of figure 4.11 was recorded after a long UV irradiation time, so that the aforementioned parasitic emission was photo-bleached.

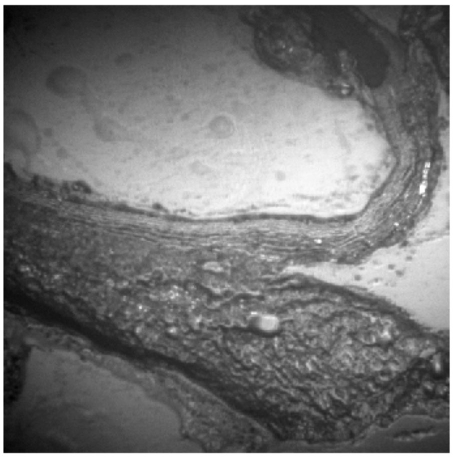

(a)

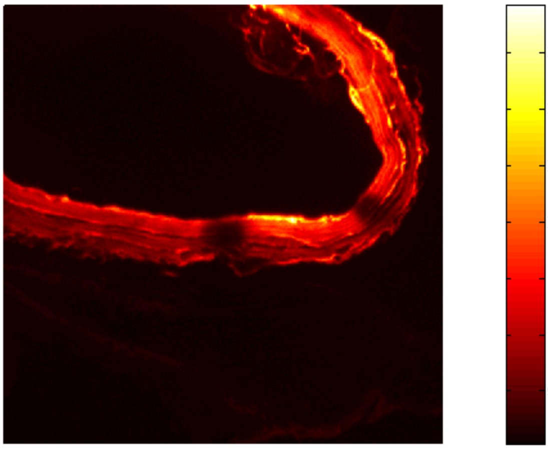
35
30
25
20
15
10
5

(b1)

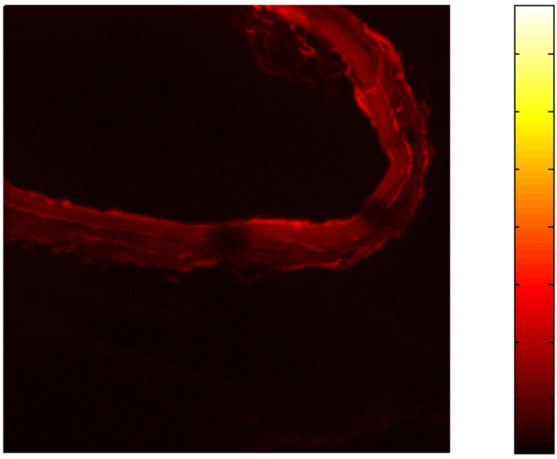
35
30
25
20
15
10
5

(b2)

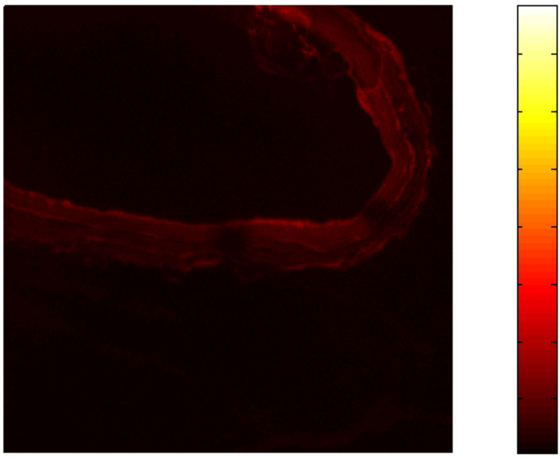
35
30
25
20
15
10
5

(b3)

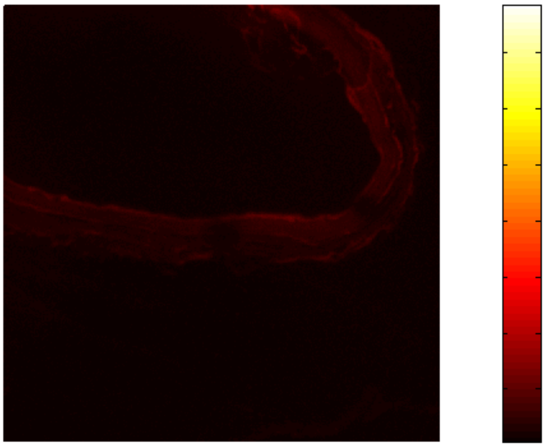
35
30
25
20
15
10
5

(b4)

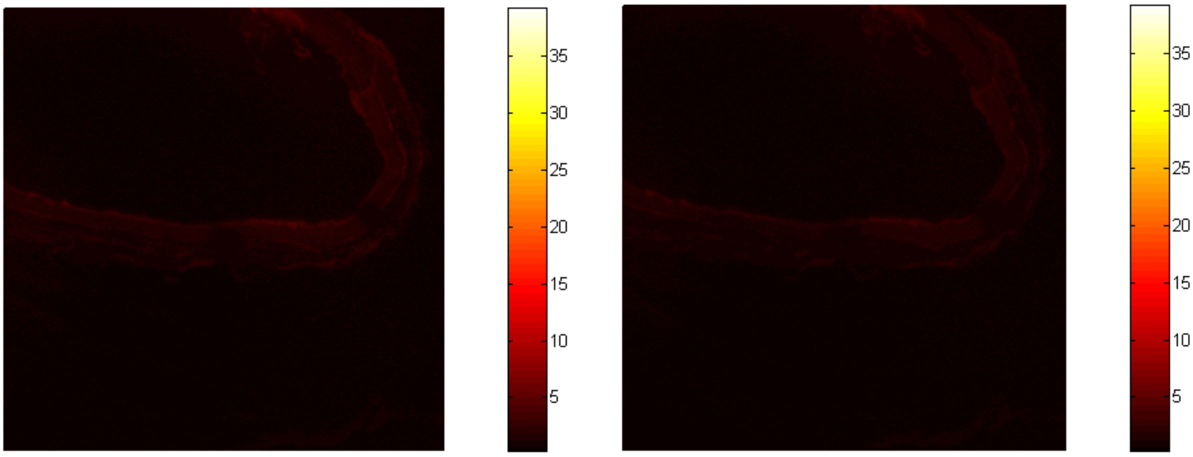
35
30
25
20
15
10
5
35
30
25
20
15
10
5

(b5) (b6)

Figure 4.9: The artery wall is treated by the PBS solution. The unit of right scale bar of fluorescence image is photoelectron. Dimension of images is 1x1 mm.

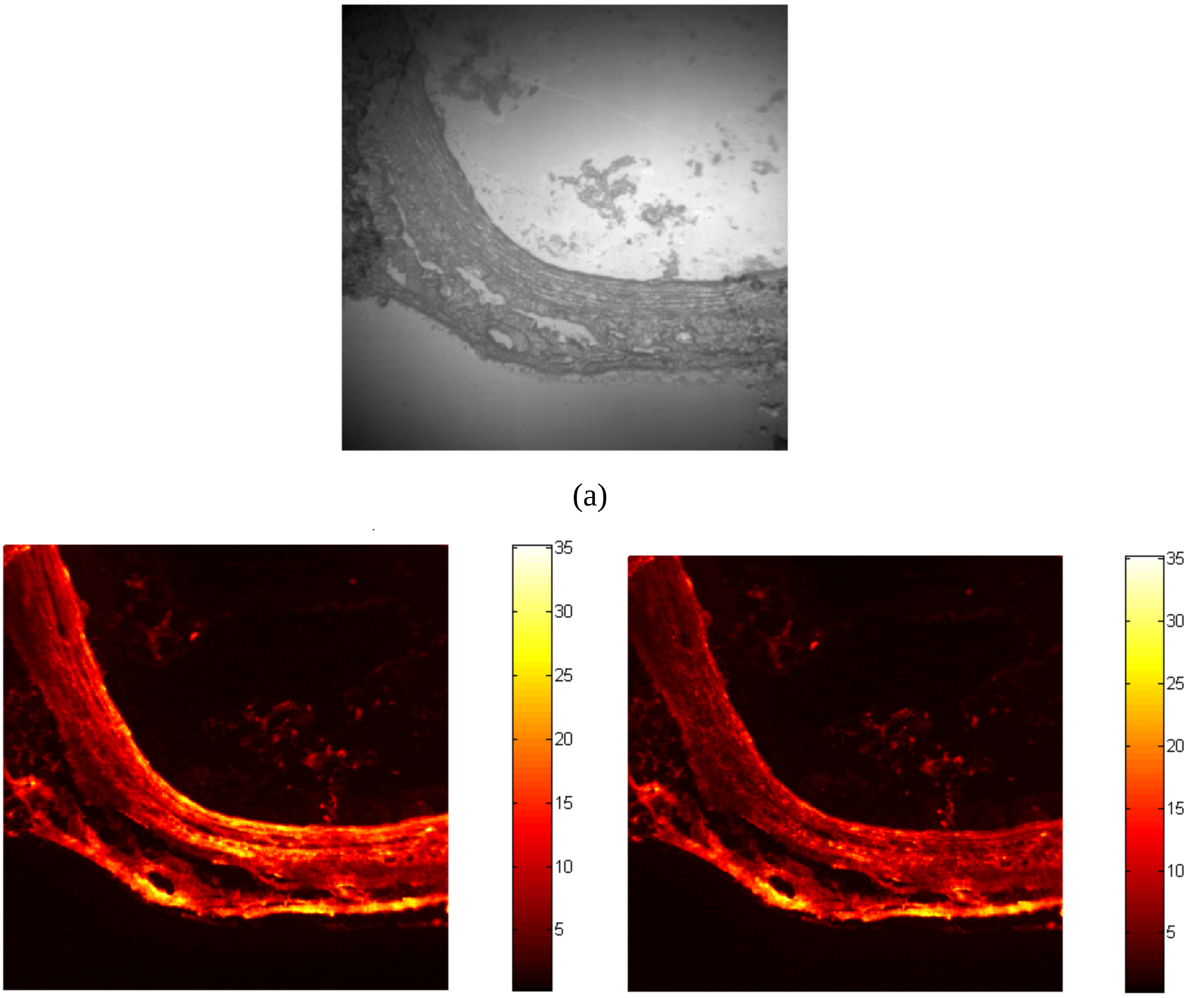
35
30
25
20
15
10
5
35
30
25
20
15
10
5

(a)

(b1) (b2)

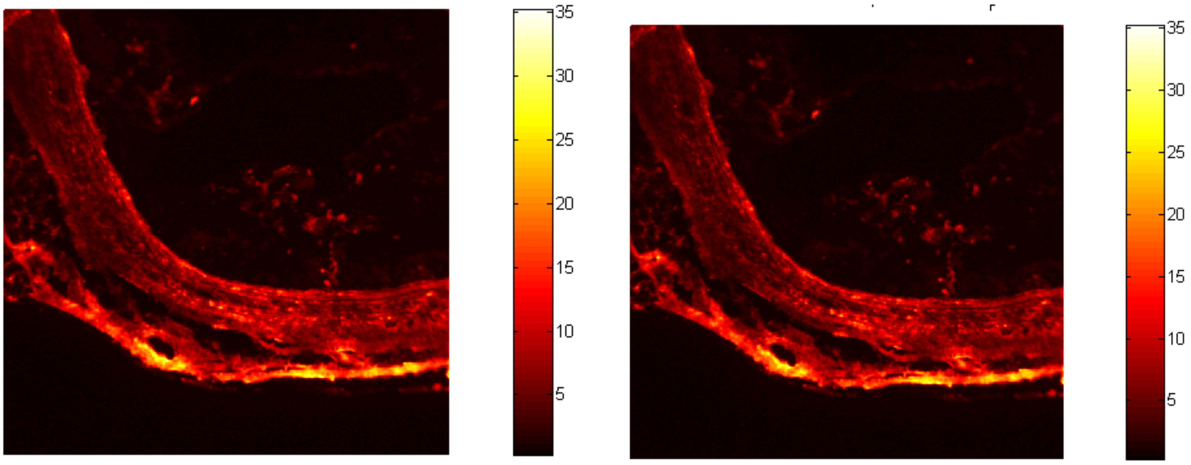
35
30
25
20
15
10
5
35
30
25
20
15
10
5

(b3) (b4)

Figure 4.10: The artery wall is treated by the P717-Tb/PBS solution. The unit of right scale bar of fluorescence image is photoelectron. Dimension of images is 1x1 mm.

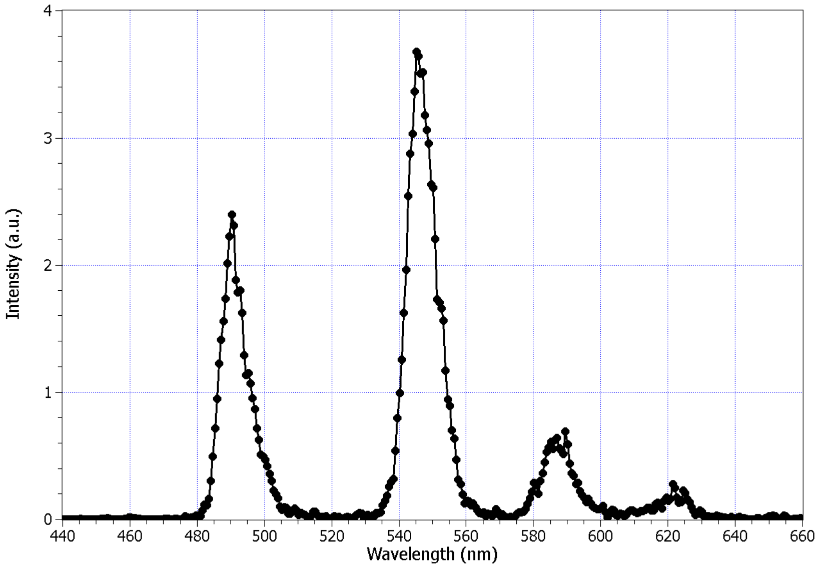

Figure 4.11: Spectrum of terbium ions in the artery specimen.

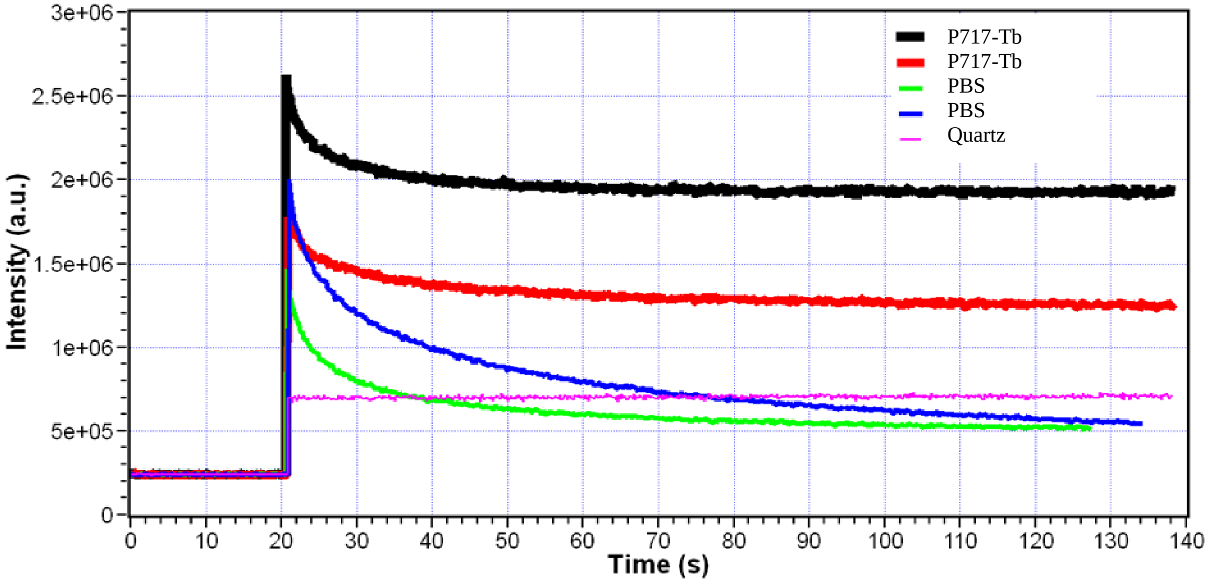

Figure 4.12: Stability of fluorescence over time

The long lifetime parasitic emission from the media layer of the artery gives a strong contribution. Fortunately, it is photo-bleached quickly while the emission of Tb^{3+} ion is more stable. Figure 4.12 presents the emission intensity versus excitation time of the artery after it was treated by P717-Tb/PBS (black and red color) and by PBS (green and blue color). The magenta color corresponds to the case when there is no artery sample (simple quartz). The laser is turn on 20 seconds after the starting of acquisition of camera. The peak intensity of laser is about 1500 W/cm^2 to accelerate the photo-bleaching effect. The bleaching happens after 30 seconds, what correspond to 210 excitation pulses. At that time, the collected intensity is even smaller than the noise coming from the system alone (simple quartz). It may be due to the extinction of UV light by the artery sample.

4.4 Conclusion

For the artery wall treated by the P717-Tb/PBS solution, the emission is observed in both media and adventitia layers of the artery wall. The intensity of light from the adventitia layer is stable while it decreases slightly in the media layer. The emission spectrum (figure 4.11) shows that the source of this emission is the Tb^{3+} ion.

Chapter 5

Experimental results on atherosclerotic rat arteries

We designed the whole system to localize and to try to quantify the fixation on pathologic arteries of fluorescent contrast agents chemically similar to those used in MRI imaging. In this chapter, we present the first experimental results. They are still very preliminary, but they show that our system can meet our expectations.

5.1 Animal model

The elastase model, developped in U1148 and performed by a skilled technician, consisted in inducing the formation of an aneurysm within the abdominal aorta of Lewis rats 12 weeks aged as described elsewhere [79]. Briefly, the model was induced under general pentobarbital anesthesia by in situ intraluminal pressurized perfusion of 3 units of pig pancreatic elastase within an isolated segment of the abdominal aorta. This model is characterized by a biologically active intraluminal thrombus, i.e. with activated platelets and a wide expression of P-selectin. Imaging was performed 15-21 days later.

5.2 Preparation of contrast agent mixtures

P717-Gd and P717-Gd-F have been prepared following the same protocols as P717-Tb complexes. MR experiments have been performed with 50/50 (Tb/Gd – w/w) mixtures.

As previously presented (section 4.1), we have prepared 4 complexes: P717-M and P717-M-F (M=Gd or Tb). Due to the high number of carboxylic groups per macromolecule of P717, we expected that a least 1 molecule of fucoidan would be linked to 1 P717 complex (likely more). The proportion was not determined. The molar mass distributions of all derivatives have been obtained by HPSEC with and the profiles were strongly overlaping (figure 5.1). All chromatograms were similar. We tried to separate P717-M-F from free P717-M and free fucoidan with low pressure size exclusion chromatography without success. As a consequence, we decided to inject crude mixtures without further purification i.e. containing P717-M, fucoidan and P717-M-F. We assumed that the compositions of the final mixtures were the same as the one before coupling with fucoidan. Fucoidan and P717-M-F would aim at activated platelets *in vivo*, but only the latter could be imaged. A 50/50 (w/w) Tb/Gd ratio was assayed.

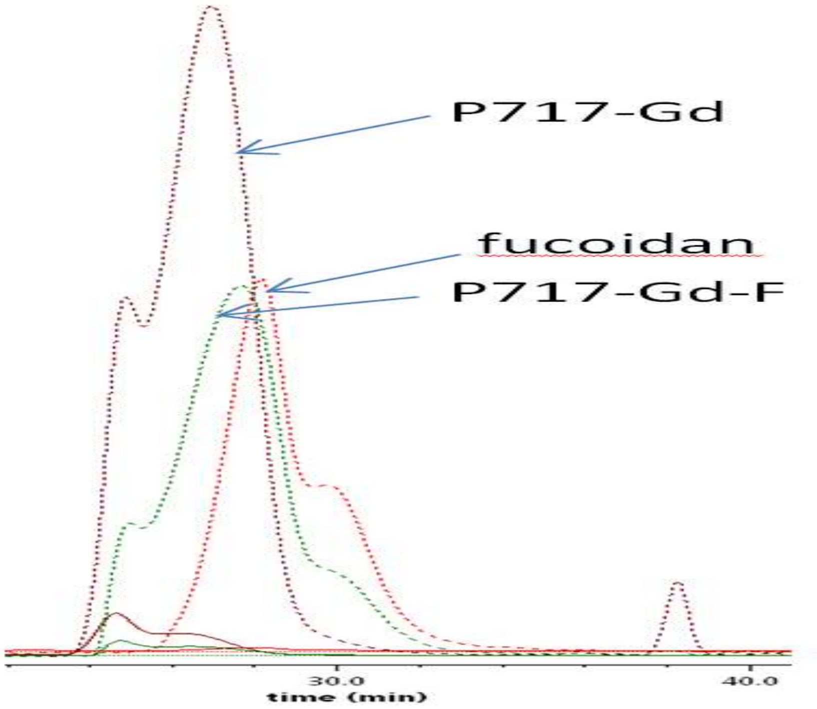

Figure 5.1 HPSEC chromatograms of P717-Gd, fucoidan and P717-Gd-F, recorded from differentiel refractometry (Columns TH802.5-803 with a pre-column, solvent = PBS 5 mM, 0.15 M NaCl, pH 7.4, flow rate = 0.50 mL/min, run time = 40 min. injected concentrations = 15 mg/mL.)

5.3 Rat abdominal aorta MR imaging

In vivo MRI experiments were conducted on 7 teslas horizontal bore magnet with 20-cm wide actively shielded gradient coils. Three weeks after operation, rats were anesthetized with a 1.5% isoflurane / O_2 gas mixture and the contrast material was injected through the penis vein. The animals were maintained anesthetized with the same gas mixture (100 cc/min maintenance dose) delivered through a nose cone and placed in a 30 mm birdcage coil with an animal handling system. Animals were scanned before and after (10, 20, 30, 50 and 90 minutes) injection of contrast material.

Four rats have been prepared for the first experiments. Unfortunately, only two rats survived. The first was used to determine the appropriate time points to record images allowing a proper MR imaging with the other one. MR images were recorded from a 7 T imager in Bichat faculty. The MR spin-echo sequence was a RARE-T1 with the following parameters : Field = 7T, TE = 9 ms, TR = 1741.9 ms, Slices: 0.80 mm/0.90 mm, matrix 256x256.

5.4 Preparation of the rat's arteries

The protocol for the preparation of the arteries slices is currently performed in U1148 [79]

Briefly, at sacrifice, relevant tissue samples were fixed in paraformaldehyde for 24 h, (dehydrated and embedded in paraffin), and cut into 6 µm sections for morphologic analysis. Serial sections were stained with Masson trichrome to visualize cells, nuclei, and fibrin and stained with Alcian blue coupled with nuclear red to reveal areas of sulfated polysaccharide material and their relation to cell nuclei. Immunohistochemistry studies were performed on 8 µm cryostat sections using goat antimouse P-selectin antibody (SC 6943; Santa Cruz Biotechnology) (1/50) vealed by an antigoat antibody conjugated with horseradish peroxidase, followed by the 3,3-diaminobenzidine reaction.

5.5 Results

All results with MR images are preliminary and should be confirmed as they have been obtained with one animal. The relaxivity of Gd complexes measured from phantoms in agarose gels with the 7 T imager was 60.1 $mM^{-1}.s^{-1}$, and the proper Gd complexes concentrations to be injected was 1.0 mg/mL. MR images are presented on the figure 5.2. Gd is a positive contrastophore i.e. an increase of the Gd concentrations within tissues corresponds to an increasing bright signal. Two aneurysmal areas have been imaged with P717-M-F. Increases of the signal within the arterial wall were observed up to 30 min after injection with mixtures of P717-M-F but not after 10 min with mixtures without fucoidan.

The fluorescence imaging of one artery slice is presented in figure 5.3. The fluorescence image (b) clearly correlates with the thrombus visible in the white light image (a, zones A1-4). The spectra recorded from different zones (figure 5.4) show that this fluorescence signal comes from terbium ions. Even if the fluorescence signal is quite low, this clearly demonstrates the expected specificity of our contrast agent, and validates our methodology. This low fluorescence level justifies *a posteriori* that development of our highly sensitive setup.

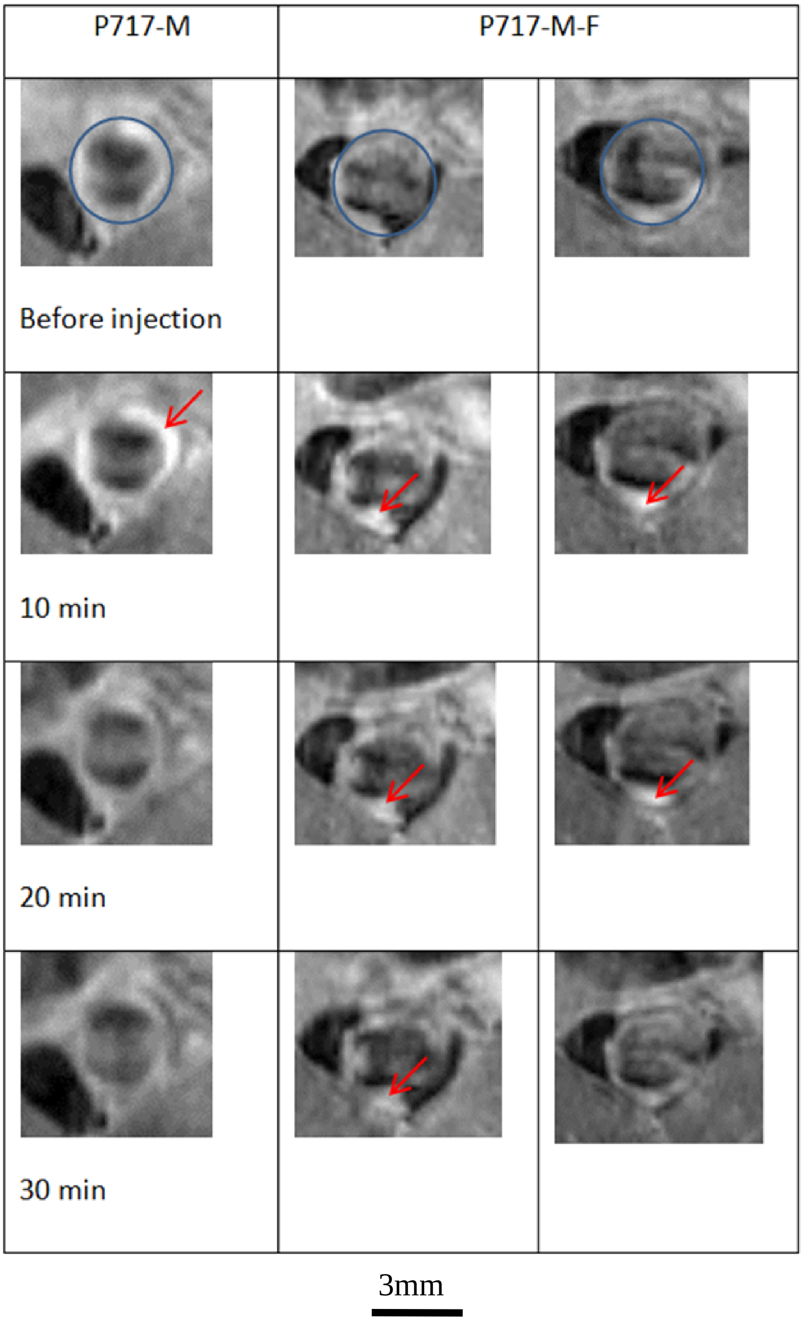

Figure 5.2 Transversal images of an abdominal aorta aneurysm (rat model). The top row depicts images recorded before injection with P717-M (left image) and with P717-M-F (M=Gd, Tb). The P717-M mixture contained 50% P717-Gd and 50% P717-Tb (w/w) and the P717-M-F mixtures contained 50% P717-Gd-F and 50% P717-Tb-F (w/w). In all mixtures, [Gd complexes] = 0.5 mg/mL. The blue circles delimit the area of interest. The other rows present images recorded 10, 20 and 30 min after injection. The contrast enhancement in the aortic wall thrombus is pointed out by red arrows. Note that the same animal was injected successiveley with P717-M and P717-M-F. The MR sequence is a RARE-T1 with the following parameters : Field = 7T, TE = 9 ms, TR = 1741.9 ms, Slices: 0.80 mm/0.90 mm.

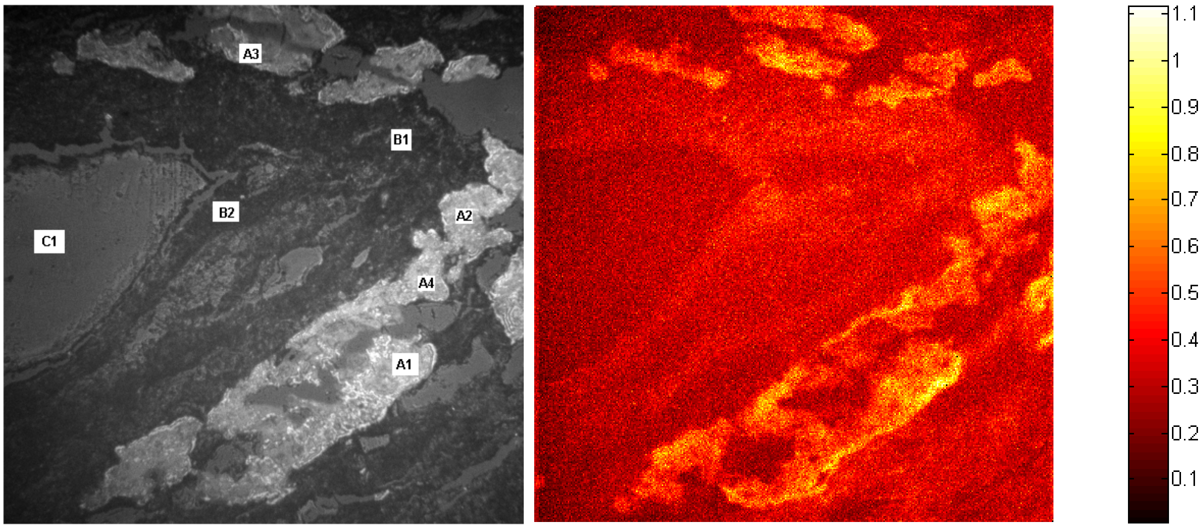
A3
B1
B2
C1
A2
A4
A1
1.1
1
0.9
0.8
0.7
0.6
0.5
0.4
0.3
0.2
0.1

(a) (b)

Figure 5.3: Bright field and fluorescent images of pathology artery slice. Dimension of image is 1x1 mm.

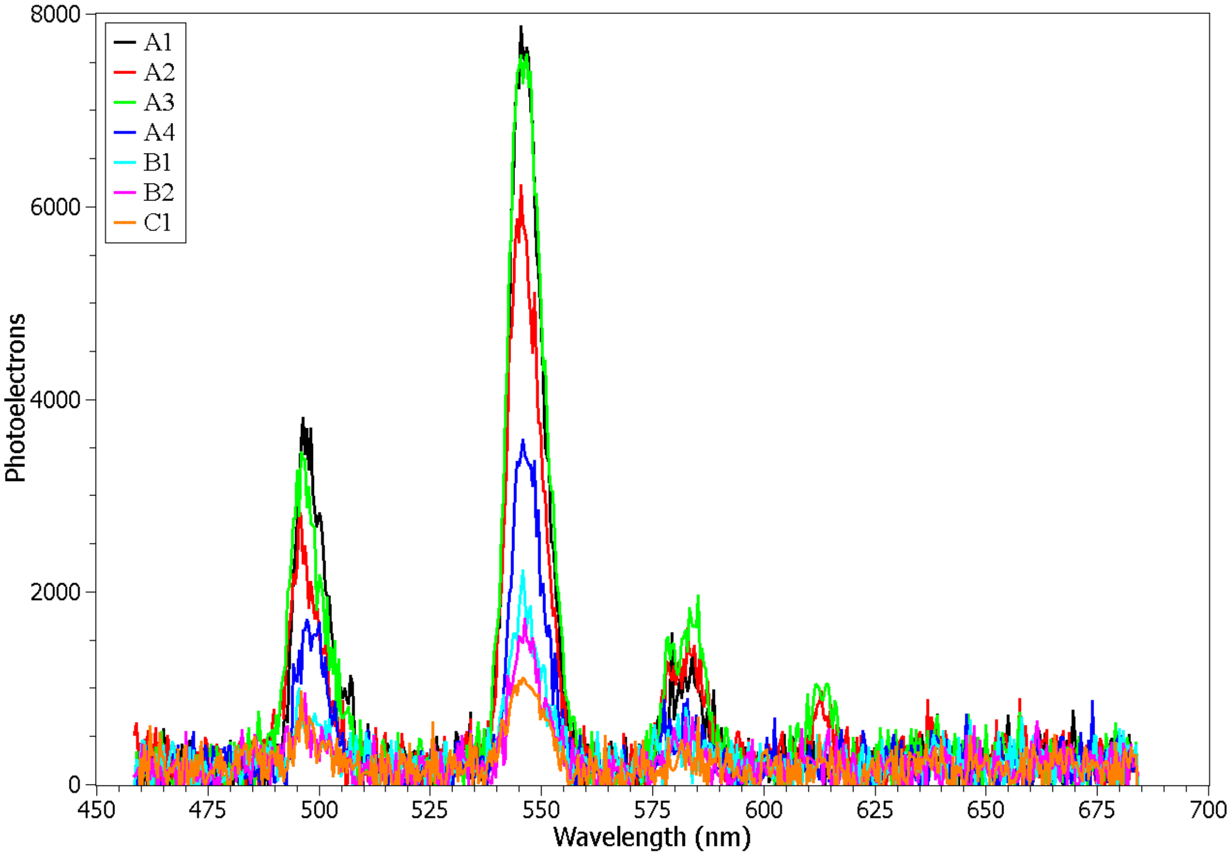

Figure 5.4: fluorescent spectra at different position of artery slice

Conclusion

I divided this conclusion into two parts. In the first one, I explain how the current system was built when I worked in the Laser Physics Laboratory. The second part corresponds to the current capability of the system.

Evolution of the experimental setup

Building a new experimental setup from scratch is both a curse and a blessing.

Difficulties arise mostly by the fact that specifications for the different elements of the setup are unknown. Of course, we could purchase the "best" for each element, like for example the most powerful, wavelength accordable, variable width pulse, etc, laser. If such a thing exists, it probably would be hugely complex and extremely expensive. It would certainly be out of our allowed budget. Even the definition of "best" for a given case is blurry. What is "best" if you do not know which parameter is the most important?

When this thesis began, we just received the microscope. Our group had several cameras inherited from previous projects, and an array of powerful UV LEDs. Let us start with that, and see where the limiting factors are. At first, this allows us to develop the software and a very reliable synchronization of the whole setup, which is mandatory for time-resolved fluorescence.

In this case, it was evident that the weakest part of the chain was the source. Even if it is powerful, a beam emitted by a LED cannot be focused sufficiently on the sample. We were hardly surprised by the poor results, as it is well known in optics, but the fluorescence depends on the fluorophore efficiency and its concentration in the sample. Maybe could we be lucky enough to have a sufficiently good signal here despite low illumination efficiency? Nope.

So we looked for a laser diode far enough in the UV domain to excite our terbium-based agent. The LED taught us that a good extinction, as soon as possible, after the "turn off" command of the source was uttermost important; otherwise, residual autofluorescence would contaminate the signal. That is why we choose the Vortran laser among many other quite similar systems.

With the laser, we can get some beautiful images, when the concentration of fluorophores is quite high. But the bright regions… do they really correspond to the contrast agent? Or do they result from some contamination by something else? (We never spoke about cleanliness and contamination here. It's an important point for any fluorescence experiment, when the signal is low. It is well known and we will not discuss about it any longer). We have to check if the bright regions really correspond to our fluorescent probe… It is time to build a spectrometer! The microscope has two output ports. We put the imaging camera at one of them. We can put a spectrometer and another camera at the other port, or we can insert the spectrometer before the main camera, whatever is the most practical way to do it. Our spectrometer is home-built; we have all the necessary parts in the laboratory. With it, we can simultaneously get a fluorescent image and check if this signal is really the one we want.

However, the intensified camera we used at first, made by Proxitronic, has a too low quantum efficiency, and the gain stage is too noisy. Therefore, we had to get a better camera. We looked for the best camera we could find, even if it was expensive. Quantum efficiency was important. Trigger modes, for time resolution, were important too, of course. After testing several cameras, we settled for the Andor one.

The laser power is still a limiting factor. We have an illumination area (and as a consequence, a collecting area) smaller than the full image provided by the microscope. Since we want to quickly scan a sample for bright regions – while checking the spectrum with the spectrometer – we developed the “mosaic imaging”.

We tried to quantify the florescence signal, characterizing the system’s apparatus function, in particular the camera. We can now quite reliably relate the number provided by the software at the end of the processing chain to the number of photons emitted in a given region of the sample.

Here we have the current system.

With it, we obtained the first images with pathological rat arteries. Since we had problems with the rats breeding, and the chemical binding of the fluorescent agent to the arteries, these results are very preliminary. As I write this, more experiments will be necessary to achieve the quality required for publications in reputable journals. However, it is obvious that we have a signal clear enough for the intended work.

Enough with the ‘curse’ side of the story. When I came to the laboratory, it was just a ‘dream’ project. As I finish my work in this laboratory, it is working, and it fully meets the expectations we had at the beginning of the project. We built most of the system together, and I feel proud of it. That’s a blessing.

Current system and its future evolution

We built a system, which is able to locate a fluorescent agent chemically similar to the MRI contrast agent used for detection of atherosclerosis. For the optical probe, we substitute lanthanides ions instead of the magnetic gadolinium ion. Fluorescence allows optical analysis of the interaction between the tissue and the agent. Optical microscopy has a very high intrinsic resolution, and therefore we expect to learn useful information about this interaction. A good signal to noise ratio is obtained by time-resolved fluorescence imaging, where autofluorescence is fast compared to the lanthanides emission. Our experiments use rats arteries, but since it really needs microscopy slides, any other kind of arteries are possible. We can positively identify terbium spectrum (or the spectrum of any other lanthanide marker), by evaluating the fluorescence spectrum while taking images, which rules out false positives. As is, the system is working, but we can improve it with a more powerful source, ideally, its wavelength could be adjusted to match the maximum absorption of the fluorescent molecules. A more efficient fluorescent light collection at the microscope would help too. After *in vivo* MR imaging, preliminary measurements show that we can indeed localize the contrast agent in pathological regions of the arteries. We now have too few examples to have a robust statistical analysis, and these results should be soon completed.

Appendix A

We describe a theory that allows us to estimate the number of collected photons by the fluorescent microscope system.

The size of the image of a point source

The image of a point of the sample on the camera has a size $r_{cam}(z)$, where *z* is the distance of the point to the focus plane. This size will be expressed as a size on the sample side, with $r(z) = r_{cam}(z)/G$, where *G* is the magnification. The size $r(z)$ depends on the diffraction for *z*~0, with:

$$r(z=0) = r_{diff} = \frac{\lambda}{2NA}$$

For high *z*, this size can be understood by geometrical optics:

$$r(z \rightarrow \infty) = r_{geom}(z) = \frac{zNA}{n}$$

A model to mix both behaviours is:

$$\mathrm{r(z)} = \sqrt{\mathrm{r}_{\mathrm{diff}}^2 + \mathrm{r}_{\mathrm{geom}}^2(\mathrm{z})} = \sqrt{\frac{\lambda^2}{4\mathrm{NA}^2} + \frac{\mathrm{z}^2\mathrm{NA}^2}{\mathrm{n}^2}} = \frac{\mathrm{NA}}{\mathrm{n}}\sqrt{\mathrm{z}^2 + \mathrm{z}_\mathrm{R}^2}$$

with $z_R = \dfrac{n\lambda}{2NA^2}$

A fluorescent point therefore enlightens a zone of size $r(z)$ (magnified by G on the camera), and will be modelled by a normalized Gaussian:

$$f(x,y,z) = \frac{N}{\pi\, r(z)^2} \exp\left[-\frac{x^2+y^2}{r(z)^2}\right]$$

The function *f* here is normalized to N, which is the collection efficiency: The factor ½ is due to the half-side collection, the factor $\mathrm{NA}^2/2\mathrm{n}^2$ comes from the solid angle of the collection system, and the factor ½ is brought by the beamsplitter: with NA=0.4 and n=1.33, we have N=1.13%. For $\lambda = 550nm$ we have $z_R = 2.3\mu m$.

The excitation beam has a size $w(z) = \theta_e\sqrt{z^2 + z_{\mathrm{Re}}^2}$, where $\theta_e = \dfrac{\lambda_e}{n\pi\, w_0}$ is the divergence of the excitation beam, w_0 is the beam waist and $z_{\mathrm{Re}} = \dfrac{n\pi\, w_0^2}{\lambda_e}$ is the Rayleigh length. For $\theta_e = 0.026$ one has $w_0 = 3.4\mu m$ and $z_{\mathrm{Re}} = 130\mu m$ (FWHM of the excitation beam: 3.1µm). The intensity of the excitation beam will be:

$$I(x,y,z) = \frac{2P}{\pi\, w(z-d)^2} \exp\left[-2\frac{x^2+y^2}{w(z-d)^2}\right]$$

where *P* is the excitation power and where *d* is the separation between the waist of the excitation beam and the focus plane.

Emitted photons

Let us consider rate equations on a quasi two-level system:

$$\dot{N}_1 = \frac{\sigma}{h\nu_e} I(1-N_1) + \frac{YN_1}{\tau} + \frac{1-Y}{\tau} N_1$$

where Y is the quantum yield. $\frac{YN_1}{\tau}$ is the probability to emit a photon, and $\frac{1-Y}{\tau}N_1$ is the probability to have a non-radiative transition. One has at the equilibrium:

$$N_1 = \frac{\frac{\sigma}{h\nu_e} I}{\frac{\sigma}{h\nu_e} I + \frac{1}{Y\tau}} = \frac{\frac{Y\sigma\tau}{h\nu_e} I}{1 + \frac{Y\sigma\tau}{h\nu_e} I}$$

The fluorescence is then (in emitted photons), if ρ is the particle density:

$$g(x,y,z) = \frac{Y\, I(x,y,z)/I_{sat}}{1 + I(x,y,z)/I_{sat}} \rho \approx Y \frac{I(x,y,z)}{I_{sat}} \rho = \frac{Y\sigma\tau\rho}{h\nu_e} I(x,y,z)$$

The photons collected on the camera are (L is the thickness of the water slab, with the focus on one side of the slab):

$$H(x,y) = \int_0^L f *_{x,y} g \, dz$$

With $g(x,y,z) \approx \frac{Y\sigma\tau\rho}{h\nu_e} I(x,y,z)$ one has:

$$f *_{x,y} g = \frac{Y\sigma\tau\rho}{h\nu_e} \frac{2P}{\pi w(z)^2} \frac{N}{\pi x(z)^2} \iint dX dY \exp\left[-\frac{X^2 + Y^2}{r(z)^2} - 2\frac{(x-X)^2 + (y-Y)^2}{w(z)^2} \right]$$

$$\begin{aligned}
\frac{X^2}{r(z)^2} + 2\frac{(x-X)^2}{w(z)^2} &= (\frac{1}{r(z)^2} + 2\frac{1}{w(z)^2})X^2 - 4\frac{xX}{w(z)^2} + 2\frac{x^2}{w(z)^2} \\
&= (\frac{w(z)^2 + 2r(z)^2}{r(z)^2 w(z)^2})(X - 2\frac{r(z)^2 x}{w(z)^2 + 2r(z)^2})^2 - 4\frac{r(z)^2}{w(z)^2 + 2r(z)^2}\frac{x^2}{w(z)^2} + 2\frac{x^2}{w(z)^2} \\
&= (\frac{w(z)^2 + 2r(z)^2}{r(z)^2 w(z)^2})(X - 2\frac{r(z)^2 x}{w(z)^2 + 2r(z)^2})^2 + 2\frac{x^2}{w(z)^2 + 2r(z)^2}
\end{aligned}$$

Let us define $w_f^2(z) = w(z)^2 + 2r(z)^2$, we then have :

$$\int dX \exp\left[-\frac{X^2}{r(z)^2} - 2\frac{(x-X)^2}{w(z)^2} \right] = \sqrt{\pi} \frac{r(z) w(z)}{w_f(z)} \exp\left[-2\frac{x^2}{w_f^2(z)} \right]$$

and we have the same for integration on Y. So, finally:

$$f *_{x,y} g = \frac{Y\sigma\tau\rho}{h\nu_e} \frac{2NP}{\pi w_f(z)^2} \exp\left[-2\frac{x^2 + y^2}{w_f(z)^2} \right]$$

When L is small, the size of H does not depend so much on d, the function H is observed to be nearly Gaussian:

$$H(x,y) \approx \frac{2F}{\pi W^2} \exp\left[-2\frac{x^2+y^2}{W^2}\right]$$

where F is the total collection of the fluorescence light.

Calculation of the total power F (in received photons)

$$F \equiv \iint h(x,y)dxdy = \int dz \left[\iint fdxdy \cdot \iint gdxdy\right]$$

Far from saturation, this simply gives

$$F \approx \frac{Y\sigma\tau\rho L\, NP}{h\nu_e}$$

Calculation of $\iint gdxdy = Y\rho \iint \frac{I(x,y,z)/I_{sat}}{1+I(x,y,z)/I_{sat}} dxdy = 2\pi Y\rho \int_0^\infty \frac{\alpha e^{-2r^2/w^2}}{1+\alpha e^{-2r^2/w^2}} rdr$

with $\alpha = \frac{2P}{\pi w(z-d)^2 I_{sat}}$. This can be readily integrated into:

$$\iint gdxdy = \frac{\pi Y\rho\, w^2(z-d)}{2} \ln(1+\alpha)$$

We therefore have

$$F \equiv \frac{\pi Y\rho\, N}{2} \int_0^L dz\, w^2(z-d) \ln\left[1+\frac{2P}{\pi w(z-d)^2 I_{sat}}\right]$$

If one neglects the variations of *w*, we have:

$$F \approx \frac{\pi Y\rho\, NLw^2}{2} \ln\left[1+\frac{2P}{\pi w^2 I_{sat}}\right]$$

Therefore the number of photoelectrons is simply:

$$n_{e-} \approx \frac{\pi Y\rho\eta\, NLw^2}{2} \ln\left[1+\frac{2P}{\pi w^2 I_{sat}}\right] = \frac{\pi Y\rho\eta\, NLw^2}{2} \ln\left[1+\frac{2\tau P}{\pi w^2 h\nu_e} Y\sigma\right]$$

Appendix B

A Matlab script is used to estimate the number of photoelectrons at the input of the electron multiplying register of the EMCCD camera.

```
% output:
%       average number of photons
%       Error of average number of photons
%       R_Square
% IF there are n photon at input, the output value k has probability f_n(k)
% IF p(n,k) is the probability of n and abey Poisson distribution
%    fi(n)=n^i*exp(-n)/(i!)
% where i is value-able of random variable; n is mean of i
% the output value y has probability is
%               pp(y)=sum[f(x)*px(y)] with x is the variant
% To find px(y) we must know p1(y), then we have
%               p1(y)=a*exp(-y/Dy)
%               px(y)=sum[p1(kxi)*p(x-1)(y-kxi)]
% for example   p2(y)=sum[p1(kxi)*p1(y-kxi)]
%               p3(y)=sum[p1(kxi)*p2(y-kxi)]
clear all;
close all;
pn_y_ready=1;
start=100;              % initial minimum number of entrance photoelectron
finish=start+100;       % initial maximum number of entrance photoelectron
max_digit=16383;
AcpErr=1e-12;           % the acceptable error of difference of SSE/SST
F_n_k_file='pn_y_max_16280_n_700_kc_95_w_3.681_Dk_46.927_BLC1.mat';
histo_file='FVB histo BLC0_H.dat';
max_value=16280;
n=700;                  % maximum number of entrance photoelectrons
F_n_k=zeros(n+1,max_value+1);   %
if (pn_y_ready==1)
   load (F_n_k_file);
   %save (F_n_k_file, 'n','kc','w','f_0_k', 'Dk','f_1_k','F_n_k','max_value','max_digit');
end
k=0:max_value;
```

```
F_lamda_k=0*linspace(1,max_value+1,max_value+1);
p_n=0*linspace(0,n,n+1);             % distribution of entrance photoelectron

%%%%%%%%%%%%%%%%%%%%%%%%%%%%%%%%%%%%%%%%%%
%
% pn(k) IS CALCULATED
if pn_y_ready==0
% f_0_k(k)
% Gauss p0=A*exp(-0.5*((k-yc)/w)^2)
   kc=95;                            % BaseLineClamp=1
   w=3.681;                          % BaseLineClamp=1
   f_0_k=exp(-0.5*((k-kc)/w).^2);
   f_0_k=f_0_k/sum(f_0_k);

   % f_1_k(k)
   Dk=46.927;     % BaseLineClamp=1
   f_1_k=exp(-k/Dk);
   f_1_k=f_1_k/sum(f_1_k);
   F_n_k(1,:)=f_0_k;                 % zezo photon
   F_n_k(2,:)=f_1_k;
   for dem=3:n
      temp=1/(Dk*(dem-2));
      for dem2=1:max_value+1
         F_n_k(dem,dem2)=F_n_k(dem-1,dem2)*(dem2-1)*temp;
      end
   end
   for dem=2:n
      if mod(dem,20)==0
         clc
      end
      dem
      F_n_k_temp=conv(F_n_k(dem-1,:),f_1_k);
      F_n_k_temp(length(f_1_k))=sum(F_n_k_temp(length(f_1_k):end));
      F_n_k(dem,:)=F_n_k_temp(1:length(f_1_k));
   end
```

```
        save (F_n_k_file, 'n','kc','w','f_0_k', 'Dk','f_1_k','F_n_k','max_value','max_digit');
    end

    %%%%%%%%%%%%%%%%%%%%%%%%%%%%%%%%%%%%%%%%%
%
    if pn_y_ready==1
        % GET DATA FROM A FILE
        temp_data=dlmread(histo_file,'\t',[0 2 max_digit 2]);
        temp_data=temp_data';
        data=temp_data(1:max_value+1);
        if max_value<max_digit
            data(max_value+1)=sum(temp_data(max_value+1:max_digit+1));
        end
        data=data/sum(data);    % normalize data
        %semilogy(k,data);

        %USE "LEAST SQUARE METHOD" TO FIND AVERAGE OF INPUT PHOTONS

        diff=1e9;
        diff2=diff;
        index=0;
        index_a=0;
        n_avr_min=0;
        count_off=0;
        data_avr=sum(data)/length(data);
        % Total Sum of Square
        SST=sum((data-data_avr).^2);
        while (diff>AcpErr)
            count_off=count_off+1;
            SSE=[0 0 0 0 0];
            R_Square=SSE;
            n_avr_arr=linspace(start,finish,5)
            for count=1:5
                p_n(1)=exp(-n_avr_arr(count));   % count=1 corresponds i=0;
                for dem=2:n+1
                    p_n(dem)=p_n(dem-1)*n_avr_arr(count)/(dem-1);
    end;
    F_lamda_k=0*F_lamda_k;
    for dem=0:n
        F_lamda_k=F_lamda_k+F_n_k(dem+1,:)*p_n(dem+1);
    end;
    % Sum of Squares due to Errors
    SSE(count)=sum(((data)-(F_lamda_k)).^2);
end;
R_Square=SSE/SST;
[value,index]=min(R_Square);
if diff>AcpErr
    if (index>1)&&(index<5)
        start=n_avr_arr(index-1);
        finish=n_avr_arr(index+1);
        if ((R_Square(index)-R_Square(index+1))*(R_Square(index)-R_Square(index+1)))>((R_Square(index)-R_Square(index-1))*(R_Square(index)-R_Square(index-1)))
            diff=R_Square(index)-R_Square(index-1);
            if diff<0
                diff=-diff;
            end;
            index_a=index-1;
        else
            diff=R_Square(index)-R_Square(index+1);
            if diff<0
                diff=-diff;
            end;
            index_a=index+1;
        end;
    end;
    if (index==1)
        start=n_avr_arr(index);
        finish=n_avr_arr(index+1);
        diff=R_Square(index)-R_Square(index+1);
        if diff<0
            diff=-diff;
        end;
```

```
                index_a=index+1;
            end;
            if (index==5)
                start=n_avr_arr(index-1);
                finish=n_avr_arr(index);
                diff=R_Square(index)-R_Square(index-1);
                if diff<0
                    diff=-diff;
                end;
                index_a=index-1;
            end;
        end;
        n_avr_min=n_avr_arr(index);
    end; %while (diff>=AcpErr)
    count_off
    n_avr_min
    n_avr_err=abs(n_avr_arr(index)-n_avr_arr(index_a))
    RSquare=1-value
    n_avr=n_avr_min;
    p_n(1)=n_avr^0*exp(-n_avr);
    for dem=1:n-1
        p_n(dem+1)=p_n(dem)*n_avr/dem;
    end;
    F_lamda_k=0*F_lamda_k;
    for dem=0:n-1
        F_lamda_k=F_lamda_k+F_n_k(dem+1,:).*p_n(dem+1);
    end;

%%%%%%%%%%%%%%%%%%%%%%%%%%%%%%%%%%%%%%%%%

   plot(data,'*');
    hold on;
   plot(F_lamda_k,'r','linewidth',3);
    title(strcat('Average entrance photoectrons: ',num2str(n_avr)));
end
```

References

[1] http://www.heart.org/HEARTORG/Conditions/Cholesterol/WhyCholesterolMatters/Atherosclerosis_UCM_305564_Article.jsp

[2] B. Hogers, D. Gross, V. Lehmann, H. J. de Groot, A. de Roos, A. C. Gittenberger-de Groot, and R. E. Poelmann, “Magnetic resonance microscopy at 17.6-Tesla on chicken embryos in vitro,” *Journal of Magnetic Resonance Imaging*, vol. 14, no. 1, pp. 83–86, 2001.

[3] J. R. Gardner, C. P. Hess, A. G. Webb, R. W. Tsika, M. J. Dawson, and V. Gulani, “Magnetic resonance microscopy of morphological alterations in mouse trabecular bone structure under conditions of simulated microgravity,” *Magnetic resonance in medicine*, vol. 45, no. 6, pp. 1122–1125, 2001.

[4] S. Ropele, F. Ebner, F. Fazekas, and G. Reishofer, “Super-resolution MRI using microscopic spatial modulation of magnetization,” *Magnetic Resonance in Medicine*, vol. 64, no. 6, pp. 1671–1675, Dec. 2010.

[5] K.-H. Herrmann, S. Schmidt, A. Kretz, R. Haenold, I. Krumbein, M. Metzler, C. Gaser, O. W. Witte, and J. R. Reichenbach, “Possibilities and limitations for high resolution small animal MRI on a clinical whole-body 3T scanner,” *Magnetic Resonance Materials in Physics, Biology and Medicine*, vol. 25, no. 3, pp. 233–244, Oct. 2011.

[6] http://en.wikipedia.org/wiki/Atherosclerosis

[7] http://www.nagygeneracio.hu/Erelmeszesedes_ellen__helyes_etrend

[8] H. C. Stary, A. B. Chandler, R. E. Dinsmore, V. Fuster, S. Glagov, W. Insull, M. E. Rosenfeld, C. J. Schwartz, W. D. Wagner, and R. W. Wissler, “A Definition of Advanced Types of Atherosclerotic Lesions and a Histological Classification of Atherosclerosis : A Report From the Committee on Vascular Lesions of the Council on Arteriosclerosis, American Heart Association,” *Circulation*, vol. 92, no. 5, pp. 1355–1374, Sep. 1995.

[9] L. K. Jennings, “Role of platelets in atherothrombosis,” *Am. J. Cardiol.*, vol. 103, no. 3 Suppl, p. 4A–10A, Feb. 2009.

[10] McEver RP. “Adhesive interactions of leukocytes, platelets, and the vessel wall during hemostasis and inflammation”, *Thromb. Haemost*. 2001, 3: 746-756.

[11] Gawaz M, Langer H, May AE, “Platelets in inflammation and atherogenesis”, *J. Clin. Invest*. 2005, 12, 3378-3384.

[12] Wagner DD, “New links between inflammation and thrombosis. Arterioscler”, *Thromb. Vasc. Biol.* 2005, 7, 1321-1324.

[13] McEver RP., “Selectin-carbohydrate interactions during inflammation and metastasis”, *Glycoconj. J*. 1997, 5, 585-591.

[14] Springer TA. “Traffic signals on endothelium for lymphocyte recirculation and leukocyte emigration”, *Annu. Rev. Physiol.* 1995, 827-872.

[15] Blondin C, Bataille I, Letourneur D. “Polysaccharides for vascular cell targeting”, *Crit. Rev. Ther. Drug Carrier Syst.* 2000; 4: 327-375.

[16] Hiramatsu, Y.; Tsujishita, H.; Kondo, H., Studies on selectin blocker. 3. Investigation of the carbohydrate ligand sialyl Lewis X recognition site of P-selectin. *J Med Chem* **1996,***39* (23), 4547-53.

[17] Vestweber D, Blanks JE. “Mechanisms that regulate the function of the selectins and their ligands”, *Physiol. Rev.* 1999, 1, 181-213.

[18] Ramphal, J. Y.; Zheng, Z. L.; Perez, C.; Walker, L. E.; DeFrees, S. A.; Gaeta, F. C., Structure-activity relationships of sialyl Lewis x-containing oligosaccharides. 1. Effect of modifications of the fucose moiety. *J Med Chem* **1994,***37* (21), 3459-63.

[19] L. Bachelet, I. Bertholon, D. Lavigne, R. Vassy, M. Jandrot-Perrus, F. Chaubet and D. Letourneur, *Biochim. Biophys. Acta*, 2009, **1790**, 141-146.

[20] Koenig, A.; Jain, R.; Vig, R.; Norgard-Sumnicht, K. E.; Matta, K. L.; Varki, A., Selectin inhibition: synthesis and evaluation of novel sialylated, sulfated and fucosylated oligosaccharides, including the major capping group of GlyCAM-1. *Glycobiology* **1997,***7* (1), 79-93.

[21] A. C. Lake, R. Vassy, M. Di Benedetto, D. Lavigne, C. Le Visage, G. Y. Perret and D. Letourneur, *J. Biol. Chem.*, 2006, **281**, 37844-37852.

[22] C. E. Luyt, A. Meddahi-Pelle, B. Ho-Tin-Noe, S. Colliec-Jouault, J. Guezennec, L. Louedec, H. Prats, M. P. Jacob, M. Osborne-Pellegrin, D. Letourneur and J. B. Michel, *J. Pharmacol. Exp. Ther.*, 2003, **305**, 24-30.

[23] http://www.imaios.com/en/e-Courses/e-MRI/MRI-signal-contrast/Signal-weighting

[24] R. B. Lauffer, “Paramagnetic metal complexes as water proton relaxation agents for NMR imaging: theory and design,” *Chemical Reviews*, vol. 87, no. 5, pp. 901–927, Oct. 1987.

[25] P. Caravan, J. J. Ellison, T. J. McMurry, and R. B. Lauffer, “Gadolinium(III) Chelates as MRI Contrast Agents: Structure, Dynamics, and Applications,” *Chemical Reviews*, vol. 99, no. 9, pp. 2293–2352, Sep. 1999.

[26] A. Bjornerud and L. Johansson, “The utility of superparamagnetic contrast agents in MRI: theoretical consideration and applications in the cardiovascular system,” *NMR in Biomedicine*, vol. 17, no. 7, pp. 465–477, Nov. 2004.

[27] G. Strijkers, W. M. Mulder, G. F. van Tilborg, and K. Nicolay, “MRI Contrast Agents: Current Status and Future Perspectives,” *Anti-Cancer Agents in Medicinal Chemistry*, vol. 7, no. 3, pp. 291–305, May 2007.

[28] C. V. Bowen, X. Zhang, G. Saab, P. J. Gareau, and B. K. Rutt, “Application of the static dephasing regime theory to superparamagnetic iron-oxide loaded cells,” *Magn Reson Med*, vol. 48, no. 1, pp. 52–61, Jul. 2002.

[29] Y. X. Wang, S. M. Hussain, and G. P. Krestin, “Superparamagnetic iron oxide contrast agents: physicochemical characteristics and applications in MR imaging,” *Eur Radiol*, vol. 11, no. 11, pp. 2319–2331, 2001.

[30] R. Weissleder, G. Elizondo, J. Wittenberg, C. A. Rabito, H. H. Bengele, and L. Josephson, “Ultrasmall superparamagnetic iron oxide: characterization of a new class of contrast agents for MR imaging,” *Radiology*, vol. 175, no. 2, pp. 489–493, May 1990.

[31] R. Weissleder, A. Bogdanov, E. A. Neuwelt, and M. Papisov, “Long-circulating iron oxides for MR imaging,” *Advanced Drug Delivery Reviews*, vol. 16, no. 2–3, pp. 321–334, Sep. 1995.

[32] P. Wunderbaldinger, L. Josephson, and R. Weissleder, “Crosslinked iron oxides (CLIO): a new platform for the development of targeted MR contrast agents,” *Acad Radiol*, vol. 9 Suppl 2, pp. S304–306, Aug. 2002.

[33] M. Taupitz, J. Schnorr, C. Abramjuk, S. Wagner, H. Pilgrimm, H. Hünigen, and B. Hamm, “New generation of monomer-stabilized very small superparamagnetic iron oxide particles (VSOP) as contrast medium for MR angiography: preclinical results in rats and rabbits,” *J Magn Reson Imaging*, vol. 12, no. 6, pp. 905–911, Dec. 2000.

[34] http://culturesciences.chimie.ens.fr/content/principe-de-lirm-les-agents-de-contraste-759

[35] I. Solomon, “Relaxation Processes in a System of Two Spins,” *Physical Review*, vol. 99, no. 2, pp. 559–565, Jul. 1955.

[36] N. Bloembergen, “Proton Relaxation Times in Paramagnetic Solutions,” *The Journal of Chemical Physics*, vol. 27, no. 2, p. 572, 1957.

[37] N. Bloembergen and L. O. Morgan, “Proton Relaxation Times in Paramagnetic Solutions. Effects of Electron Spin Relaxation,” *The Journal of Chemical Physics*, vol. 34, no. 3, p. 842, 1961.

[38] E. Kahn, C. Tessier, G. Lizard, A. Petiet, J.-C. Bernengo, D. Coulaud, C. Fourre, F. Frouin, O. Clement, J.-R. Jourdain, E. Delain, F. Guiraud-Vitaux, N. Colas-Linhart, N. Siauve, C.-A. Cuenod, G. Frija, and A. Todd-Pokropek, “Analysis of the distribution of MRI contrast agents in the livers of small animals by means of complementary microscopies,” *Cytometry*, vol. 51A, no. 2, pp. 97–106, Feb. 2003.

[39] A. Beilvert, D. P. Cormode, F. Chaubet, K. C. Briley-Saebo, V. Mani, W. J. M. Mulder, E. Vucic, J.-F. Toussaint, D. Letourneur, and Z. A. Fayad, “Tyrosine polyethylene glycol (PEG)-micelle magnetic resonance contrast agent for the detection of lipid rich areas in atherosclerotic plaque,” *Magnetic Resonance in Medicine*, vol. 62, no. 5, pp. 1195–1201, Nov. 2009.

[40] C. Bremer, V. Ntziachristos, and R. Weissleder, “Optical-based molecular imaging: contrast agents and potential medical applications,” *Eur Radiol*, vol. 13, no. 2, pp. 231–243, Feb. 2003.

[41] I. Hemmilä, S. Dakubu, V. M. Mukkala, H. Siitari, and T. Lövgren, “Europium as a label in time-resolved immunofluorometric assays,” *Anal. Biochem.*, vol. 137, no. 2, pp. 335–343, Mar. 1984.

[42] W. L. Scaff, D. L. Dyer, and K. Mori, “Fluorescent europium chelate stain,” *Journal of bacteriology*, vol. 98, no. 1, pp. 246–248, 1969.

[43] J.-C. G. Bünzli, “Lanthanide Luminescent Bioprobes (LLBs),” *Chemistry Letters*, vol. 38, no. 2, pp. 104–109, 2009.

[44] J. Yuan and G. Wang, “Lanthanide complex-based fluorescence label for time-resolved fluorescence bioassay,” *J Fluoresc*, vol. 15, no. 4, pp. 559–568, Jul. 2005.

[45] K. A. Gschneidner, L. Eyring, J.-C. G. Bünzli, and V. K. Pecharsky, *Handbook on the physics and chemistry of rare earths*. Amsterdam: North-Holland, 1979.

[46] Ulrich Brackmann, *Laser Dyes*, 3rd edition, Göttingen, 2000.

[48] E. Beaurepaire, V. Buissette, M.-P. Sauviat, D. Giaume, K. Lahlil, A. Mercuri, D. Casanova, A. Huignard, J.-L. Martin, T. Gacoin, J.-P. Boilot, and A. Alexandrou, “Functionalized Fluorescent Oxide Nanoparticles: Artificial Toxins for Sodium Channel Targeting and Imaging at the Single-Molecule Level,” *Nano Letters*, vol. 4,

no. 11, pp. 2079–2083, Nov. 2004.

[49] Y. Chen, Y. Chi, H. Wen, and Z. Lu, “Sensitized luminescent terbium nanoparticles: preparation and time-resolved fluorescence assay for DNA,” *Analytical chemistry*, vol. 79, no. 3, pp. 960–965, 2007.

[50] M. Xiao and P. R. Selvin, “Quantum Yields of Luminescent Lanthanide Chelates and Far-Red Dyes Measured by Resonance Energy Transfer,” *Journal of the American Chemical Society*, vol. 123, no. 29, pp. 7067–7073, Jul. 2001.

[51] A. P. S. Samuel, J. Xu, and K. N. Raymond, “Predicting Efficient Antenna Ligands for Tb(III) Emission,” *Inorganic Chemistry*, vol. 48, no. 2, pp. 687–698, Jan. 2009.

[52] J. Sokolnicki, “Enhanced luminescence of Tb^{3+} due to efficient energy transfer from Ce^{3+} in a nanocrystalline $Lu_2Si_2O_7$ host lattice,” *Journal of Physics: Condensed Matter*, vol. 22, no. 27, p. 275301, Jul. 2010.

[53] C. C. Bryden and C. N. Reilley, “Europium luminescence lifetimes and spectra for evaluation of 11 europium complexes as aqueous shift reagents for nuclear magnetic resonance spectrometry,” *Analytical Chemistry*, vol. 54, no. 4, pp. 610–615, Apr. 1982.

[54] K. A. Gschneidner, J.-C. G. Bünzli, and V. K. Pecharsky, *Handbook on the physics and chemistry of rare earths*. Amsterdam: North-Holland, 2007.

[55] M. Elbanowski, S. Lis, and J. Konarski, “Quantum efficiency of the luminescence of Eu (III), Tb (III) and Dy (III) in aqueous solutions,” *Monatshefte für Chemie/Chemical Monthly*, vol. 120, no. 8–9, pp. 699–703, 1989.

[56] M. Li and P. R. Selvin, “Luminescent Polyaminocarboxylate Chelates of Terbium and Europium: The Effect of Chelate Structure,” *Journal of the American Chemical Society*, vol. 117, no. 31, pp. 8132–8138, Aug. 1995.

[57] J. L. Kropp and M. W. Windsor, “Enhancement of Fluorescence Yield of Rare-Earth Ions by Heavy Water,” *The Journal of Chemical Physics*, vol. 39, no. 10, pp. 2769–2770, 1963.

[58] J. J. Freeman, G. A. Crosby, and K. E. Lawson, “The effect of deuterium on the luminescence decay times of solvated rare earth chlorides,” *Journal of Molecular Spectroscopy*, vol. 13, no. 1, pp. 399–406, 1964.

[59] J. L. Kropp and M. W. Windsor, “Luminescence and Energy Transfer in Solutions of Rare-Earth Complexes. I. Enhancement of Fluorescence by Deuterium Substitution,” *The Journal of Chemical Physics*, vol. 42, no. 5, p. 1599, 1965.

[60] J. L. Kropp, “Comment on the Fluorescence of Trivalent Europium in D2O—H2O Mixtures,” *The Journal of Chemical Physics*, vol. 45, no. 2, p. 761, 1966.

[61] Y. J. Zhang, Y. Chen, Q. D. Liu, X. G. Wang, J. R. Li, and H. Liu, “Synthesis, characterization and luminescent properties of terbium and europium complexes with ligands from DTPA and pAS,” *Journal of alloys and compounds*, vol. 307, no. 1, pp. 137–140, 2000.

[62] G. Vereb, E. Jares-Erijman, P. R. Selvin, and T. M. Jovin, “Temporally and spectrally resolved imaging microscopy of lanthanide chelates,” *Biophysical journal*, vol. 74, no. 5, pp. 2210–2222, 1998.

[63] G. Marriott, M. Heidecker, E. P. Diamandis, and Y. Yan-Marriott, “Time-resolved delayed luminescence image microscopy using an europium ion chelate complex,” *Biophysical Journal*, vol. 67, no. 3, pp. 957–965, Sep. 1994.

[64] N. Gahlaut and L. W. Miller, “Time-resolved microscopy for imaging lanthanide luminescence in living cells,” *Cytometry Part A*, vol. 77A, no. 12, pp. 1113–1125, Dec. 2010.

[65] [65] T. K. Christopoulos and E. P. Diamandis, “Enzymatically amplified time-resolved fluorescence immunoassay with terbium chelates,” *Anal. Chem.*, vol. 64, no. 4, pp. 342–346, Feb. 1992.

[66] A. G. Basden, C. A. Haniff, and C. D. Mackay, “Photon counting strategies with low-light-level CCDs,” *Monthly Notices of the Royal Astronomical Society*, vol. 345, no. 3, pp. 985–991, Nov. 2003.

[67] http://web.maths.unsw.edu.au/~adelle/Garvan/Assays/67.html

[68] https://www.andor.com/learning-academy/quantitative-stability-stability-in-emccds

[69] P. R. Selvin and J. E. Hearst, “Luminescence energy transfer using a terbium chelate: improvements on fluorescence energy transfer,” *Proceedings of the National Academy of Sciences*, vol. 91, no. 21, pp. 10024–10028, 1994.

[70] Corot C, Schaefer M, Beaute S, Bourrinet P, Zehaf S, Benize V, Sabatou M, Meyer D. Physical, chemical and biological evaluations of CMD-A2-Gd-DOTA. A new paramagnetic dextran polymer. Acta Radiol. Suppl. 1997; 91–99.

[71] L. Armelao, S. Quici, F. Barigelletti, G. Accorsi, G. Bottaro, M. Cavazzini, and E. Tondello, “Design of luminescent lanthanide complexes: From molecules to highly efficient photo-emitting materials,” *Coordination Chemistry Reviews*, vol. 254, no. 5–6, pp. 487–505, Mar. 2010.

[72] M. Albin, W. D. Horrocks, and F. J. Liotta, “Characterization of a potentially axially symmetric europium(III) complex of a tetraacetate,tetraaza, macrocyclic ligand by luminescence excitation, emission and lifetime spectroscopy,” *Chemical Physics Letters*, vol. 85, no. 1, pp. 61–64, Jan. 1982.

[73] [F. Chaubet, I. Bertholon, J-M. Serfaty, R. Bazeli, H. Alsaid, M. Jandrot-Perrus, C. Zahir, P. Even, L. Bachelet, Z. Touat, E. Lancelot, C. Corot, E. Canet-Soulas, D. Letourneur, "A new macromolecular paramagnetic MR contrast agent binds to activated human platelets" Contrast Media and Molecul. Imag., 2007, jul. 2(4) 178-188]

[74] Kusaykin, M.; Bakunina, I.; Sova, V.; Ermakova, S.; Kuznetsova, T.; Besednova, N.; Zaporozhets, T.; Zvyagintseva, T., Structure, biological activity, and enzymatic transformation of fucoidans from the brown seaweeds. *Biotechnol J* **2008,***3* (7), 904-15.

[74] Li, B.; Lu, F.; Wei, X.; Zhao, R., Fucoidan: structure and bioactivity. *Molecules* **2008,***13* (8), 1671-95.

[75] Nardella, A.; Chaubet, F.; Boisson-Vidal, C.; Blondin, C.; Durand, P.; Jozefonvicz, J., Anticoagulant low molecular weight fucans produced by radical process and ion exchange chromatography of high molecular weight fucans extracted from the brown seaweed Ascophyllum nodosum. *Carbohydr Res* **1996,***289*, 201-8.

[76] Logeart, D.; Letourneur, D.; Jozefonvicz, J.; Kern, P., Collagen synthesis by vascular smooth muscle cells in the presence of antiproliferative polysaccharides. *J Biomed Mater Res* **1996,***30* (4), 501-8

[78] Cumashi, A.; Ushakova, N. A.; Preobrazhenskaya, M. E.; D'Incecco, A.; Piccoli, A.; Totani, L.; Tinari, N.; Morozevich, G. E.; Berman, A. E.; Bilan, M. I.; Usov, A. I.;

Ustyuzhanina, N. E.; Grachev, A. A.; Sanderson, C. J.; Kelly, M.; Rabinovich, G. A.; Iacobelli, S.; Nifantiev, N. E., A comparative study of the anti-inflammatory, anticoagulant, antiangiogenic, and antiadhesive activities of nine different fucoidans from brown seaweeds. Glycobiology 2007,17 (5), 541-52.

[79] F. Rouzet, L. Bachelet-Violette, J. M. Alsac, M. Suzuki, A. Meulemans, L. Louedec, A. Petiet, M. Jandrot-Perrus, F. Chaubet, J. B. Michel, D. Le Guludec and D. Letourneur, J. Nucl. Med., 2011, 52, 1433-1440.

[80] Bachelet-Violette L., Silva A. K. A., Maire M., Michel A., Brinza O., Phalla O., Ollivier V., Nicoletti A., Wilhelm C., Letourneur D., Ménager C., Chaubet, F., "Strong and specific interaction of ultra small superparamagnetic iron oxide nanoparticles and human activated platelets mediated by fucoidan coating" RSC Advances, 2014, 4 : pp4864-4871

Summary

We developed a fluorescence imaging microscope system intended for localizing and evaluating its concentration within arteries slices of a macromolecular (P717) Gd-based MRI contrast agent used for the visualization of atherosclerotic lesions. As the contrast agent is not initially fluorescent, we modified the agent which is now partially fitted with Tb ions, while preserving its chemical characteristics. A long fluorescence emission time constant enables us to have a suitable signal to noise ratio, despite a low intensity, using pulsed illumination and time gated imaging after the other sources of fluorescence have decayed.

The excitation source, on top of the inverted microscope, is a laser diode emitting at 371nm. The fluorescence signal is imaged on an ICCD camera. The fluorescence spectrum is acquired too, to positively insure that the signal really comes from the intended contrast agent. A microcontroller synchronizes electrical gating of the ICCD camera, of the laser pulse and generally controls automatically all parts of the measurement process. For tissue identification, we acquire a “natural image” using the standard halogen lamp of the microscope. This image is synthesized by the use of the combination of three successive images taken with the three fundamental colors. Then our software assembles the color and fluorescence images.

First images of rat arteries show that the contrast agent is indeed localized on specific regions of the tissues. We now have a new tool which allows us to understand and optimize the MRI contrast agent.

Résumé

Nous avons développé un microscope d’imagerie de fluorescence destiné à localiser, et à évaluer la concentration, d’un agent de contraste IRM macromoléculaire (P717) incluant du Gd, destiné à identifier les lésions athérosclérotiques. Comme l’agent de contraste n’est pas naturellement fluorescent, nous l’avons modifié en substituant des ions Tb aux ions Gd, ce qui ne modifie pas ses propriétés chimiques vis-à-vis de l’artère. Comme sa constante de temps est très supérieure à celle des autres sources de fluorescence, nous obtenons un bon rapport signal sur bruit, malgré une faible émission, par une technique de résolution temporelle.

La source d’excitation, sur le microscope inversé, est une diode laser émettant à 371nm, le capteur est une caméra ICCD. Nous mesurons aussi le spectre de la fluorescence pour nous assurer que le signal provient réellement de l’agent étudié. Un microcontrôleur permet de gérer automatiquement la synchronisation de toutes les parties du système. Pour l’identification des tissus par un anatomo-pathologiste, nous prenons aussi une photo en « couleurs naturelles » en prenant successivement trois images aux trois couleurs fondamentales. Ensuite, notre logiciel assemble toutes les images en couleurs et en fluorescence.

Les premières images que nous avons prises sur des artères de rat nous prouvent que l’agent de contraste est effectivement localisé dans des régions spécifiques. Nous disposons maintenant d’un outil nous permettant de comprendre l’attachement d’un agent de contraste IRM sur uneartère et qui nous permettra d’optimiser cet agent.